University of Denver
Digital Commons @ DU

Electronic Theses and Dissertations | Graduate Studies

8-1-2014

Electron Paramagnetic Resonance Imaging and Probes

Hanan B. Elajaili
University of Denver

Follow this and additional works at: https://digitalcommons.du.edu/etd

 Part of the Chemistry Commons

Recommended Citation

Elajaili, Hanan B., "Electron Paramagnetic Resonance Imaging and Probes" (2014). *Electronic Theses and Dissertations*. 179.
https://digitalcommons.du.edu/etd/179

This Dissertation is brought to you for free and open access by the Graduate Studies at Digital Commons @ DU. It has been accepted for inclusion in Electronic Theses and Dissertations by an authorized administrator of Digital Commons @ DU. For more information, please contact jennifer.cox@du.edu,dig-commons@du.edu.

Electron Paramagnetic Resonance Imaging and Probes

_____

A Dissertation

Presented to

The Faculty of Natural Sciences and Mathematics

University of Denver

_____

In Partial Fulfillment

of the Requirements for the Degree

Doctor of Philosophy

_____

By

Hanan B. Elajaili

August 2014

Advisor: Sandra S. Eaton

©Copyright by Hanan B. Elajaili 2014

All Rights Reserved

Author: Hanan B. Elajaili
Title: Electron Paramagnetic Resonance Imaging and Probes
Advisor: Sandra S. Eaton
Degree Date: August 2014

Abstract

EPR imaging at low frequency is an important method to measure in vivo physiology. Because native paramagnetic species exist at low concentrations in living systems, exogenous paramagnetic species are needed for in vivo EPR. Selection of the appropriate EPR probe allows the experimenter to obtain information about the environment of the imaged probe and its spatial distribution. Relaxation times for several nitroxide radicals were studied with the aim of understanding the relaxation mechanisms, which provides criteria for design of suitable in vivo imaging probes.

Amino-substituted trityl radicals have the potential to monitor pH in vivo, and the suitability for this application depends on spectral properties. Electron spin relaxation times T_1 and T_2 were measured at X-band for the protonated and deprotonated forms of two amino-substituted triaryl methyl radicals. T_1 exhibits little dependence on protonation, which makes it useful for measuring O_2 concentration. Values of T_2 vary substantially with pH, reflecting a range of dynamic processes, and thus T_2 is a potentially useful monitor of pH.

The spin-lattice relaxation rates at 293 K for three anionic semiquinones (2,5-di-*t*-butyl-1,4-benzosemiquinone, 2,6-di-*t*-butyl-1,4-benzosemiquinone, and 2,3,5,6-tetramethoxy-1,4-benzosemiquinone) were studied at up to 8 frequencies between 250 MHz and 34 GHz in ethanol or methanol solution containing high concentrations of OH^-.

The relaxation rates are about a factor of 2 faster at lower frequencies than at 9 or 34 GHz when measured in solvent with normal isotope abundance. However, in perdeuterated alcohols the relaxation rates exhibit little frequency dependence. The relaxation rates were modeled as the sum of two frequency-independent contributions (spin rotation and a local mode) and two frequency-dependent contributions (modulation of dipolar interaction with solvent nuclei and a much smaller contribution from modulation of g anisotropy). The correlation time for modulation of the interaction with solvent nuclei is longer than the tumbling correlation time and is attributed to hydrogen bonding of the alcohol to the oxygen atoms of the semiquinones.

Rapid scan imaging was shown, for the same data acquisition time, to give higher signal-to-noise than continuous wave for the nitroxide probe ^{15}N-perdeuterated tempone. The narrow spectral widths for the amino-substituted triaryl methyl radicals facilitate spectral-spatial EPR imaging. A phantom was imaged using rapid scan to test the feasibility of mapping the pH and to test a new algorithm for full spectrum imaging. Finally, a spin coherence phenomenon was observed at X-band in semiquinone rapid scan spectra, which arises from closely-spaced nuclear hyperfine lines.

Acknowledgements

My sincere thanks to Prof. Sandra Eaton, and Prof. Gareth Eaton, who helped and supported me throughout this research.

I want to acknowledge the scholarship from the Libyan Ministry of Higher Education and Scientific Research. I am extending my thanks to the Department of Chemistry and Biochemistry for providing the facilities for this work.

My thanks, also to Prof. Andrei Kutateladze for his help. My thanks to my committee: Dr. Martin Margittai, Dr. Michelle Knowles and Dr. Bryan Cowen and the external chair Dr. Susan E. Sadler.

I want to acknowledge Dr. George Rinard and Richard Quine for their help. Also, my sincere thanks to Dr. Mark Tseitlin for his help and explanations.

Special thanks to Dr. Josh Biller with whom I worked as partner for several projects. Thanks to Drs. Deborah Mitchell and Virginia Meyer for their advice.

Zhelin Yu reserves special thanks for helping with the semiquinone rapid scan project. Priyanka Aggarwal reserves my thanks for her warm heart and for being a nice sister throughout my study. Thanks to my family in Libya for their prayers.

Finally my appreciation to my husband Ibrahim Awad without your help I could not proceed any step further in my study. My appreciation is to my children for their patience and support. I hope I can compensate them in the future on the time they spent waiting for me.

Table of Contents

Chapter One: Introduction 1
1.1 Electron Paramagnetic Resonance 1
1.2 EPR Methods 8

Chapter Two: Relaxation Time Measurements for Nitroxide Radicals 13
2.1 Introduction.....13
2.2 ^{14}N-mHCTPO and ^{14}N-Tempone-d_{16} 14
2.3 Comparison of the Results from Different Instruments 15
2.4 Relaxation Times Measurements for Six Nitroxide Radicals at X-band 16
2.5 Spin-lattice Relaxation Times by Saturation Recovery 22
2.6 Relaxation Times for Immobilized Radicals 29

Chapter Three: Frequency Dependence of Electron Spin-Lattice Relaxation for Semiquinones in Alcohol Solutions 32
3.1 Introduction 32
3.2 Materials and Methods 36
3.3 Modeling the Frequency Dependence of $1/T_1$ 45
3.4 Results and Discussion 48

Chapter Four: Electron Spin Relaxation Times of pH-Sensitive Amino Substituted Trityl Radicals 53
4.1 Introduction 53
4.2 Materials and Methods 54
4.3 Results and Discussion 56
4.4 Conclusion 66

Chapter Five: EPR Imaging 68
5.1 Introduction 68
5.2 Comparison between CW and Rapid Scan Methods for EPR Imaging of ^{15}N-PDT Nitroxide on the VHF (250MHz) Spectrometer 69
5.3 pH- Sensitive Trityl (aTAM) Imaging Applications.....78
5.4 Full Spectrum Rapid Scan Imaging 83

Chapter Six: X-Band Rapid Scan for Semiquinone Radicals and Spin Coherence Signal 87
6.1 Introduction.....87
6.2 Materials and Methods 88
6.3 Results and Discussion 89

Chapter Seven: Conclusion and Future Work.....107

References 113

Appendix – List of Publications……..119

List of Tables

Table 2.1 Nitroxide T_2 and T_1 values (μs) determined at X-band (0.27mM) 15

Table 2.2 Nitroxide T_2 and T_1 values (μs) determined at X-band (0.4mM) 15

Table 2.3 T_1 values (μs) for ^{14}N-mHCTPO (0.4 mM in toluene) determined at X-band using different instruments 16

Table 2.4 T_2 (μs) at X-band for ^{14}N-nitroxides 21

Table 2.5 T_1 (μs) at X-band for ^{14}N-nitroxides 21

Table 2.6 T_2 (μs) at X-band for ^{15}N-nitroxides 21

Table 2.7 T_1 (μs) at X-band for ^{15}N-nitroxides 22

Table 2.8 Slopes of plots of $1/T_2$ and $1/T_1$ vs. concentration 22

Table 2.9 NitroxideT_1 (μs) values determined by saturation recovery at X-band..... 28

Table 2.10 T_2 values in (μs) at X-band for immobilized samples 30

Table 2.11 T_1 values in (μs) at X-band for immobilized samples 31

Table 3.1 Contributions to Spin-Lattice Relaxation of Semiquinones at 293 K in Fluid Solution 51

Table 3.2 Comparison between contributions to T_1 for trityl-CH_3, 25DTBSQ and mHCTPO at X-band and VHF..... 52

Table 4.1 Hyperfine splitting constants (G) for $aTAM_4$ 60

Table 4.2 Hyperfine splitting constants (G) for $aTAM_5$ 60

Table 4.3 T_2 values in (μs) for the center field line of 0.1 mM $aTAM_4$ obtained by echo decay at X-Band 61

Table 4.4 T_2 values in (μs) for the high field line of 0.1 mM $aTAM_4$ obtained by echo decay at X-Band 61

Table 4.5 pH dependence of T_1 and T_2 for $aTAM_4$ at X-band 62

Table 4.6 pH dependence of T_1 and T_2 values forTAM_5 at X-band 62

Table 4.7 Comparison of T_1 and T_2 for Trityls at X-band 63

Table 4.8 T_1 values in (μs) for the center field line of 0.1 mM $aTAM_4$ obtained by inversion recovery at X-band 63

Table 4.9 T_1 values in (μs) for the high field line of 0.1 mM $aTAM_4$ obtained by inversion recovery at X-band 64

Table 4.10 T_1 values in (μs) for the center field line of 0.1 mM $aTAM_4$ obtained by saturation recovery at X-band 64

Table 4.11 Spin packet ΔBsp for $aTAM_4$ calculated from T_2 65

Table 4.12 Spin packet ΔB_{sp} for $aTAM_5$ calculated from T_2 66

Table 5.1 Parameters for CW projections with time comparable to rapid scan 72

Table 5.2 Parameters for CW projections with longer averaging time 73

Table 5.3 Imaging parameters to collect the image in Figure 5.6 81

Table 5.4 Imaging parameters for full spectrum imaging algorithm 85

Table 6.1 Scan frequencies used and the frequency of the coherence signal 101

Table 6.2 The rate of the scan and coherence frequency converted into gauss 102

List of Figures

Figure 1.1 In the presence of a magnetic field the electron spin states split into two different energy levels: parallel and anti-parallel to the magnetic field vector……. ……..3

Figure 1.2 The energy level diagram showing the Boltzmann distribution at thermal equilibrium……...6

Figure 1.3 Saturation recovery experiment to measure T_1 ……..10

Figure 2.1 Structures of nitroxide studied at X-band……17

Figure 2.2 Field swept echo detected spectrum for 35 µM ^{14}N-mHCTPO in H_2O at X-band……19

Figure 2.3 Field swept echo detected spectrum for 35 µM ^{15}N-mHCTPO in H_2O at X-band……20

Figure 2.4 Structures of nitroxide radicals studied at X-band by saturation recovery…..23

Figure 2.5 CW spectrum for 0.5 mM Proxyl in H_2O at X-band……...25

Figure 2.6 CW spectrum for 0.18 mM ^{14}NPDT in 44% glycerol at X-band ……...26

Figure 2.7 CW spectrum for 0.5 mM nitronyl nitroxide in 2mM NaOH at X-band…….27

Figure 2.8 CW spectrum for 0.18 mM TPHIO in toluene at X-band……...28

Figure 3.1 Structures of the semiquinones studied……...35

Figure 3.2 CW spectra of semiquinones obtained with 0.5 G modulation amplitude…..38

Figure 3.3 CW spectra of semiquinones obtained with 0.05 G modulation amplitude…39

Figure 3.4 25DTBSQ stability monitored for 25 days……..40

Figure 3.5 Frequency dependence of $1/T_1$ for 25DTBSQ in alcohols at 293 K……...42

Figure 3.6 Frequency dependence of $1/T_1$ for 26DTBSQ in alcohols at 293 K……...43

Figure 3.7 Frequency dependence of $1/T_1$ for TMBSQ in alcohols at 293 K……..44

Figure 4.1 Structures of trityl TAM and aTAM radicals……..57

Figure 4.2 X-band CW spectra of $aTAM_4$. (A) at pH 8.5, (B) at pH 7.5,and (C) at pH 6.5. …….....58

Figure 4.3 X-band CW spectra of $aTAM_5$ (A) at pH 9.0, (B) at pH 8.2, and (C) at pH 6.4……...59

Figure 5.1 CW spectrum for two tubes containing 0.2 mM ^{15}N-PDT in H_2O……..70

Figure 5.2 Rapid scan spectra of the same two tubes of 0.2 mM ^{15}N-PDT in H_2O……..71

Figure 5.3 Projections as a function of the projection number from 1 to 18 and the resulting 2D spectral-spatial images……..75

Figure 5.4 2D spectral-spatial image of ^{15}NPDT, linewidth, and distance between the tubes……...77

Figure 5.5 2D spectral-spatial image of a phantom consisting of two tubes of 0.5 mM $aTAM_4$…….....82

Figure 5.6 2D spectral-spatial image of phantom consisting of pH=7.0 and pH=7.2 $aTAM_4$ radicals……..86

Figure 6.1 Rapid scan spectrum for 25DTBSQ at X-band with scan frequency of 2.6 KHz and 10 G sweep width……...91

Figure 6.2 Rapid scan spectrum for 25DTBSQ at X-band with scan frequency of 2.7 KHz and 10 G sweep width……...92

Figure 6.3 Rapid scan spectrum for 25DTBSQ at X-band with scan frequency of 2.9 KHz and 10 G sweep width…….. ……93

Figure 6.4 Rapid scan spectrum for 25DTBSQ at X-band with scan frequency of 3.5 KHz and 10 G sweep width. ……. ……...94

Figure 6.5 Rapid scan spectrum for 25DTBSQ at X-band with scan frequency of 7.7 KHz and 10 G sweep width……...95

Figure 6.6 Rapid scan spectrum for 25DTBSQ at X-band with scan frequency of 19.8 KHz and 10 G sweep width……...96

Figure 6.7 Rapid scan spectrum for 25DTBSQ at X-band with scan frequency of 41.6 KHz and 10 G sweep…….97

Figure 6.8 Spin coherence from the low field hyperfine line obtained with 7.7 KHz and 2 G sweep width……98

Figure 6.9 Spin coherence from the center field hyperfine line obtained with 7.7 KHz and 2 G sweep width……..99

Figure 6.10 Spin coherence signal from high field hyperfine line obtained with 7.7 KHz and 2 G sweep width……100

Figure 6.11 The dependence of the frequency of the coherence signal on the scan frequency……..101

Figure 6.12 Relationship between the scan rate and the coherence frequency in units of gauss…….102

Figure 6.13 Rapid scan spectrum for TMBSQ at X-band with scan frequency of 7.7 KHz and 10 G sweep width ……103

Figure 6.14 Rapid scan spectrum for TMBSQ at X-band with scan frequency of 20.8 KHz and 10 G sweep……...104

Figure 6.15 Rapid scan spectrum for TMBSQ at X-band with scan frequency of 41.6KHz and 10 G sweep width……..105

Figure 6.16 Rapid scan spectrum for TMBSQ at X-band with scan frequency of 2.6 KHz and 10 G sweep width……..106

List of Abbreviations, Acronyms, and Constants

25DTBSQ	2,5-Di-*t*-butyl-1,4-benzosemiquinone
26DTBSQ	2,6-Di-*t*-butyl-1,4-benzosemiquinone
$\bar{A}$	Average nitrogen hyperfine
A	Hyperfine splitting
A_i	Nitrogen hyperfine coupling component i=x, y ,z
Amp	Ampere
$aTAM_4$	Amino substituted triarylmethyl radical in (figure 4.2)
$aTAM_5$	Amino substituted triarylmethyl radical in (figure 4.3)
B_0	Static magnetic field
B_1	RF or microwave magnetic field
c_{slip}	Slip coefficient
CLR	Cross loop resonator
FID	Free induction decay
h	Planck's constant
i.d.	Inner diameter
J(ω)	Spectral density function
k	Boltzmann's constant
L-band	1-2 GHz
o.d.	Outer diameter

PDT	4-oxo-2,2,6,6-tetra-perdeuteromethyl- piperidinyl-oxyl-d_{16}
Proxyl	3-carboxy-2,2,5,5-tetramethyl-1-pyrrolidinyloxyl
Q- band	Typically 34 to 35GHz for EPR
S-band	2-4 GHz
S/N	Signal-to-noise
T_m	Phase memory time
TMBSQ	2,3,5,6-tetramethoxy-1,4-benzosemiquinone
TPHIO	1,1,3,3-tetraphenylisoindolin-2-yloxyl
Tris	2-amino-2-hydroxymethyl-propane-1,3-diol
Trityl	Triarylmethyl
TWT	Traveling-wave tube amplifier
VHF	Very high frequency = 250 MHz For EPR
V	the molecular volume
X-band	9-10 GHz
g	g-value
g_e	Free-electron g-value = 2.0023
ΔB_{sp}	Spin packet linewidth
η	Viscosity
γ	Gyromagnetic ratio
ν	Frequency
τ	Time between pulses
τ_c	Tumbling correlation time

τ_c^0	Pre-exponential factor
τ_R	Rotational correlation time
ω	Larmor frequency

Chapter One: Introduction

1.1 Electron Paramagnetic Resonance (EPR)

EPR is a spectroscopic technique that is widely used to characterize samples with unpaired electrons such as radicals and paramagnetic metals. The spectra are simpler to interpret when there is a single unpaired electron with S=1/2 than where there are multiple electron spins. The origin of the EPR signal is the interaction between the magnetic moment of the unpaired electron and a magnetic field, B_0. In the absence of a magnetic field the electron spins have random orientation and the energy levels are degenerate. In the presence of a magnetic field the two energy levels split into two states that commonly are designated as α, β. The energy when the spin is aligned with the magnetic field (m_S = -1/2 (β)) is lower than when it is aligned against the magnetic field vector (m_s = +1/2 (α)) as shown in Figure 1.1. This splitting is called the Zeeman Effect. The splitting is proportional to the strength of the magnetic field [1]. The energy separation is shown in Eq. (1.1).

$$\Delta E = g \mu_B B_0 \quad (1.1)$$

The transition between those two states requires that $\Delta E = h\nu$ as shown in Eq. (1.2). This resonant absorption of energy is the origin of the EPR signal.

$$\Delta E = h\nu = g \mu_B B_0 \quad (1.2)$$

h is Planck's constant, ν is the electromagnetic frequency, μ_B is the electron Bohr magneton, and g is the g-factor.

The EPR signal can be obtained by changing the magnetic field and holding the microwave frequency constant, or changing the microwave frequency and holding the magnetic field constant. Because of hardware limitations it is difficult to sweep the microwave frequency. Therefore sweeping the magnetic field is the approach that is used for most EPR spectrometers.

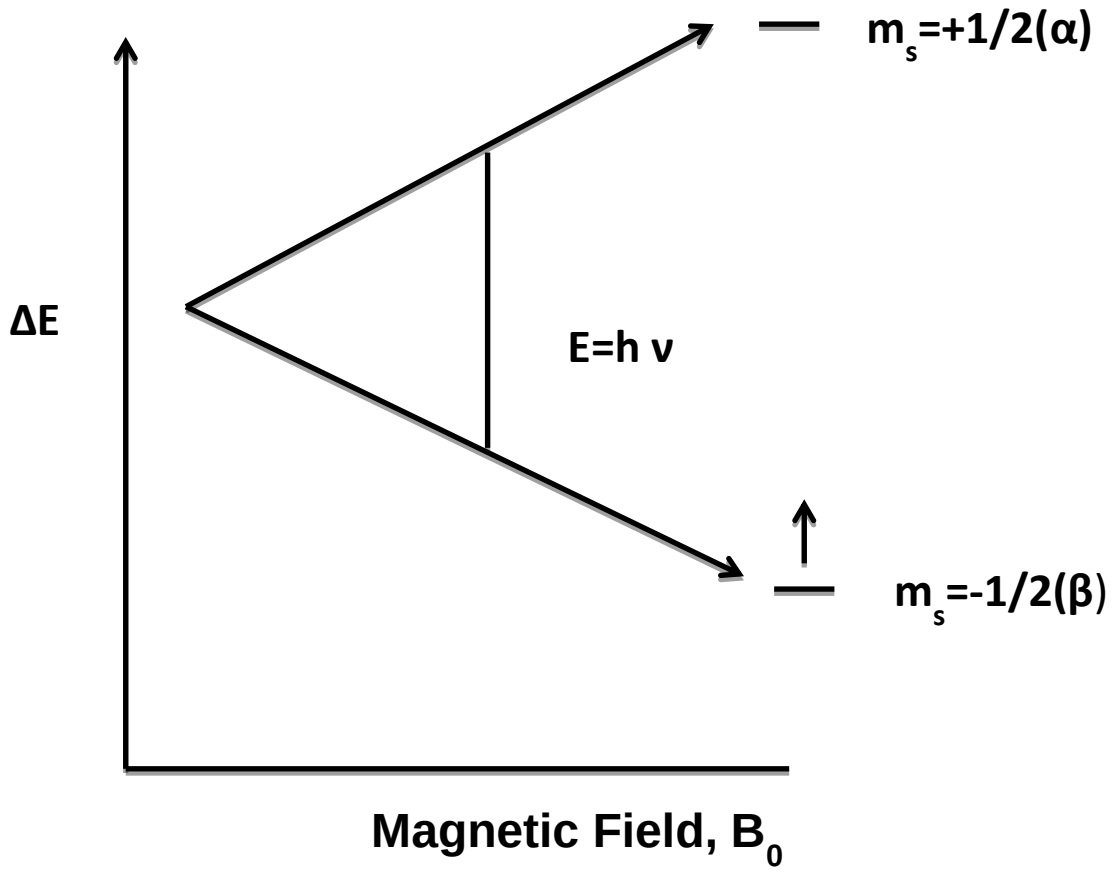

Figure 1.1 In the presence of a magnetic field the electron spin states split into two different energy levels: parallel and anti-parallel to the magnetic field vector.

The g-factor

The resonance field at which the EPR signal occurs is different for different microwave frequencies, so it is not a fingerprint or characteristic of the sample studied by EPR. By contrast, the g-factor is a fingerprint of the unpaired electron center.

$$g = h\nu/\mu_B B_0 \quad (1.3)$$

The g-factor is an indication of the coupling between the spin and the orbital angular momenta. The g value varies based on the environment of the unpaired electron.

For a free radical, the g-factor is close to the free electron value of 2.0023. However the g-factors for transition metal complexes deviate significantly from the free electron value, and may depend strongly upon the geometry. In a crystal or in an immobilized sample the g-factor may be anisotropic and depend on the orientation of the molecule with respect to the magnetic field [1]. g-anisotropy is averaged for rapidly tumbling radicals in solutions.

Hyperfine Coupling

Additional identification for a compound beside the g-factor is the hyperfine structure. In most molecules there are nuclei that have magnetic moments, such as ^{1}H, ^{13}C, ^{14}N, and ^{15}N. The electron not only experiences the external magnetic field, it also experiences an additional local magnetic field that is produced by the nuclei surrounding it. The hyperfine structure is a result of the interactions between the electron and the nuclei. This interaction causes splitting in the spectrum, and the number of hyperfine lines is equal to $2nI+1$, where n is the number of the symmetry equivalent nuclei and I is the nuclear spin. The magnitude of the local magnetic field depends on the type of the nucleus and the spin density on it [1]. The hyperfine coupling constant could be isotropic or anisotropic. The anisotropy is averaged by tumbling in solution just like g-anisotropy [2].

Electron Relaxation Times

Relaxation times are other features that characterize the interaction between the electron spins and the surroundings or with each other [2]. The spins distribute between the two energy states α, β according to the Boltzmann distribution with excess in the lower energy state that is parallel with the magnetic field. This distribution is in thermal equilibrium Eq. (1.4).

$$\frac{Na}{Nb} = e^{-\Delta E/KT} \tag{1.4}$$

where N_a is the spin population in the α state (with higher energy) and N_b is the population in the lower energy state β. ΔE is the energy difference between the two states, k is Boltzmann's constant and T is temperature. At thermal equilibrium there is a small excess of spins in the lower energy state which results in a net magnetization that is aligned with the external magnetic field. The direction of the external field is designated as the Z-direction and the magnetization vector is denoted as the Z-vector shown in Figure 1.2. Applying a pulse heats the system and perturbs the thermal equilibrium rotating the Z-vector from its orientation. After the microwave pulse is switched off the magnetization vector returns to equilibrium in two relaxation processes.

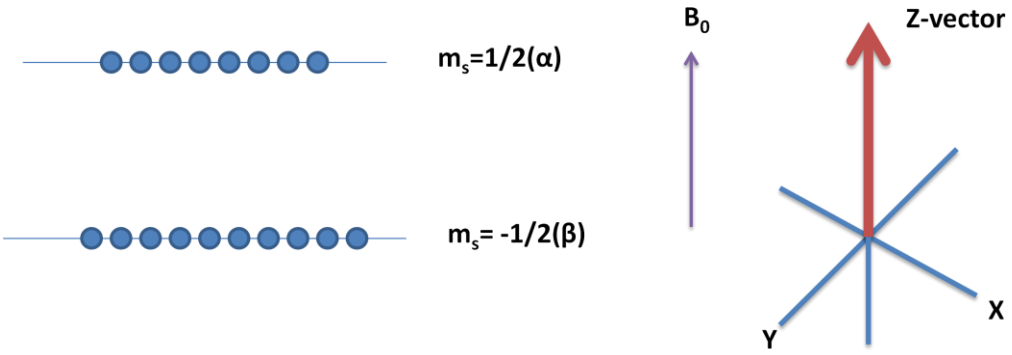

Figure 1.2 The energy level diagram on the left shows the Boltzmann distribution of electron spins at thermal equilibrium. On the right, the net magnetization is represented as vector aligned with the magnetic field, which is defined as the z-direction.

Spin–lattice relaxation, T_1

The magnetization returns to equilibrium and recovers the equilibrium orientation of the magnetization vector by dissipating the energy to the surroundings, which is called the lattice. This process is called spin-lattice relaxation and the time constant for the process is T_1. Since this process includes heat transfer, it is an enthalpic process [2]. Information about molecular rotation and molecular collision can be revealed by T_1 measurements.

Spin-spin relaxation, T_2

The second relaxation process is dephasing of the magnetization in the X-Y plane by interactions between the spins. This process is called spin-spin relaxation and the time constant is T_2. The interaction could be between electron spins or between electron and nuclear spins. It can provide information about the presence of nuclear spin in the system. Spin–spin relaxation is an entropic process since it involves losing the phase coherence [2]. The time constant for a spin echo decay is called the phase memory time T_m. In a solid at low temperature T_m is dominated by nuclear spin flip processes [3]. Dynamic processes including motions of nuclei that are coupled to an unpaired electron also can contribute to T_m. If a system has no or only a few nuclear spins $T_m = T_2$ and the spin–spin relaxation in a solid would be determined by the interaction between the electron spins as shown in Eq. (1.5).

$$T_2 = hr^3/2\pi\mu^2 \tag{1.5}$$

where h is Planck's constant, r=distance between unpaired spins, and μ is the electron magnetic moment [4].

In solution, the time constant for the spin echo decay is designated as T_2.

The spin packet linewidth can be calculated from T_2 according to Eq. (1.6)

$$\Delta B_{sp} = \frac{2}{\sqrt{3}\gamma T_2} \tag{1.6}$$

where ΔB_{sp} is the spin packet linewidth and γ is the gyromagnetic ratio. This equation is applicable only to Lorentzian lines which are said to be homogenously broadened. For many organic radicals unresolved nuclear hyperfine interactions contribute to the

linewidths which have shapes that are intermediate between Lorentzian and Gaussian and are said to be inhomogeneously broadened.

1.2 EPR Methods

Continuous wave (CW)

In CW EPR the magnetic field is scanned at constant microwave frequency until the resonance condition is met. This occurs when the energy of the microwave radiation matches the energy difference between the two spin states. This is the condition for which the resonance in the sample is detected. The signal detected in this experiment has an enormous amount of information about the sample (g-factor, hyperfine coupling constant, tumbling). To obtain undistorted CW spectra, knowledge about the relaxation time is required. Pulsed EPR methods to determine the relaxation times are described in the following section.

Pulse

T_2 and T_1 can be calculated directly by pulse methods. T_2 can be measured by spin echo decay, and T_1 can be measured by inversion recovery and both methods involve forming an echo as discussed below.

Spin echo decay

In this experiment the echo is formed from a two-pulse 90^o - 180^o sequence. The first pulse rotates the net spin vector from the Z-direction to the X-Y plane, after which the spins start to dephase. A refocusing 180^o pulse is then applied to flip the spins in the opposite direction. The spins are still dephasing, but now in the direction that refocuses to

form the echo. This happens at a time 2τ that is twice the time τ between the pulses. Increasing the time between the pulses allows more time for dephasing, which decreases the amplitude of the echo. In solution the time constant of this decay is T_2.

Inversion recovery

In an inversion recovery experiment a three pulse sequence is used with 180^o-90^o-180^o pulses. The first 180^o pulse is called the inverting pulse, which inverts the net spin vector to the - Z-direction. The following two pulses form the spin echo. Increasing the time between the first pulse 180^o and the second pulse allows more time for the magnetization to return to equilibrium. Monitoring the echo intensity as a function of the time between the first and second pulses generates an inversion recovery curve. In the ideal case the time constant of the recovery is T_1. Because of the short inverting pulse this method of measuring T_1 is subject to the effect of spectral diffusion. Spectral diffusion is any process that takes spins off resonance. These processes can cause the time constant for the inversion recovery experiment to be shorter than be the true T_1. An alternative method to obtain the true T_1 is called saturation recovery.

Saturation Recovery

In this experiment a long microwave pulse is used to saturate the EPR transition and cause the two energy states to have equal population as shown in Figure 1.3. After the saturating pulse there is no net magnetization. The net magnetization that is generated from the difference in the populations described previously (Figure 1.2) is eliminated. After the saturating pulse is switched off, the net magnetization recovery is monitored at low non-saturating observing power. In the Bruker E580 and similar pulse

spectrometers, the high power pulses are produced with traveling wave tube (TWT) amplifiers that limit the pulse length to 10 μs [1, 5]. The advantage of saturation recovery is that using a CW source permits long pulse lengths that minimize the effect from the spectral diffusion. If the saturating pulses are long enough, then all spins that are interchanged by the spectral diffusion processes are saturated. If the sample has very long relaxation times the observe power must be very low to avoid saturation of the spin system which shortens the observed recovery time [5].

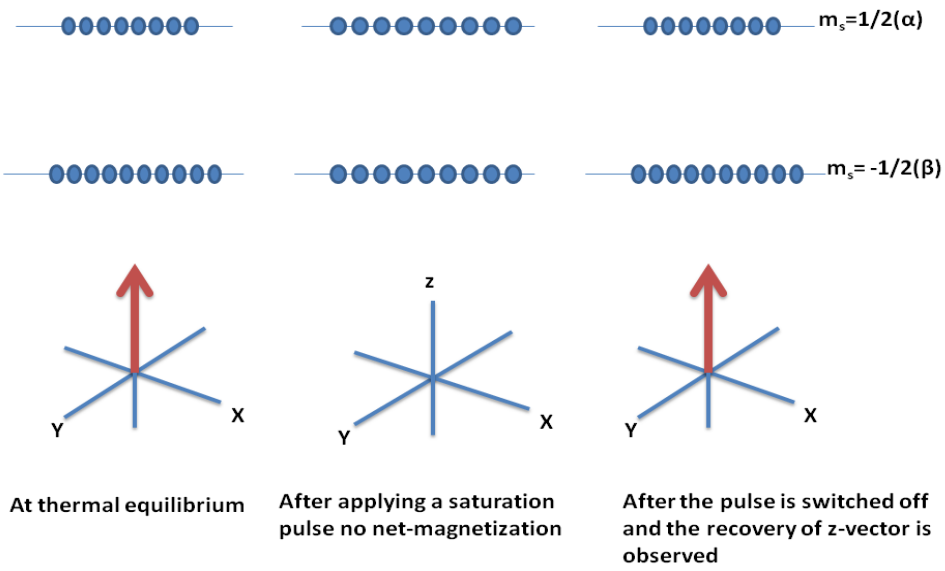

Figure 1.3 Saturation recovery experiment to measure T_1. Dots represent populations of electron spins. The upper section is an energy diagram.

Rapid Scan

Rapid scan–EPR is based on the phenomena of passage effects that were observed in NMR [6]. When the rate at which the magnetic field scans through resonance

is fast relative to electron spin relaxation rates, wiggles are observed after the magnetic field passes through resonance. The same phenomenon was observed in the early days of EPR. The first observation of "wiggles" in EPR was by Beeler et al. [7, 8].

Signals can be obtained by sweeping the magnetic field or microwave frequency [9] through resonance in times that are short relative to electron spin relaxation times. This signal is then deconvolved to provide the EPR absorption signal [10]. Rapid scan EPR has been developed in the Eaton laboratory at both VHF (250 MHz) and X-band frequency (~9.6 GHz).

In rapid scan the time spent on resonance is a very short, which permits the use of high power or high B_1 without saturating the signal. This led to improvements in the S/N for rapid scan relative to CW [11-13]. This is advantageous for samples with long spin-lattice relaxation times [14].

Rapid scan EPR is particularly advantageous for imaging because the amplitude of the absorption signal decreases approximately linearly with magnetic field gradient, whereas the amplitude of the first-derivative CW EPR decreases approximately quadratically. In this dissertation imaging with rapid scan was demonstrated to be a promising EPR imaging method. EPR is a quantitative technique that is widely used to obtain information with different spectroscopic methods, each of which is better suited for obtaining specific types of information. In this dissertation most of the methods described in this chapter were used.

In this dissertation the work is divided into projects in six chapters. Chapter two describes relaxation measurements for nitroxide radicals tumbling rapidly in solution to

understand the relation between the structural features and the relaxation times. This understanding is needed to design a suitable in vivo imaging nitroxide probe. A few measurements also were performed for immobilized samples. Chapter three includes the synthesis and frequency dependence of spin lattice relaxation of three transient semiquinone radicals, which provides new insight about the relaxation mechanism of this class of biologically important radicals. In chapter four the relaxation times for a dual function probe with sensitivity to both pH and oxygen, the amino derivatives of trityl (aTAM) have been characterized to investigate the possibility of using these types of radicals in pulsed EPR. EPR imaging applications are described in chapter five. Chapter six describes an interesting spin physics phenomenon that was observed in the rapid scan spectra for semiquinones.

Chapter Two: Relaxation Time Measurements for Nitroxide Radicals

2.1 Introduction

Nitroxide radicals have been developed extensively as EPR probes [15],[16]. The small size of these radicals and the ease of synthesis make them attractive probes for in vivo imaging. After the work by other research groups to enhance resistance to bio reduction, the next goal was to increase the relaxation times of the nitroxide to be suitable for pulsed in vivo imaging. Understanding the mechanisms of the relaxation and how it is related to structure will lead to the design of structures that increase the relaxation time for the nitroxide radicals. This will make several imaging applications feasible. Nitroxide radical structures can be designed for pH mapping through the change in the hyperfine splitting [17], monitoring local oxygen concentration through changes in linewidths or relaxation times [18], and measuring redox status through changes in rates of reduction [19].

In a joint project with Josh Biller and Virginia Meyer, relaxation times for several nitroxide radicals were studied with the aim of understanding the relaxation mechanisms. This chapter is a description of our work with an emphasis on my contributions. The project involved relaxation times measurements for six nitroxide radicals at X-band (9.4 to 9.8 GHz) at room temperature aiming to understand the relationship between spectral properties and relaxation mechanisms. A comparison of T_1 and T_2 obtained by different people for precision and to estimate the standard deviation was a primary aspect of this

project. Initial results were summarized in [20]. The study was extended to understand the relaxation mechanism for other nitroxide radicals and at a range of frequencies between 250 MHz and 34 GHz, which was published in [21, 22].

2.2 ^{14}N-mHCTPO and ^{14}N-Tempone-d_{16}

As mentioned above, a primary effort was comparison of the results obtained by different people and on different instruments. Spin-spin relaxation T_2 by echo decay, and spin-lattice relaxation time T_1 by inversion recovery at X-band were measured for ^{14}N-mHCTPO and ^{14}N-Tempone. My role was to measure T_2 and T_1 on the Bruker E580 spectrometer.

Materials and Methods

Spin-lattice relaxation times were measured by inversion recovery and spin–spin relaxation time by spin echo decay for two nitroxide radicals: 0.4 mM ^{14}N-mHCTPO in toluene and 0.27 mM ^{14}N-Tempone-d_{16} in water. ^{14}N-Tempone-d_{16} was purchased from CDN Isotopes (Quebec, Canada) and ^{14}N-mHCTPO was provided by Prof. Halpern (University of Chicago). Solutions were deoxygenated by freeze pump thaw. The structures are shown in Figure 2.1.

Results and Discussion

T_2 and T_1 values measured by spin echo decay or inversion recovery, respectively, for the three lines of PDT and ^{14}N-mHCTPO are shown in Table 2.1 and 2.2. The ± refers to one standard deviation for 2 to 3 replicates.

Table 2.1 Nitroxide T_2 and T_1 values (μs) determined at X-band (0.27mM)

^{14}N Tempone-d_{16}	T_2	T_1
Low Field	0.59±0.03	0.62±0.01
Center Field	0.57±0.03	0.56±0.02
High Field	0.45±0.03	0.52±0.01

Table 2.2 Nitroxide T_2 and T_1 values (μs) determined at X-band (0.4mM)

^{14}N-mHCTPO	T_2	T_1[#]
Low Field	0.56±0.01	0.56
Center Field	0.47±0.06	0.53
High Field	0.43±0.01	0.49

[#] T_1 values do not have replicates.

The results from different people were in good agreement within about 5% uncertainty.

2.3. Comparison of the Results from Different Instruments

Spin–lattice relaxation times for ^{14}N-mHCTPO in toluene were measured using saturation recovery on two spectrometers - the Bruker E580 and the locally designed saturation recovery spectrometer [23].

Table 2.3 T_1 values (μs) for ^{14}N-mHCTPO (0.4 mM in toluene) determined at X-band using different instruments

Instrument	Low Field	Center Field	High Field
Homebuilt SR	0.62±0.02	0.55±0.04	0.45±0.01
E580 SR	0.56±0.04	0.53±0.03	0.46±0.03

2.4 Relaxation Times Measurements for Six Nitroxide Radicals at X-band at Ambient Temperature.

Nitroxides studied

The study included nitroxides shown in Figure 2.1. Each was studied with both ^{14}N and ^{15}N isotopes to test the isotope effect on the relaxation mechanism. Substitution of ^{1}H by ^{2}H results in narrower EPR signals and improved S/N, so the study was carried out on deuterium-substituted nitroxide. Most of the nitroxides selected for the study have been used for imaging applications [17-19]. For instance mHCTPO has been used as a probe to follow the oxygen concentration.

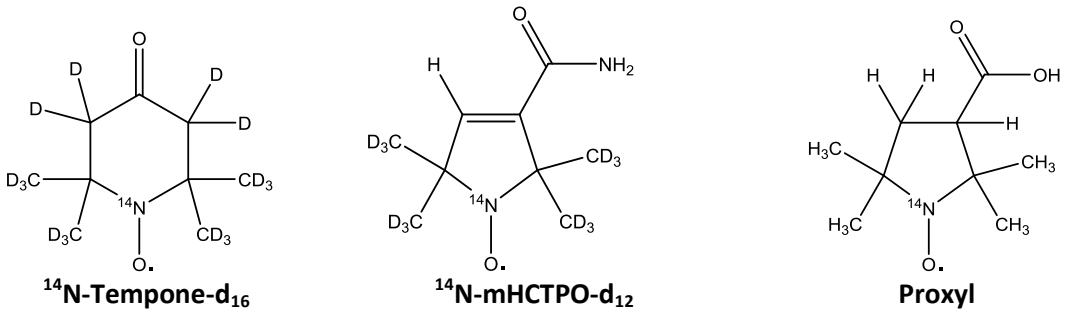

Figure 2.1 Structures of nitroxide studied at X-band.

Materials and Methods

Compound **1** and its ^{15}N analog were purchased from CDN Isotopes (Quebec, Canada), compound **2** with natural isotope abundance nitrogen and its ^{15}N analog were prepared as previously reported [15] and provided by Prof. Halpern (University of Chicago). Compound **3** and its ^{15}N analog were prepared as reported in [16]. Solutions were deoxygenated by passing N_2 gas over the sample using a thin Teflon tube that passed into the quartz sample tube, aligned with the Teflon tube that contains the sample.

Spectroscopy

T_2 relaxation times were measured by two-pulse electron spin echo and T_1 by inversion recovery on a locally-built pulsed spectrometer [24] with a Bruker ER4118-X-MS5 split ring resonator. A 1 KW amplifier was used. The experiments were performed at room temperature.

Result and Discussion

Examples of field sweep echo-detected spectra obtained by 40 ns $\pi/2$ pulse are shown in Figures 2.2-2.3. Spectra are similar for the three nitroxides. Hyperfine splittings are reported in [20]. The echo detected spectra were used to select the magnetic fields at which the relaxation time measurements were performed.

T_1 and T_2 values for the nitroxides studied in water at 125 µM, 67 µM, 62 µM, 60 µM, 35 µM, 34 µM, 33 µM, and 31 µM are shown in the Tables 2.4-2.7. Values reported without uncertainties were measured one time. Values with uncertainty have at least two replicates. The concentration dependence of T_1 is equal to or smaller than for T_2 (Table 2.8). PDT and m-HCTPO show more concentration dependence than Proxyl which has a negative charge on the carboxylic group that decreases the probability of collisions. This is similar to the trityl radicals that are large and negatively charged, which prevents collisions and makes the relaxations less concentration-dependent [25]. Early studies of semiquinone relaxation times showed no concentration dependence, which was attributed to the solvent cage [26]. This was also observed in the study of the semiquinone relaxation in this dissertation (Chapter 3). Relaxation times are longer for ^{15}N- than for ^{14}N-nitroxides, as predicted by models. A T_1 dependence on nitrogen m_I was observed. This dependence was reproducible in several replicate measurement and different people doing the experiments. A dependence of T_1 on m_I was observed in an early study of nitroxides, but the difference was comparable to the experimental uncertainty [27]. Recent studies of nitroxide in viscous solutions did not show a dependence of T_1 on m_I

[28, 29]. The dependence of T_2 on m_I has been studied extensively by Freed and co-workers [30-33] and is used to determine the tumbling correlation time.

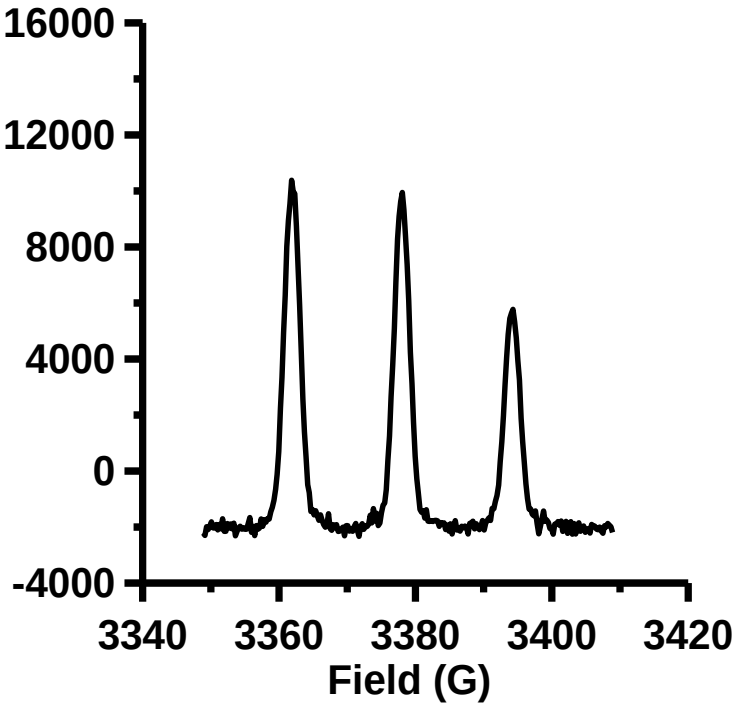

Figure 2.2 Field swept echo detected spectrum for 35 μM ^{14}N-mHCTPO in H_2O at X-band

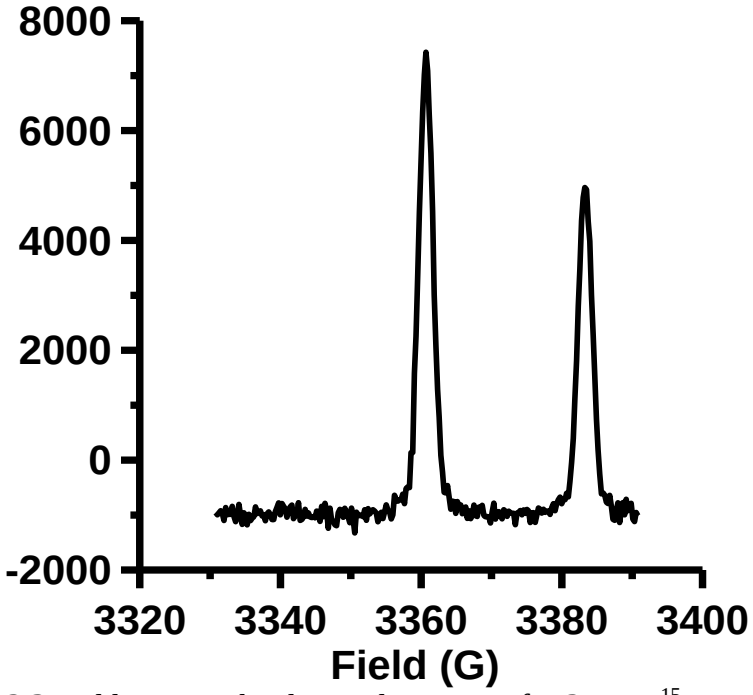

Figure 2.3 Field swept echo detected spectrum for 35 μM ^{15}N-mHCTPO in H_2O at X-band

Table 2.4 T_2 (μs) at X-band for ^{14}N-nitroxides

Nitroxide	Conc. (μM)	Low field	Center field	High field
Proxyl	125	0.69	0.65	0.42
	62	0.71	0.66	0.41
PDT	67	0.74±0.03	0.68±0.01	0.52±0.01
	34	0.74±0.01	0.72±0.01	0.55±0.02
mHCTPO	70	0.69	0.63	0.48
	35	0.76±0.04	0.72±0.04	0.49±0.03

Table 2.5 T_1 (μs) at X-band for ^{14}N-nitroxides

Nitroxide	Conc. (μM)	Low field	Center field	High field
Proxyl	125	0.88	0.73	0.69
	62	0.93	0.79	0.68
PDT	67	0.83±0.03	0.74±0.02	0.67±0.01
	34	0.85±0.02	0.76±0.02	0.66±0.01
mHCTPO	35	0.92±0.01	0.83±0.01	0.70±0.01

Table 2.6 T_2 (μs) at X-band for ^{15}N-nitroxides

Nitroxide	Conc. (μM)	Low field	High field
Proxyl	125	0.94	0.58
	62	0.96	0.64
	31	0.97±0.03	0.59±0.03
PDT	125	0.66	0.52
	63	0.71±0.04	0.57±0.01
	33	0.88±0.01	0.64±0.03
	31	0.88±0.01	0.69±0.03
mHCTPO	60	0.85±0.01	0.59±0.02
	35	0.94±0.01	0.62±0.02

Table 2.7 T_1 (μs) at X-band for ^{15}N-nitroxides

Nitroxide	Conc. (μM)	Low field	High field
Proxyl	125	1.09	0.92
	62	1.18±0.07	0.94±0.06
	31	1.29±0.01	1.05±0.02
PDT	125	0.73	0.62
	63	0.88±0.03	0.72±0.04
	33	0.98±0.05	0.81±0.02
	31	1.01±0.03	0.83±0.04
mHCTPO	60	1.06±0.04	0.88±0.06
	35	1.15±0.03	0.92±0.03

Table 2.8 Slopes of plots of $1/T_2$ and $1/T_1$ vs. concentration

	Low field		High field	
Radical	$1/T_2$	$1/T_1$	$1/T_2$	$1/T_1$
^{15}N-Proxyl	$4x10^{-4}$	$2x10^{-3}$	$1x10^{-3}$	$1x10^{-3}$
^{15}N-PDT	$4x10^{-3}$	$4x10^{-3}$	$5x10^{-3}$	$4x10^{-3}$
^{15}N-mHCTPO	$5x10^{-3}$	$3x10^{-3}$	$3x10^{-3}$	$2x10^{-3}$

2.5 Spin-lattice Relaxation Times by Saturation Recovery

Spin lattice relaxation times were obtained by saturation recovery at X-band to be compared to the spin-lattice relaxation obtained by inversion recovery. Spectral diffusion processes may contribute to the recovery curves obtained by inversion recovery. If the saturating pulse is sufficiently long, saturation recovery should give the true spin-lattice relaxation time. Obtaining the same value from inversion recovery and saturation recovery validates the results from inversion recovery.

Nitroxide studied

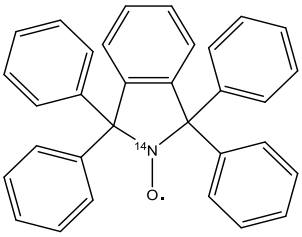

TPHIO

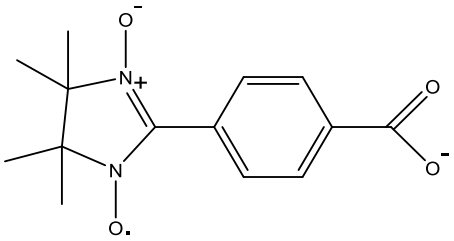

Nitronyl

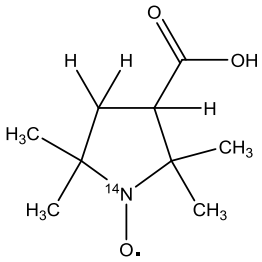

Proxyl

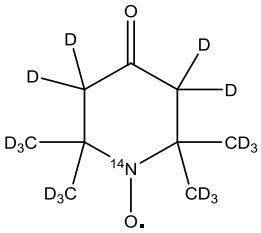

(PDT) ^{14}N-Tempone-d$_{16}$

Figure 2.4 Structures of nitroxide radicals studied at X-band by saturation recovery.

Materials and Methods

Samples

TPHIO was prepared as previously reported [18]. PDT was purchased from CDN Isotopes (Quebec, Canada). Nitronyl nitroxide and Proxyl were prepared by Prof. Gerald Rosen at the University of Maryland [16, 21].

The concentrations of the samples were ^{14}NTPHIO, 0.18 mM in toluene; ^{14}NPDT, 0.18 mM in 44% Glycerol; nitronyl nitroxide, 0.5 mM in 2 mM NaOH ; and Proxyl, 0.5 mM in H_2O.

Spectroscopy

The measurements, except for Proxyl, were performed on the homebuilt saturation recovery spectrometer with an E231 resonator [23]. For Proxyl the saturation recovery experiments were performed on a Bruker E580 spectrometer. For PDT in 44% glycerol, Proxyl or nitronyl nitroxide in water, samples in thin-wall Teflon tubing were placed into 4 mm EPR tubes and degassed using constant purging with N_2 gas. TPHIO in a 4 mm EPR tube was degassed by several freeze- pump- thaw cycles and flame sealed. CW spectra for the four radicals recorded on the homebuilt saturation recovery spectrometer are shown in Figures 2.5-2.8.

Spin-lattice T_1 by saturation recovery for TPHIO was obtained under the following conditions: pump power 16 dB, observe power 18 dB, 1 dB power on the bridge, repetition time 201 μs and pump time 20 μs, 10000 averages, scan time 20.16 μs, and 1008 data points.

For ^{14}NPDT in 44% glycerol, data were obtained with 12 dB pump and 18 dB observe power, 401 μs repetition time, 20 μs pump time and 40000 averages. The number of points was 256 and the scan time was12.8 μs.

For nitronyl, data were obtained with 12 dB pump power, 18 dB observe power, 601 μs repetition time, 20 μs pump time, 1008 points with and 20 ns time base, 20 μs scan time and 80000 averages.

T_1 for Proxyl was obtained on the Bruker E580 spectrometer using the following parameters: 25 dB observe power, 12 dB pump power, P^0 = 1 μs, d_5= 1μs, d_0= 940 ns, 50 ns time base, 256 points and 8000 averages.

Results and Discussion

Saturation recovery experiments were performed to measure the spin–lattice relaxation time T_1 of four nitroxide radicals. Table 2.9 shows T_1 values for the low-field, centerfield, and high-field lines, respectively. T_1 measurements for nitronyl were performed on the center line only. The X- band inversion recovery curves fit well with a single exponential, as expected in the regime where $\omega\tau_R \leq 1$, where τ_R is the tumbling correlation time. Saturation recovery curves fit well with a single exponential and the values are in good agreement with the values obtained by inversion recovery.

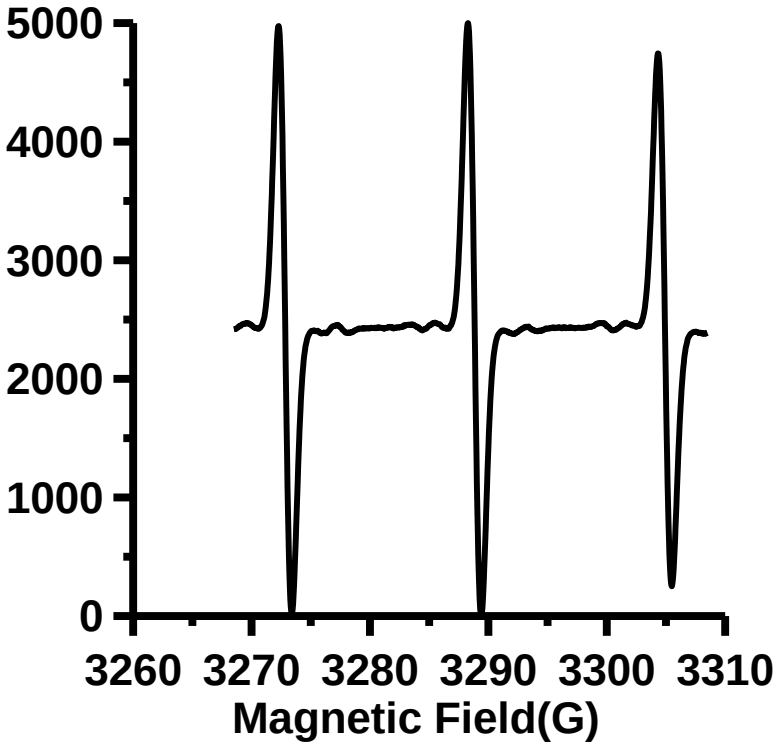

Figure 2.5 CW spectrum for 0.5 mM Proxyl in H_2O at X-band obtained with 0.05 G modulation amplitude, 40 G sweep width, 60 s sweep time, 1024 points, and 20 dB power attenuation.

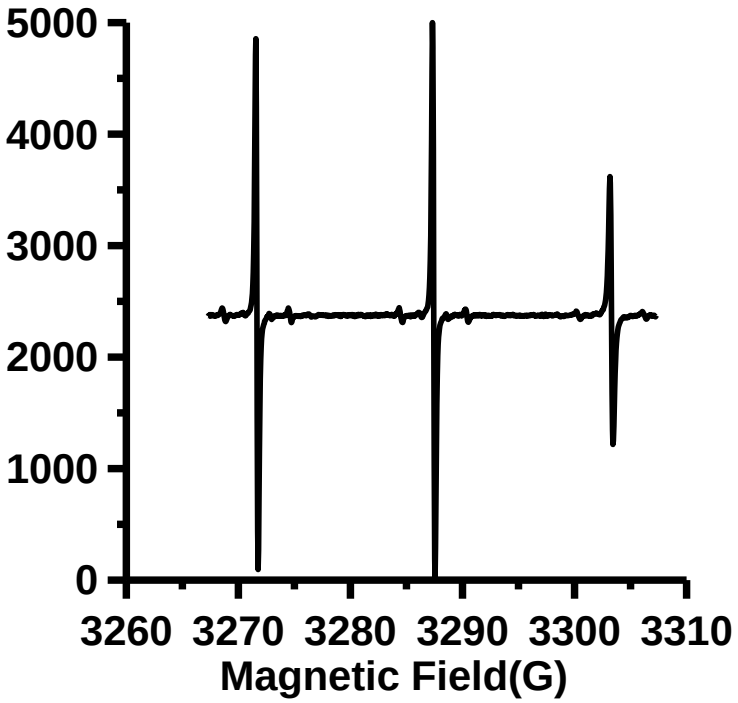

Figure 2.6 A CW spectrum for 0.18 mM ^{14}NPDT in 44% glycerol at X-band obtained with 0.025 G modulation amplitude, 40 G sweep width, 60 s sweep time, 1024 points, and 20 dB power attenuation.

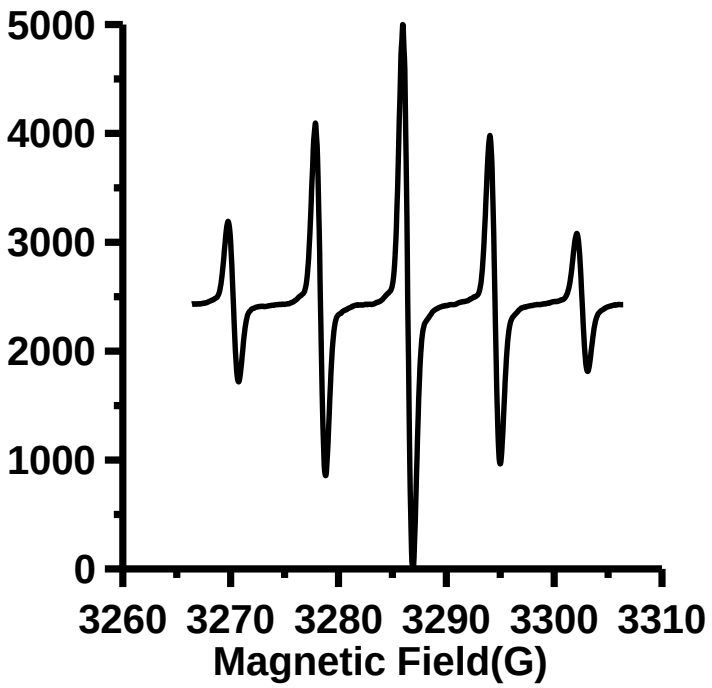

Figure 2.7 CW spectrum for 0.5 mM nitronyl nitroxide in 2mM NaOH at X-band obtained with 0.16 G modulation amplitude, 40 G sweep width, 60 s sweep time, 1024 points, and 22 dB power attenuation.

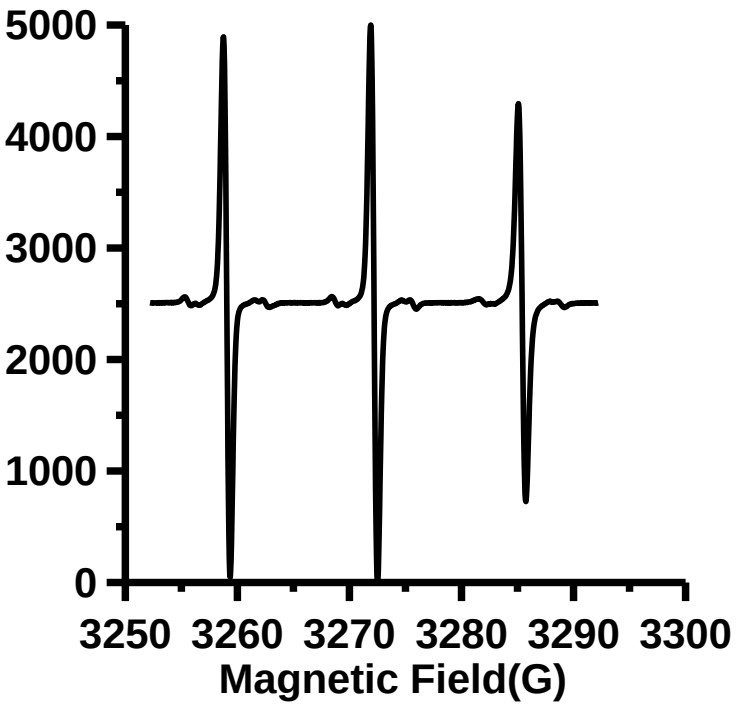

Figure 2.8 CW spectrum for 0.18 mM TPHIO in toluene at X-band obtained with 0.02 G modulation amplitude, 40 G sweep width, 60 s sweep time, 1024 points, and 23 dB power attenuation.

Table 2.9 NitroxideT_1 (μs) values determined by saturation recovery at X-band*

Radical	Conc. (mM)	Low field	Center field	Low field
TPHIO (toluene)	0.18	1.91±0.09	2.25±0.14	1.86±0.21
PDT (44%Glycerol)	0.18	1.43±0.12	1.52±0.03	1.30±0.14
Proxyl (H_2O)	0.5	0.712±0.05	0.699±0.05	0.623±0.07
Nitronyl	0.5	N/A	1.18±0.07	N/A

* T_1 values reported in this table were obtained by a single exponential fit

2.6 Relaxation Times for Immobilized Radicals

Introduction

Until 2013 rapid scan sweep width in the Eaton lab were limited to 55 G. Recent instruments modifications make it feasible to sweep 100-155 G. A major enabling technology was the use of Litz-wire in the scan coils [34]. One important class of organic radicals is immobilized nitroxide spin labels. After the hardware modifications and the developments of the rapid scan instrumentation, wide sweep for the full spectra for these radicals was demonstrated in a work by Zhelin Yu et al. [34]. In order to interpret rapid scan spectra, knowledge about the relaxation times is useful. As a part of this project my role was to measure the relaxation times of some of these immobilized radicals.

Materials and Methods

Samples

Nitroxides ^{14}N-PDT and ^{15}N-PDT were purchased from CDN isotopes (Quebec, Canada) prepared in sucrose octaacetate as reported in [35] . The preparation of the spin-labeled T4 lysozyme was performed at Vanderbilt University [36]. Crystals of malonic acid had been irradiated to 115 KGray.

Spectroscopy

T_2 and T_1 were measured by spin echo decay and inversion recovery on a locally-built pulsed X-band spectrometer with ER4118X-MS5 split ring resonator [24]. The measurements performed at ambient temperature. Values shown in tables 2.10 - 2.11 were measured using 40 ns $\pi/2$ pulse for all the samples except for the PDT sample. For

that sample 80ns pulse was used to reduce B_1 and thereby minimize the deuterium modulation that was observed in the echo decay.

Results and Discussion

Nitroxide T_1 increases as the tumbling correlation time becomes longer due to decreases in the contributions from spin rotation and modulation of the anisotropic nitrogen hyperfine interaction [22]. For the slower tumbling samples the recovery curves are not fit well with a single exponential so results from double exponentials are shown. These T_2 values in Tables 2.10-2.11 are not as long as at lower temperature due to incomplete immobilization that result in motional averaging of g and A-anisotropy

Table 2.10 T_2 values in (μs) at- X-band for immobilized samples

Sample	Single exponential	Double exponential	
		Short	Long
Irradiated malonic acid	3		
T4 lysozyme	0.52	0.49	0.92
^{15}N PDT in sucrose octaacetate	0.57	0.36	1.5
^{14}N PDT in sucrose octaacetate	0.77	0.28	1.8

Table 2.11 T_1 values in (μs) at X-band for immobilized samples

Sample	Single exponential	Double exponential	
		Short	Long
Irradiated malonic acid	31	27	50
T4 lysozyme	14	3.7	18
^{15}N PDT in sucrose octaacetate	4	1.5	5.8
^{14}N PDT in sucrose octaacetate	6	1.9	9.5

Chapter Three: Frequency Dependence of Electron Spin-lattice Relaxation for Semiquinones in Alcohol Solutions

3.1 Introduction

Semiquinones are ubiquitous in biology, from photosynthesis to environmental toxicology [37, 38]. They are involved in many electron transfer reactions [39, 40]. Semiquinones have been studied extensively by EPR [41], and their spin relaxation properties are important to understanding their EPR spectra. Semiquinones are useful for assigning mechanisms of electron spin relaxation because their g values are higher than for carbon-centered radicals, but their nuclear hyperfine couplings are smaller than for nitroxides.

Semiquinones were among the first species for which spin-lattice relaxation rates were measured directly by saturation recovery in fluid solution [42]. Extensive studies at X-band as a function of temperature and viscosity demonstrated that relaxation rates for a range of semiquinones in alcohol solutions could be fit with the relationship shown in Eq. (3.1) [26, 43-46].

$$\frac{1}{T_1} = \frac{AT}{\eta} + B\mathrm{e}^{-\Delta E/RT} \qquad (3.1)$$

where η is the viscosity of the solution, ΔE is about 1 kcal/mole (ΔE/R = 500 K), A and B were determined experimentally. There is general agreement that the term in T/η is due to spin rotation, which is usually written as in Eq. (3.2) [47, 48].

$$\frac{1}{T_1^{SR}} = \frac{\sum_{i=1}^{3}(g_i - g_e)^2}{9\tau_R} \tag{3.2}$$

where $i = x,y,z$ and g_e is 2.0023, and τ_R is the tumbling correlation time.

The origin of the second term in Eq. (3.1) was not well understood and has been attributed to hindered rotation [26, 46] and/or spin rotation [45]. A study at X- and Q-band of five semiquinones in glass-forming solvents between 25 and 295 K found that the dominant contributions to relaxation at 295 K were spin rotation and a local mode [49]. The energy for the local mode was 600 K, which is similar to the activation energy reported previously for the second contribution to semiquinone relaxation (Eq. 3.1). The full expression for a local mode is given by Eq. (3.3) [50].

$$\frac{1}{T_1^{\text{local}}} = C_{local}\frac{e^{\Delta_{loc}/T}}{(e^{\Delta_{loc}/T}-1)^2} \tag{3.3}$$

where Δ_{loc} is the energy of the local mode in Kelvin and C_{local} is determined experimentally. If $\Delta_{loc} >> T$, Eq. (3.3) can be approximated as in Eq. (3.4), which has the same temperature dependence as the second term in Eq. (3.1).

$$\frac{1}{T_1^{\text{local}}} \sim C_{local}e^{-\Delta_{loc}/T} \tag{3.4}$$

These results indicate that the two dominant contributions to spin-lattice relaxation at X-band for semiquinones tumbling rapidly in solution are spin rotation and a local mode with an energy of 500 to 600 K. The contributions from these two relaxation mechanisms are independent of resonance frequency.

Studies of the frequency dependence of spin-lattice relaxation for carbon-centered trityl radicals [51] and nitrogen-centered nitroxide radicals [21, 22, 52] have demonstrated the significance of additional relaxation mechanisms. These frequency-dependent processes modulate anisotropic interactions – *g* anisotropy (Eq. 3.5) [29, 53], hyperfine (A_i) anisotropy (Eq. (3.7) [29, 53, 54], dipolar coupling to solvent nuclei (Eq. 3.8) [51], or involve a thermally-activated process (Eq. 3.9) [22].

$$\frac{1}{T_1^g} = \frac{2}{5}\left(\frac{\mu_B \omega}{g\beta}\right)^2 \left\{ \frac{(\Delta g)^2}{3} + (\delta g)^2 \right\} J(\omega) \tag{3.5}$$

where $\Delta g = g_{zz} - 0.5(g_{xx}+g_{yy})$, $\delta g = 0.5(g_{xx} - g_{yy})$, μ_B is the electron Bohr magneton and $J(\omega)$ is the Bloembergen, Purcell, Pound (BPP) spectral density function (Eq. 3.6).

$$J(\omega) = \frac{\tau_R}{1+(\omega\tau_R)^2} \tag{3.6}$$

where τ_R is the tumbling correlation time and ω is the resonance frequency.

$$\frac{1}{T_1^A} = \frac{2}{9} I(I+1) \sum_i (A_i - \bar{A})^2 J(\omega) \tag{3.7}$$

where A_i is a component of the nitroxide nitrogen hyperfine coupling in angular frequency units, $\bar{A}$ is the average nitrogen hyperfine, and I is the nitrogen nuclear spin.

$$\frac{1}{T_1^{\text{solvent}}} = C_{solvent}\frac{\tau_{solvent}}{1+(\omega\tau_{solvent})^2} \tag{3.8}$$

where $\tau_{solvent}$ is the correlation time for motion of the solvent relative to the radical, and $C_{solvent}$ is a function of the dipolar interaction with solvent nuclei.

$$\frac{1}{T_1^{\text{therm}}} = C_{therm}\left(\frac{\omega}{\omega_{ref}}\right)\frac{\tau_{therm}}{1+(\omega\tau_{therm})^2} \tag{3.9}$$

where $\tau_{therm} = \tau_c^{\,0} \exp(E_a/RT)$, E_a is the activation energy, $\tau_c^{\,0}$ is the pre-exponential factor, C_{therm} is the coefficient for the contribution of the thermally-activated process, and ω_{ref} = 9.5 GHz. Variable temperature studies of semiquinone spin lattice relaxation did not find evidence of a thermally-activated process [26, 49] so this contribution was not included in the models used in this chapter.

To determine the extent to which frequency-dependent processes (Eq. 3.5, 3.7, 3.8) contribute to the relaxation of semiquinones in alcohol solvents at 293 K, the three radicals shown in Figure 3.1 were studied at frequencies between 250 MHz and 34 GHz.

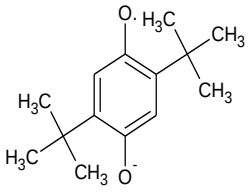

25DTBSQ

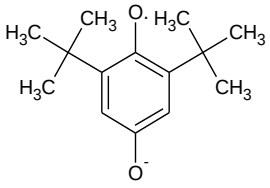

26DTBSQ

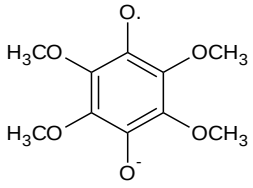

TMBSQ

Figure 3.1 Structures of the semiquinones studied.

3.2 Material and Methods

Semiquinone preparation

2,5-Di-*t*-butyl-1,4-benzosemiquinone (25DTBSQ) was prepared by mixing equal volumes of air-saturated ethanol solutions of 2,5-di-*t*-butyl hydroquinone (5 mM, Alfa Aesar, 98% purity) and KOH (5 mM) [55]. 2,6-Di-*t*-butyl-1,4-benzosemiquinone (26DTBSQ) was prepared from 2,6-di-*t*-butyl-1,4-benzoquinone (Sigma -Aldrich, 98% purity) using the same procedure. 2,3,5,6-tetramethoxy-1,4-benzosemiquinone (TMBSQ) was prepared by mixing a 2:1 volume ratio of 25 mM KOH and 5 mM tetraflouro-1,4-benzoquinone (Sigma-Aldrich, 97% purity) in methanol. Formation of the radicals was confirmed by X-band CW EPR [55]. Concentrations of the semiquinones were determined by comparison of the double integrals of the EPR spectra with double integrals of signals for 0.20 mM ^{15}N-CTPO (3-carbamoyl-2,2,5,5-tetramethyl-3-pyrroline-1-oxyl) in the same solvent. Concentrations were in the range of 0.2 to 0.5 mM. Air-saturated solutions stored at 4^{o}C for up to 30 days produced the semiquinone EPR signal after deoxygenation. 1,4-benzosemiquinones form adducts with, and react with, O_2 [56]. In deoxygenated solution the EPR signal decays within hours to days.

Oxygen Removal

Samples were purged with N_2 to remove O_2. Relaxation time measurements were repeated, with continued N_2 purging, until no further increase in relaxation time constant was observed. At Q-band the samples were in Teflon tubes with 0.30 mm ID and 0.66 mm OD that were placed inside a 1.6 mm OD quartz capillary tube that was open at both ends. The Bruker cryostat was purged with N_2 throughout the measurements. At

frequencies between 1 and 9 GHz samples were in 4 mm OD quartz tubes. The vapor space in the tube was initially purged vigorously with N_2, after which N_2 was gently bubbled into the solution through thin Teflon tubing. At X-band the resonator also was purged with N_2. At L-, S-, and X-band samples were purged continuously with N_2. At 600 MHz and 250 MHz 16 mm and 25 mm OD quartz tubes were used, respectively. The height of the solution in the tube was about 3 cm. To purge the large vapor space in these tubes the following protocol was developed: 15 min purging at the top of the tube, 15 min near the top, 15 min in the middle of the tube and 30 min gentle bubbling into the solution followed by constant gentle purging of the solution with N_2 during the relaxation time measurements.

Spectroscopy

CW spectra

CW spectra at X-band were obtained using a Bruker EMX EPR spectrometer with SHQ resonator, 10 KHz modulation frequency, 0.5 G modulation amplitude, 0.636 mW incident power. Spectra are shown in Figure 3.2. To observe the smaller hyperfine splitting from the tert-butyl and methoxy protons, smaller modulation amplitudes were used than for Figure 3.2 to obtain the spectra shown in Figure 3.3. 0.05 G modulation amplitude was used for 25DTBSQ (A) and 26DTBSQ (B) and 0.02G modulation amplitude was used for TMBSQ (C)

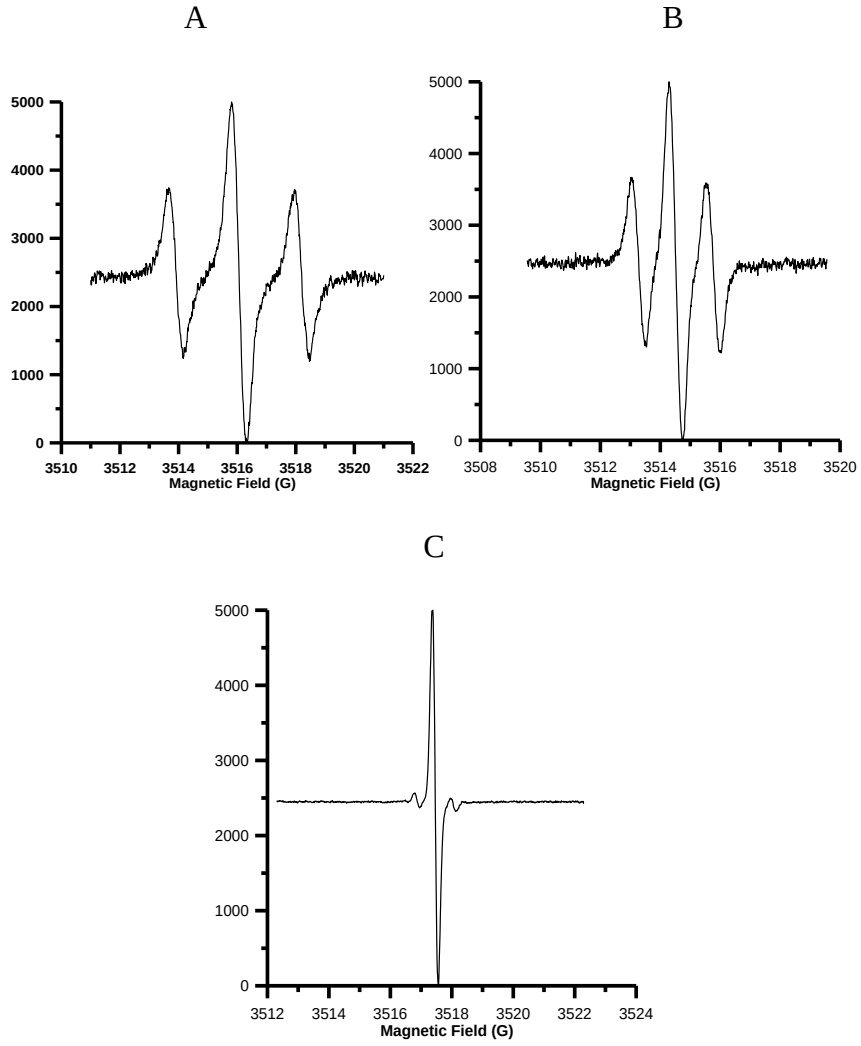

Figure 3.2 CW spectra of semiquinones obtained with 10 KHz modulation frequency, 0.636 mW incident power, 40.96 ms conversion time, 40.96 ms time constant, 1024 points, and 0.5 G modulation amplitude for 25DTBSQ (A), 26DTBSQ (B) and 0.05 G for TMBSQ (C).

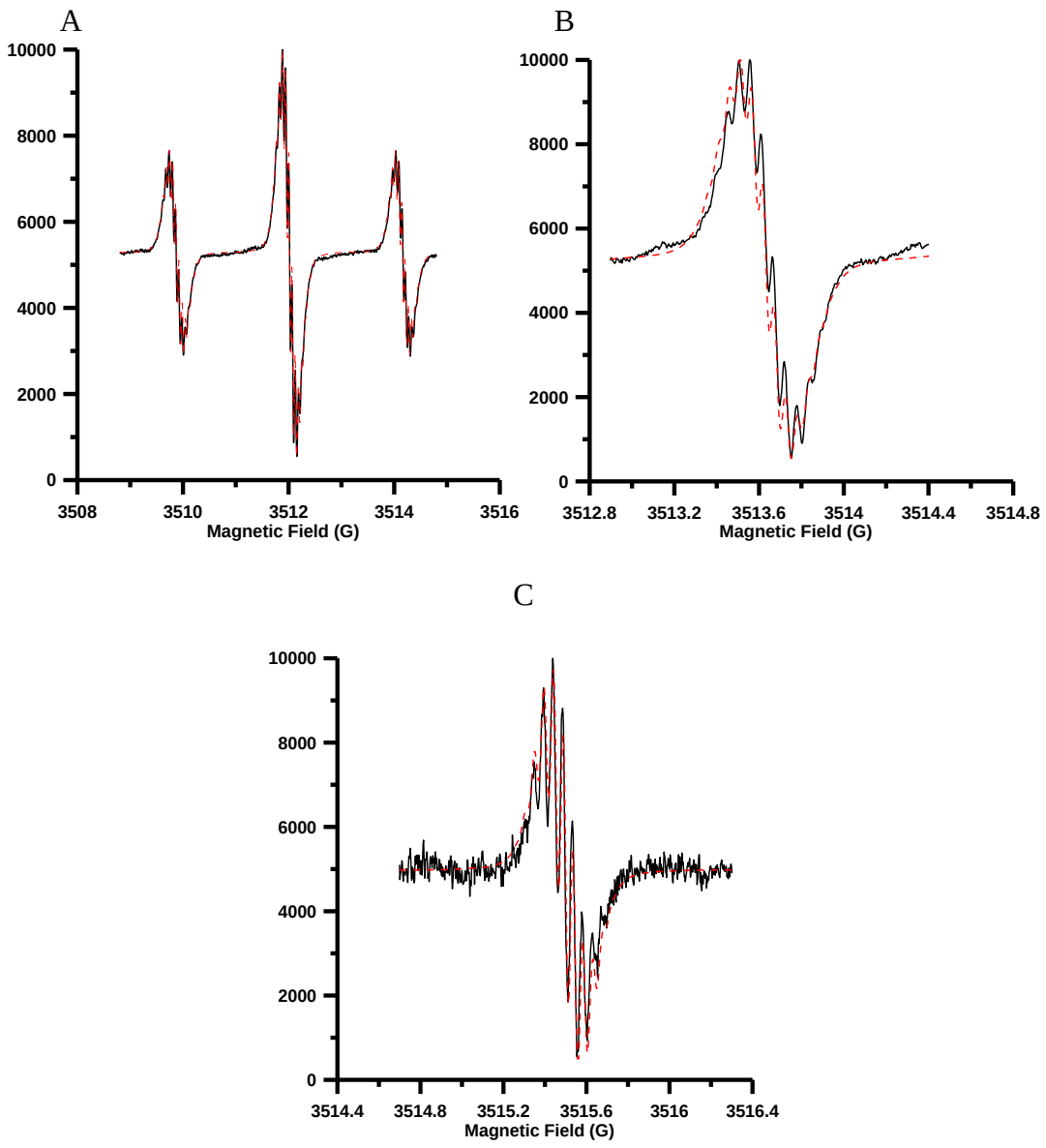

Figure 3.3 CW spectra of semiquinones obtained with 0.05 G modulation amplitude to observe the hyperfine splitting from t-butyl group protons for 25DTBSQ (A) and 26DTBSQ (B). (A, B) Conversion time was 40.96 ms, time constant was 40.96 ms, and 1024 points. (C) For TMBSQ 0.02G modulation amplitude was used, conversion time was 10.24 ms, time constant was 10.24 ms, 1024 points, 2 G sweep width to resolve the hyperfine from the 12 protons on the methoxy groups. The red dashed lines are the simulations of the spectra which used the following proton hyperfine splittings: 0.059 G (A), 0.052 G (B), and 0.046 G (C).

Stability

The stability of 25DTBSQ in ethanol was monitored for 25 days by taking a small sample from the solution that was kept refrigerated, placing it in 4 mm EPR tube, purging with N_2, and recording the EPR spectrum. The concentration of the semiquinone radical dropped quickly from 0.58 mM to 0.27 mM after 2 days, then stayed constant for about 25 days (Figure 3.4). 26DTBSQ and TMBSQ had similar stability. The concentration was determined by comparing the integrated intensity of the EPR signal with that for 0.2 mM ^{15}N-CTPO prepared in ethanol and spectra recorded under same conditions. The purging method enhanced the stability which is in contrast to flame sealing the tube which caused the EPR signal to decay in two hours.

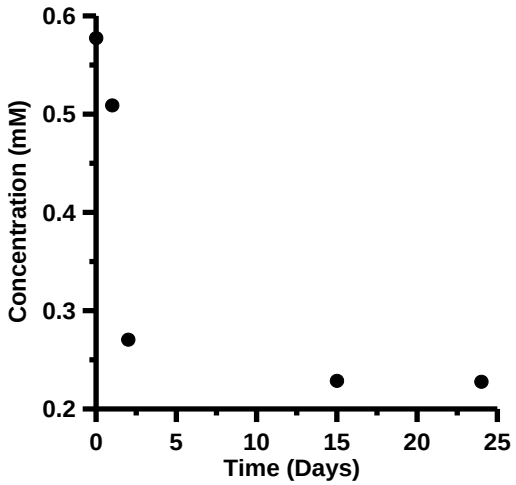

Figure 3.4 25DTBSQ stability monitored for 25 days.

Relaxation times measurements

Spin-lattice relaxation times, T_1, were measured by inversion recovery at 250 MHz [57], 600 MHz [22], L-band (1.0, 1.5 GHz) [58], S-band (2.57, 3.0 GHz) [58], and X-band (9.5 GHz) [24] on locally designed spectrometers. Q-band (34 GHz) measurements were performed on a Bruker E580 spectrometer. The experiments were performed at a resonator temperature of ~293 K. Multifit, a locally written program based on the algorithms of Provencher, was used to determine T_1 from the decay curves [59]. Single exponential fits were in good agreement with the data. Replicate measurements demonstrated that uncertainties were in the range of 5 to 15%, as shown Figures 3.5 – 3.7. At lower frequencies the signal-to-noise was poorer than at higher frequencies, which resulted in greater uncertainty in T_1.

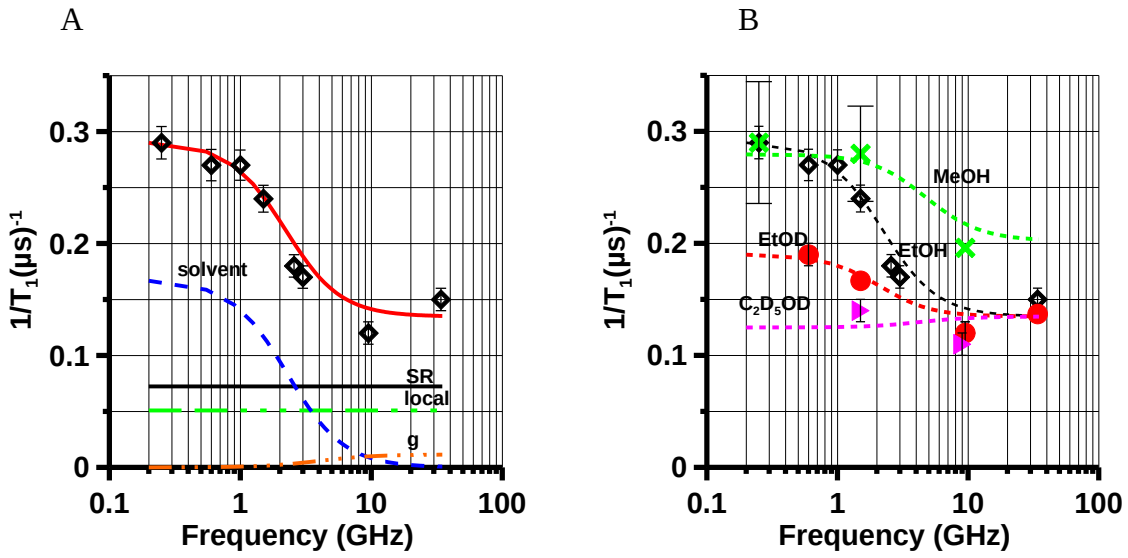

Figure 3.5 (A) Frequency dependence of $1/T_1$ (◊) for 25DTBSQ in ethanol at 293 K. The relaxation is modeled as the sum (—) of contributions from spin rotation (SR) (—) Eq. (3.2), a local mode (local) (— — - - -) Eq. (3.3), modulation of g-anisotropy (g) (— - - -) Eq. (3.5) and modulation of dipolar interactions with solvent nuclei (solvent) (- - -) Eq. (3.8). (B) Frequency dependence of $1/T_1$ in EtOH (◊), in MeOH (x), in monodeuterated ethanol (EtOD) (•) and in perdeuterated ethanol (C_2D_5OD) (▶). The dashed lines are the sums of the contributions to the spin lattice relaxation as described in the text, calculated with Eq. 3.2, 3.3, 3.5, and 3.8.

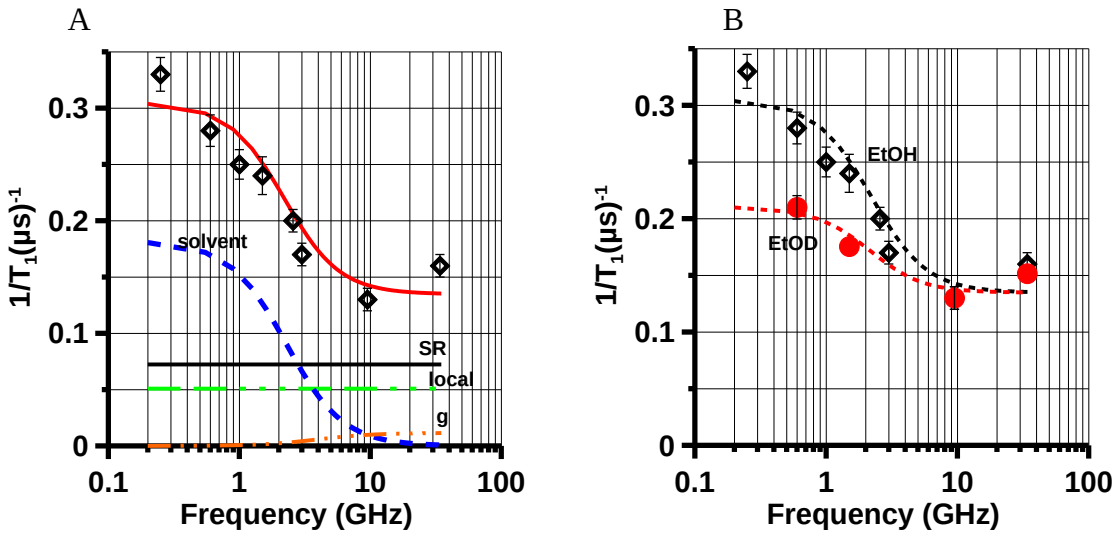

Figure 3.6 (A) Frequency dependence of $1/T_1$ (◊) for 26DTBSQ in ethanol at 293 K. The relaxation is modeled as the sum (—) of contributions from spin rotation (SR) (—) Eq. (3.2), a local mode (local) (— — - - -) Eq. (3.3), modulation of g-anisotropy (— - - -) Eq. (3.5), and modulation of dipolar interactions with solvent nuclei (solvent) (- - -) Eq. (3.8). (B) Frequency dependence of $1/T_1$ in EtOH (◊) and in monodeuterated ethanol (EtOD) (●). The dashed lines are the sums of the contributions to the spin lattice relaxation as described in the text and calculated with Eq. 3.2, 3.3, 3.5, and 3.8.

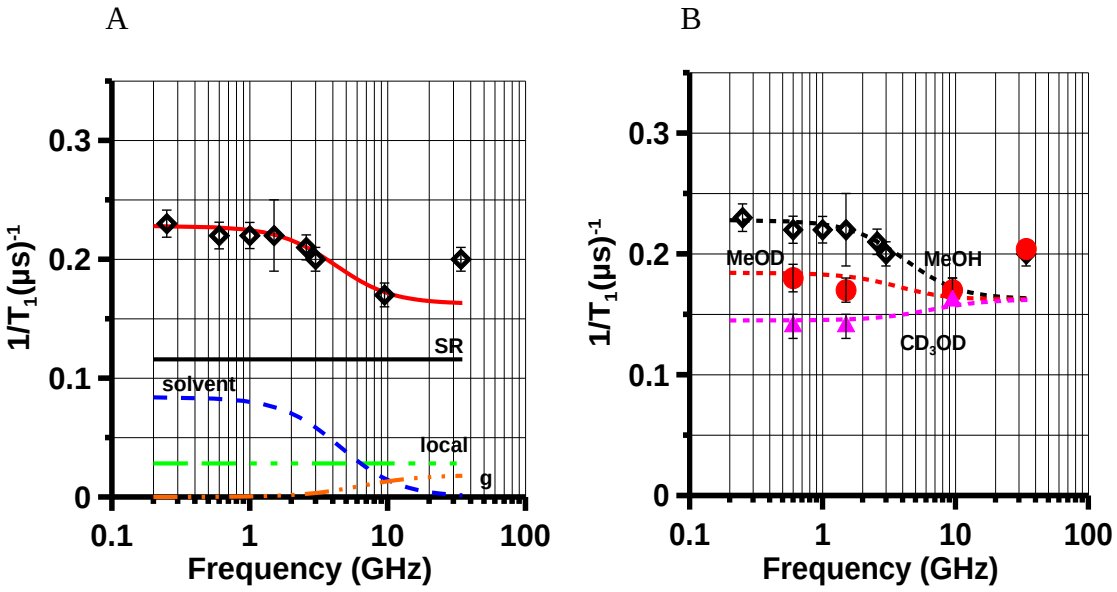

Figure 3.7 (A) Frequency dependence of $1/T_1$ (◊) for TMBSQ in methanol at 293 K. The relaxation is modeled as the sum (—) of contributions from spin rotation (SR) (—) Eq. (3.2), a local mode (local) (— — - - -) Eq. (3.3), modulation of g-anisotropy (— - - -) Eq. (3.5) and modulation of dipolar interactions with solvent nuclei (solvent) (- - -) Eq. (3.8). (B) Frequency dependence of $1/T_1$ in methanol (◊), in monodeuterated methanol (MeOD) (•), and in perdeuterated methanol (CD_3OD) (▲). The dashed lines are the sums of the contributions to the spin lattice relaxation as described in the text, calculated with Eq. 3.2, 3.3, 3.5, and 3.8.

3.3 Modeling the Frequency Dependence of $1/T_1$

Frequency-Independent Contributions to $1/T_1$

The two frequency-independent contributions to $1/T_1$ for molecules tumbling rapidly in fluid solution are spin rotation (Eq. 3.2) and the local mode (Eq. 3.3, 3,4). The contribution $1/T_1^{local}$ was calculated using Eq. (3.3) with Δ_{loc} = 500 K to be consistent with ΔE = 1 kcal/mole from the extensive early work on semiquinones [26]. In Ref. [26] the value of B (Eq. 3.1) for 25DTBSQ in ethanol or methanol was 0.29×10^6 s^{-1}. A value of Δ_{loc} = 500 K in Eq. (3.3) is not large enough to be fully in the limit of $\Delta_{loc} >> T$ at 293 K. To make the value of $1/T_1^{local}$ at 293 K calculated using Eq. (3.3) with Δ_{loc} = 500 K equal to that calculated with Eq. (3.1) and ΔE = 1 kcal/mole requires multiplication of B by about a factor of 0.7, which gives $C_{local} \sim 0.19 \times 10^6$ s^{-1}. In Ref. [49] the contribution from the local mode for 25DTBSQ in 1:4 glycerol:ethanol or 1:2 glycerol:ethanol was calculated with Δ_{loc} = 600 K and $C_{local} = 0.18 \times 10^6$ s^{-1} or 0.13×10^6 s^{-1}, respectively. To obtain the same magnitude of contribution at 293 K with Δ_{loc} = 500 K would require $C_{local} = 0.11 \times 10^6$ s^{-1} or 0.08×10^6 s^{-1} for the two solvent mixtures, respectively. Since there is a weak dependence of C_{local} on solvent and semiquinone, and there are uncertainties in parameters obtained in prior experiments, the values of C_{local} in the modeling of the frequency dependence of $1/T_1$ were constrained to be between 0.08×10^6 and 0.19×10^6 s^{-1}.

Calculation of $1/T_1^{SR}$ requires g values and τ_R. The g values for 25DTBSQ, 26DTBSQ, and TMBSQ in hydrogen-bonding solvents are g_x = 2.0065, g_y = 2.0052, and g_z = 2.0023 [49]. The viscosities at 298 K are 0.545 cP for MeOH and 1.08 cP for EtOH

[60]. Based on these viscosities, tumbling correlation times calculated using the Stokes-Einstein equation are 109 ps for 25DTBSQ or 26DTBSQ in EtOH and 57 ps for TMBSQ in MeOH at 293 K. In the early studies of semiquinone relaxation the spin rotation term was expressed as AT/η (Eq. 3.1), which can be related to the expression in Eq. (3.2) by using $\tau_R = c_{slip}\ V\ \eta/kT$ where V is the molecular volume and k is Boltzmann's constant [61, 62]. The adjustable parameter c_{slip} ranges from 0 to 1.0 depending on the extent of solute-solvent interaction. When molecular volumes were calculated assuming a density of 0.90, the values of A (Eq. 3.1) in ref. [26] correspond to c_{slip} ranging from 0.10 to 0.40 with an average of 0.24, including c_{slip} = 0.40 and 0.25 for 25DTBSQ in MeOH and EtOH, respectively, and c_{slip} = 0.36 for TMBSQ in MeOH. These values of c_{slip} are larger than those for nitroxides [22] which are 0.11 for tempone (which has a keto group) in water, 0.15 for mHCTPO (which has a carboxamide group) in water, and 0.21 for proxyl (which has a carboxy group) in water. The larger values of c_{slip} for the anionic semiquinones than for neutral nitroxides are consistent with the expectation of stronger interaction of the semiquinones with the H-bonding polar solvents. Values of c_{slip} in water:glycerol mixtures for trityl radicals with three carboxy groups are about 0.65 [51]. Since the molar masses of the trityls are in the range of 975 to 1695 [51] and the Stokes-Einstein model results in c_{slip} closer to 1 for larger molecules, the values of c_{slip} for semiquinones with molar masses about 220 are expected to be smaller than for the trityls. In modeling the frequency dependence of $1/T_1$ the values of c_{slip} were constrained to be between 0.24 and 0.50. It was assumed that c_{slip} was similar in ethanol and methanol, unaffected by solvent deuteration, and similar for 25DTBSQ and 26DTBSQ. The

resulting values of c_{slip} were 0.37 for 25DTBSQ and 26DTBSQ and 0.44 for TMBSQ (Table 3.1). The higher value for TMBSQ may reflect additional solvent interaction with the methoxy oxygens.

Frequency-Dependent Contributions to $1/T_1$

The contribution from modulation of *g* anisotropy (Eq. 3.5) is calculated from the known *g* values and the value of τ_R that was determined by analysis of the contributions from frequency-independent terms at X-band.

Eq. (3.7) the contribution from modulation of anisotropic nuclear hyperfine interaction, was derived for a single nuclear spin. That contribution is proportional to the square of the hyperfine anisotropy. Analogous equations have not been derived for multiple hyperfine interactions. The anisotropic hyperfine couplings to the two ring protons of 25DTBSQ and 26DTBSQ are (1.92, 2.14, 2.35 G) and (0.92, 1.28, 1.44 G), respectively [49]. If it is assumed that the contributions from multiple protons are additive, the estimated contributions from modulation of hyperfine anisotropy for the two ring protons are about two orders of magnitude smaller than the observed frequency dependence of $1/T_1$ Figures 3.5-3.7. Although the assumption of additivity is over-simplified, more sophisticated analysis are unlikely to dramatically change the magnitude of the contribution, so modulation of the anisotropic ring proton hyperfine coupling was omitted from the analysis.

The parameters $C_{solvent}$ and $\tau_{solvent}$ were adjusted to match the experimental data. The inflection point in the plot of $1/(T_1^{solvent})$ vs. frequency is strongly dependent on

$\tau_{solvent}$ so those values are tightly constrained. The value of $C_{solvent}$ was adjusted to model the magnitude of the frequency-dependent contribution at low frequency.

3.4 Results and Discussion

The spin lattice relaxation rates for the semiquinones were studied at 293 K at up to 8 frequencies between 250 MHz and 34 GHz. As reported previously [26] there was negligible concentration dependence of T_1 for concentrations of the order of 1 mM. This lack of concentration dependence has been attributed to the solvent cage around the radicals [26]. The negative charge on the anionic semiquinones also may decrease collision probabilities. In a comparable concentration range significant concentration dependence has been observed for nitroxide radicals [20] .

For 25DTBSQ in EtOH or MeOH (Figure. 3.5), 26DTBSQ in EtOH (Figure. 3.6), and TMBSQ in MeOH (Figure 3.7) the spin lattice relaxation rates were about a factor of two faster at lower frequencies than at 9 GHz. The relaxation was modeled as the sum of contributions from two frequency-independent process, (spin rotation (Eq. 3.2) and a local mode (Eq. 3.3), and two frequency-dependent processes (modulation of dipolar interaction with solvent nuclei (Eq. 3.8) and a smaller contribution from modulation of g-anisotropy (Eq. 3.5), Table 3.1. Spin-lattice relaxation at X-band is dominated by the frequency-independent processes. Decreasing τ_R increases the contribution from spin rotation which can be compensated by increasing the coefficient C_{local}. The range of acceptable values of τ_R is limited by the range of C_{local} found in prior variable temperature experiments [26, 49]. At 295 K the viscosity of MeOH (0.545 cP) is about half that of EtOH (1.08 cP) so τ_R decreases by about a factor of 2 when the solvent is

changed from EtOH (Figure 3.5A) to MeOH (Figure 3.5B). Comparison of relaxation rates for 25DTBSQ in EtOH and MeOH permitted separation of the tumbling-dependent spin-rotation contribution from the tumbling-independent local mode contribution. This set of constraints permitted definition of the values of τ_R.

The modulation of *g* anisotropy by molecular tumbling makes a relatively small contribution to $1/T_1$ and is significant for the semiquinones only at Q-band. For each of the semiquinones the relaxation rates at Q-band were faster than predicted by modeling with Eq. (3.2, 3.3, 3.5, and 3.8). It is therefore proposed that an additional process contributes at higher frequencies, which will require further study. Analogous observations have been made for nitroxides [22].

The dominant frequency-dependent contribution to $1/T_1$ was decreased by deuteration of the solvent (Figures 3.5 – 3.7). For all three semiquinones replacement of solvent OH by OD decreased the contribution from the frequency-dependent contribution by about a factor of two (Table 3.1). Complete solvent deuteration eliminated this contribution, which demonstrated domination of the frequency dependent contribution to relaxation by interaction with solvent nuclei. The contributions calculated from Eq. (3.8) are strongly dependent on the value of $\tau_{solvent}$. The simulations required $\tau_{solvent}$ about twice as long as τ_R. The uncertainties for $\tau_{solvent}$ are about ±10% and the uncertainties for τ_R are about 25% so the difference of about a factor of 2 is much larger than the uncertainties in the correlation times. The observation of $\tau_{solvent} > \tau_R$ indicates that the dynamic process that modulates the interaction between the unpaired electron and the solvent nuclei is not molecular tumbling. Water and alcohols are strongly hydrogen

bonded to semiquinones [63-65]. The observations that (i) the contribution from Eq. (3.8) decreased by about a factor of 2 when OH was replaced by OD (Figures 3.5 – 3.7), (ii) the frequency dependent contribution to relaxation was eliminated by solvent perdeuteration, and (iii) values of $\tau_{solvent}$ differ from τ_R, are consistent with assignment of fluctuations in hydrogen bonding as the process that drives $\tau_{solvent}$.

Relaxation rates for semiquinones compared with trityl-CH_3 and mHCTPO in Table 3.2. Relaxation rates for trityl at X-band are dominated by a local mode. Semiquinone radicals have higher g-values than trityls, so the dominant contributions for semiquinones at X-band are the spin rotation in addition tothe local mode. Nitroxides have large anisotropy nitrogen hyperfine couplings so the dominant contributions at X-band are spin rotation and modulation of A-anisotropy.

Relaxation rates, $1/T_1$, for nitroxide [21, 22, 66] and trityl radicals [51] also have been found to be larger at 250 MHz to 1 GHz than at 9 GHz (Table 3.2). For trityls the enhanced relaxation rates at lower frequencies are attributed to modulation of electron-proton dipolar coupling by tumbling. For semiquinones it is proposed that the electron-proton dipolar interactions are modulated by fluctuations in the hydrogen bonding between the solvent and the semiquinone oxygens. However for nitroxides the dominant contribution to enhanced relaxation rates at lower frequencies is modulation of anisotropic nitrogen hyperfine couplings. This process is not significant for trityls or semiquinones because these molecules do not have large anisotropic hyperfine couplings. The common theme for these relaxation enhancements at lower frequencies is that the rates of dynamic processes become comparable to the resonance frequency, ie $\omega \sim 1/\tau$.

Table 3.1 Contributions to Spin-Lattice Relaxation of Semiquinones at 293 K in Fluid Solution

Semiquinone	Solvent	τ_R (ps)[a], (c_{slip})	Δ_{loc} (K)[b]	C_{loc} (s^{-1})	$\tau_{solvent}$ (ps)	$C_{solvent}$ (s^{-1})
25DTBSQ	EtOH	40 (0.37)	500	$0.18x10^6$	70	$2.4x10^{15}$
	EtOD	40 (0.37)	500	$0.18x10^6$	70	$1.0x10^{15}$
	C_2D_5OD	40 (0.37)	500	$0.18x10^6$	70	~0
	MeOH	20 (0.36)	500	$0.18x10^6$	35	$2.4x10^{15}$
26DTBSQ	EtOH	40 (0.37)	500	$0.18x10^6$	70	$2.6x10^{15}$
	EtOD	40 (0.37)	500	$0.18x10^6$	70	$1.2x10^{15}$
TMBSQ	MeOH	25 (0.44)	500	$0.10x10^6$	35	$2.4x10^{15}$
	MeOD	25 (0.44)	500	$0.10x10^6$	35	$1.2x10^{15}$
	CD_3OD	25 (0.44)	500	$0.10x10^6$	35	~0

[a] g = 2.0065, 2.0052, 2.0023 [49]

[b] Fixed at the value obtained by variable temperature studies [26].

Table 3.2 comparison between trityl-CH_3, 25DTBSQ and mHCTPO at X-band and **V**HF

Radical	Low frequency (VHF)		X-band		Ref.
	T_1(μs)	Contribution	T_1(μs)	Contribution	
trityl-CH_3	8	Electron-proton dipolar	16	Local mode	[51]
25DTBSQ	3	Solvent dynamics	8	Local mode + spin rotation	This work
mHCTPO	0.5	N-hyperfine	1	Spin rotation + N-hyperfine	[22]

Typical values at 295 K in water

Chapter Four: Electron Spin Relaxation Times of pH-sensitive Amino Substituted Trityl Radicals

4.1 Introduction

Localized measurement of pO_2 and pH is crucial to understand normal and diseased states [67]. It would be particularly helpful to have probes that can monitor both properties. Water-soluble triarylmethyl (TAM) radicals have been shown to be useful probes for EPR oximetry [68, 69]. Synthetic methods have been developed for larger scale preparations of TAMs to facilitate in vivo applications [70]. The narrow EPR signals and long T_1 and T_2 values of carboxy-substituted TAM radicals make them sensitive probes of local oxygen concentration [71-73]. Carboxylic groups on TAMs make the EPR signal sensitive to pH [67]. However, the pK_a of carboxylic groups is too low to be appropriate for monitoring pH in the physiological range. Replacement of one of the carboxylic groups by an amino group to form $aTAM_4$ or its selectively deuterated analog $aTAM_5$ (Figure 4.1) has been shown to result in probes with spectra that are oxygen responsive and pH sensitive in the range of pH = 6 to 8 [74]. The relatively long electron spin relaxation times for carboxy-substituted TAMs trityl-CH_3 and Oxo63 (Figure 4.1) [75] are advantageous for pulsed oximetry [76-79]. To assess the potential utility of aTAMs for pulsed oximetry and pH measurement, the pH dependence of the relaxation times for $aTAM_4$ and $aTAM_5$ were studied at X-band (9.4 GHz). T_1 was

measured by saturation recovery and inversion recovery and T_2 was measured by pulsed electron spin echo decay. To demonstrate the feasibility of using these probes for EPR imaging, rapid scan images at 250 MHz were obtained for a phantom consisting of tubes containing $aTAM_4$ at pH 6.5 and 7.1 (Chapter five).

4.2. Materials and Methods

Samples

Preparation of $aTAM_4$ and $aTAM_5$ was performed at The Ohio State University by Dr. Ilirian Dhimitruka using literature procedures [74]. Weighed samples of $aTAM_4$ were dissolved in absolute ethanol and diluted with potassium phosphate (1.0 M) or tris (1.0 or 0.5 M) buffer in a 20:80 percent ratio (ethanol:buffer) to yield a final radical concentration of 0.1 mM. Samples of TAM_5 were prepared analogously using 0.5 M tris buffer. For X-band experiments solutions in thin-wall 0.97 mm i.d. Teflon tubing were placed inside 4 mm o.d. quartz tubes. For the continuous wave (CW) and pulsed EPR experiments oxygen was removed by passing N_2 gas over the sample using a thin Teflon tube inserted parallel to the Teflon tube that contained the sample.

X-band Spectroscopy

CW spectra were obtained at 295 K on a Bruker EMX spectrometer with an SHQ resonator. Microwave power (B_1) was selected to be in the regime where signal intensity increases linearly with the square root of power. CW spectra were simulated with locally written programs and with WINSIM [74]. The nitrogen and proton hyperfine splittings obtained by the simulations shown in Tables 4.1 and 4.2 are in good agreement with the

literature values [74]. Inclusion of 7% of trityl-CH_3 (Figure 4.1) was required to match the relative intensities of the peaks in the spectra of $aTAM_4$ (Figure 4.2).

Measurements of electron spin relaxation times at room temperature were performed on a locally-designed and built pulsed spectrometer [24] equipped with a Bruker ER4118-X-MS5 split ring resonator and a 1 KW microwave amplifier. The resonator was over-coupled to Q ~ 100. Multifit, a locally written program based on the algorithms of Provencher [59], was used to determine T_1 or T_2 from the decay curves. T_2 was determined by two-pulse spin echo. For a sample of $aTAM_4$ in tris buffer, variation of the length of the 90^o pulse from 40 ns to 160 ns caused no discernible change in T_2 (Table 4.3, 4.4). The values reported in Tables 4.5 to 4.7 were obtained with a 90^o pulse length of 40 ns, which corresponds to a B_1 of 2.2 G. Longer pulses are more selective but result in poorer signal-to-noise. T_1 was measured by inversion recovery. For $aTAM_4$ in tris buffer the value of T_1 decreased as the length of the 90^o pulse was increased from 40 to 320 ns, which is attributed to spectral diffusion as shown in Table 4.8- 4.9. Data reported in Tables 4.5 – 4.7 were obtained with a 90^o pulse length of 40 ns. T_1 also was measured by long-pulse saturation recovery on a locally-built spectrometer [23] equipped with a Varian E231 resonator. The pump and observe powers were 12 dB and 18 dB, respectively. Recovery curves obtained with a 50 μs saturating pulse could be fit well with a single exponential. Values of T_1 obtained by saturation recovery (Table 4.10) were systematically shorter by about 1 μs than values obtained by inversion recovery with a 90^o pulse length of 40 ns (Table 4.5). This difference is comparable to the estimated uncertainties in the values. The poorer signal-

to-noise for the saturation recovery experiments may contribute to systematically shorter values of T_1 (Table 4.10).

4.3. Result and Discussion

CW spectra of $aTAM_4$ at pH 6.5, 7.6, and 8.5 (Figure 4.2) and of $aTAM_5$ at pH 6.5, 8.2, and 9 (Figure 4.3) are pH dependent and in good agreement with spectra reported previously [74]. Protonation of the amino group of $aTAM_4$ increases the coupling to the amino nitrogen from 0.69 G to 1.01 G and decreases the coupling to one of the protons on the CH_2 group from 2.04 to 1.05 G (Figure 4.1). The sample of $aTAM_4$ contained about 7% of the parent compound trityl-CH_3 which puts a sharp signal line in the center of the spectrum (Figure 4.2). This signal provided an internal comparison between the properties of $aTAM_4$ and of trityl-CH_3. Because of the changes in the hyperfine coupling constants the contributions from the protonated and deprotonated species are well resolved in the high-field and low-field regions of the spectrum (Figure 4.2). In $aTAM_5$ the two protons of the methylene group that link the amino substituent to the aryl ring are deuterated, which reduces the corresponding hyperfine coupling constants to the methylene nuclei by about a factor of 6 [74]. The spectral width is therefore reduced, but more lines are resolved in the spectrum so deuteration does not simplify the spectrum.

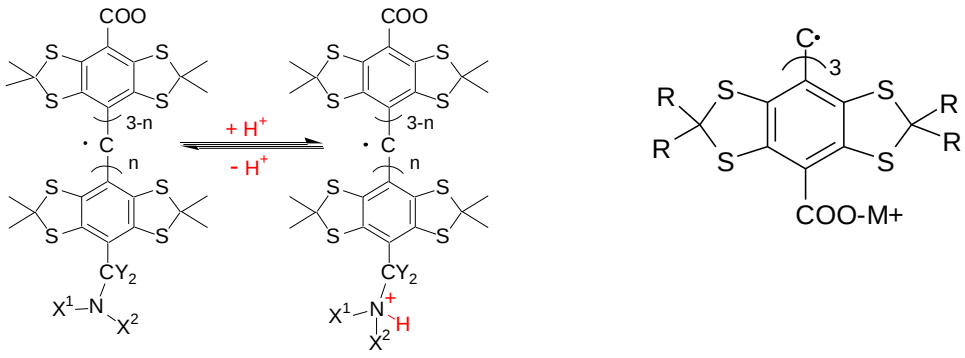

	n	X^1	X^2	Y
$aTAM_4$	1	Et	Et	H
$aTAM_5$	1	Et	Et	D

	R
Trityl-CH_3	CH_3
Oxo63	CH_2CH_2OH

Figure 4.1 Structures of trityl TAM and aTAM radicals [51, 74]

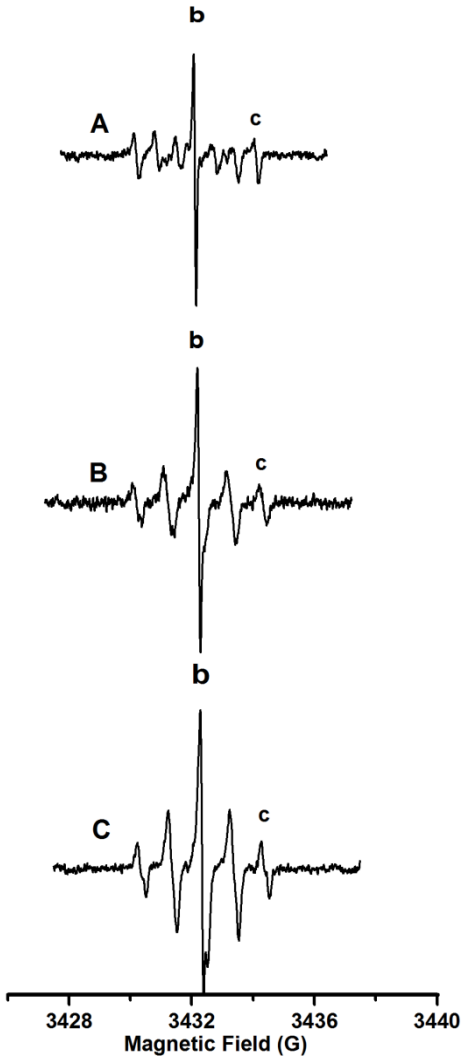

Figure 4.2 X-band CW spectra of aTAM$_4$ obtained with 10 kHz modulation frequency, 0.05 G modulation amplitude, 10 G sweep with 2048 points, 20.48 ms time constant and conversion time, 41 s sweep time, 0.318 mW incident power. (A) at pH 8.5, (B) at pH 7.5,and (C) at pH 6.5. The line marked with 'b' has a contribution from about 7% of trityl-CH_3.

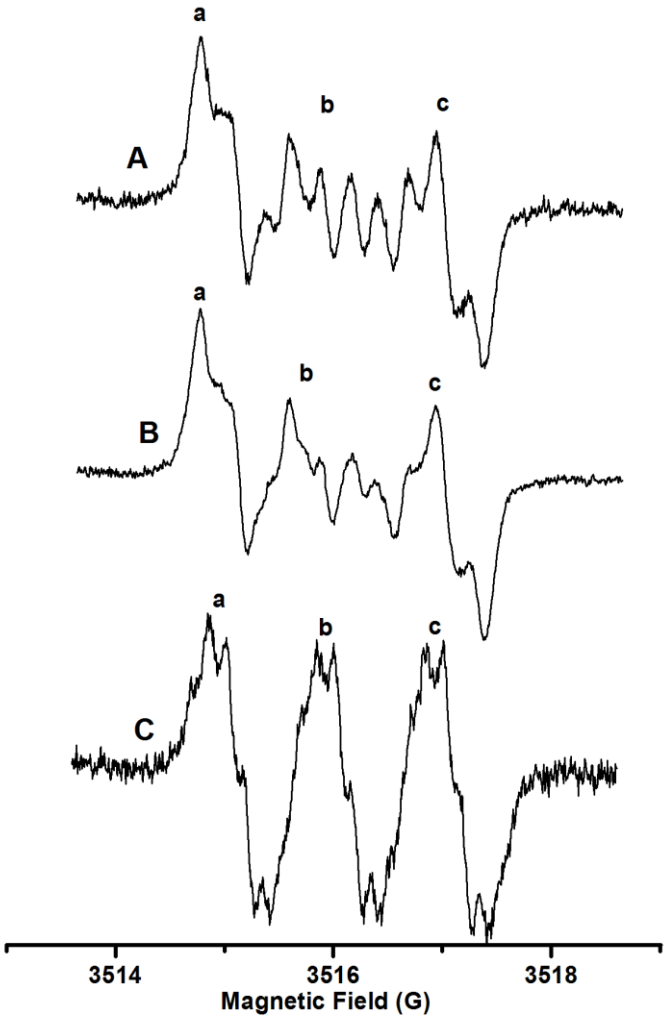

Figure 4.3 X-band CW spectra of $aTAM_5$ obtained with 30 kHz modulation frequency, 0.1 G modulation amplitude, 5 G sweep with 1024 points 163.84 ms time constant and conversion time, sweep time 167.77 s, 0.318 mW power. (A) at pH 9.0, (B) at pH 8.2, and (C) at pH 6.4.

Table 4.1 Hyperfine splitting constants (G) for $aTAM_4$

	Protonated	Deprotonated (high pH)
N	1.01	0.69
1 H	0.97	0.95
1 H	1.05	2.04
1H	0.15	

Table 4.2 Hyperfine splitting constants (G) for $aTAM_5$

	Protonated	Deprotonated (high pH)
N	0.99	0.67
1 D	0.14	0.150
1 D	0.17	0.300
1H	0.15	

Table 4.3 T_2 values in (μs) for the center field line of 0.1mM $aTAM_4$ obtained by echo decay at X-band

	CF		
pH	40-80	160-320	320-640
phosphate			
6.8	3.3±0.5	3.5±0.3	3.4±0.6
7.67	3.9±0.3	4.5±0.1	4.6
Tris			
6.5	2.9±0.1	3.2±0.2	3.3±0.1
7.59	3.7±0.1	3.8±0.3	4.6
8.49	3.6±0.2	3.8±0.1	4.0±0.1

Table 4.4 T_2 values in (μs) for the high field line of 0.1mM $aTAM_4$ obtained by echo decay at X-band

	HF		
pH	40-80	160-320	320-640
Phosphate			
6.8	0.7±0.1		
7.7	0.6±0.1		
Tris			
6.5	3	3.2±0.3	
7.6	1.3±0.1	1.3±0.1	
8.5	0.8±0.3	0.7	

Table 4.5 pH dependence of T_1 and T_2 for $aTAM_4$ at X-band[+]

Line (Fig. 2)	pH	T_1 (μs)	T_2 (μs) in H_2O	T_2 (μs) in D_2O
b	6.5	18±0.3	2.9±0.1	
b	7.6	18±0.6	3.7±0.1	
b	8.5	18±0.5	3.6±0.2	3.5±0.1
c	6.5	15±0.6	3.2±0.3	
c	7.6	17±0.2	1.3±0.1	
c	8.5	17±0.8	0.76±0.1	2.7±0.1

[+]Values in tris buffer obtained with 90° pulse lengths of 40 ns. The signal designed as line 'b' is an overlap of contributions from $aTAM_4$ and about 7% impurity of trityl-CH_3.

Table 4.6 pH dependence of T_1 and T_2 values for TAM_5 at X-band[+]

Line (Fig. 3)	pH	T_1 (μs) in H_2O	T_1 (μs) in D_2O	T_2(μs) in H_2O	T_2 (μs) in D_2O
a	6.5	20±0.1		3.6	
a	8.2	20±0.7	20±0.3	1.5±0.1	3.2±0.1
a	9			1.5±0.1	
b	6.5	20±0.7		3.7±0.1	
b	8.2	21±0.4	21±0.1	1.5±0.1	3.1±0.2
b	9	21 ±0.1		1.5±0.1	
c	6.5	20±0.4		3.6	
c	8.2	20±1.0	20±0.3	1.5±0.1	3.1±0.1
c	9			1.5±0.1	

[+]Values in tris buffer obtained with 90° pulse lengths of 40 ns.

Table 4.7 Comparison of T_1 and T_2 for Trityls at X-band

Compound	T_1 (μs)	T_2 (μs)
Trityl-CH_3 [51]	16	9.1
Oxo63 [51]	15	6.4
$aTAM_4$ (line b)	18	2.9 to 3.7
$aTAM_4$ (line c)	15 to 17	0.76 to 3.2
$aTAM_5$ (line a)	20	1.5 to 3.6
$aTAM_5$ (line b)	20	1.5 to 3.7
$aTAM_5$ (line c)	20	1.5 to 3.6

Table 4.8 T_1 values in (μs) for the center field line of 0.1mM $aTAM_4$ obtained by inversion recovery at X-band

	CF			
pH	40-20-40	80-40-80	320-160-320	640-320-640
Phosphate				
6.8		17±0.1	13	12
7.67	18	17±0.4	13±0.1	12
Tris				
6.5	19	18±0.3	14±0.2	13±0.8
7.59		18±0.6	14±0.9	12
8.49	19	18±0.5	13±0.1	13±0.1

Table 4.9 T_1 values in (μs) for the high field line of 0.1mM $aTAM_4$ obtained by inversion recovery at X-band

	HF			
pH	40-20-40	80-40-80	320-160-320	640-320-640
phosphate 6.8				
7.7	16	14		
Tris 6.5		15	13	13
7.6		17	13	
8.5		17		

Table 4.10 T_1 values in (μs) for the center field line of 0.1 mM $aTAM_4$ obtained by saturation recovery at X-band

pH	CF
Phosphate 6.8	17±0.9
7.7	17±1.1
Tris 6.5	17±0.6
7.6	17±0.9
8.5	18±0.9

The values of T_1 for $aTAM_4$ exhibit little dependence on pH or position in the spectrum. Pulsed imaging of T_1 for Oxo63 is a powerful method for in vivo oximetry [79]. The pH invariance of T_1 for TAMs suggests that oxygen concentration can be measured independent of pH using T_1. T_2 for $aTAM_4$ and $aTAM_5$ are strongly dependent

on pH, varying between 0.76 and 3.7 μs Table 4.5-4.7. Values of T_2 are consistently shorter for the deprotonated form than for the protonated form. When the radicals were dissolved in D_2O instead of H_2O, the values of T_2 for the deprotonated form became similar to that for the protonated form. Since the magnetic moment of a deuteron is 1/6 that of a proton, the increase in T_2 in D_2O indicates that water dynamics that modulates electron coupling to the H(D) contribute to the decrease in T_2 for the deprotonated form of the radical. In a prior study [74] the lineshapes of CW spectra of a deoxygenated solution of deprotonated $aTAM_4$ found that the Lorentzian component had a peak-to-peak linewidth of 96 mG, which is larger than the 87 mG calculated from T_2 Table 4.11.

Spin packet shown in the Tables 4.3-4.4 were calculated using Eq. (1.6)

Table 4.11 Spin packet ΔB_{sp} for $aTAM_4$ calculated from T_2[#]

pH	ΔB_{sp}
	b(mG)
6.5	23
7.6	18
8.5	18
	c(mG)
6.5	21
7.6	50
8.5	87

[#]b and c are the lines as shown on the spectra in Figure 4.2

Table 4.12 Spin packet ΔB_{sp} for $aTAM_5$ calculated from T_2[#]

pH	ΔB_{sp}
	a(mG)
6.5	18
8.2	44
9	44
	b(mG)
6.5	18
8.2	44
9	44
	c(mG)
6.5	18
8.2	44
9	44

[#] a, b, and c are the lines as shown in Figure 4.3

Values of T_1 for $aTAM_4$ and $aTAM_5$ (Table 4.5) are similar to values reported for trityl-CH_3 and Oxo63 [51]. This similarity is consistent with the assignment that the dominant contribution to T_1 for TAM radicals in solution at ambient temperature is a local mode (see semiquinone chapter) [51]. Replacement of a substituent on one of the aryl rings does little to change the local mode, which presumably is centered in the hydrocarbon and sulfur core of the radical. Values of T_2 vary substantially as a function of pH and structure of the substituents, which presumably reflects a range of dynamic processes occurring in solution.

4.4 Conclusions

T_1 for $aTAM_4$ and $aTAM_5$ are similar to each other, approximately independent of pH, and similar to trityl-CH_3 and Oxo63. Insensitivity of T_1 to changes in substituents is

consistent with the assignment of the dominant contribution to spin lattice relaxation as a local mode that involves primarily atoms in the carbon and sulfur core. Values of T_2 vary substantially with pH and the nature of the aryl group substituent, reflecting a range of dynamic processes. The narrow spectral widths for the amino-substituted triaryl methyl radicals facilitate spectral-spatial EPR imaging, which was demonstrated with a phantom that will be described in Chapter five.

Chapter Five: EPR Imaging

5.1 Introduction

EPR imaging at low frequency is an important in vivo technique for monitoring changes in healthy and diseased states. Selection of the appropriate EPR probe allows the experimenter to obtain information about the environment of the imaged probe and its spatial distribution. Because native paramagnetic species exist at low concentrations in living systems, exogenous paramagnetic species are needed for in vivo EPR [80]. Optimizing EPR imaging probes and EPR imaging methods are the focus of multiple EPR laboratories. [19, 81, 82]

This chapter describes three EPR imaging applications that were performed during this dissertation project in the Eaton lab. (i) The signal-to-noise advantage of rapid scan vs. CW EPR was demonstrated for a phantom constructed from two aqueous solutions of the spin probe, ^{15}N-PDT. The solution in one tube was equilibrated with air and the solution in the other tube had been deoxygenated. Linewidths were determined from 2D spectral-spatial images. (ii) To demonstrate the ability to measure local pH EPR imaging was performed for a phantom constructed from aqueous solutions of the pH-sensitive trityl radical ($aTAM_4$) at two different pH values. (iii) Experiments were performed to test a new algorithm developed by Dr. Mark Tseitlin to image a full

spectrum without the restrictions that hamper the traditional filtered back projections (FBP) method.

5.2 Comparison between CW and Rapid Scan Methods for EPR Imaging of ^{15}N-PDT Nitroxide on the VHF (250 MHz) Spectrometer.

Extensive experiments at X-band (9.5 GHz) have demonstrated that the signal-to-noise in rapid scan EPR spectra is substantially higher than for conventional CW spectroscopy [11-14]. Rapid scan is predicted to have even greater advantages over CW for imaging because the absorption spectrum is acquired instead of the first derivative [83]. To test this hypothesis images reconstructed from EPR data acquired by the rapid scan method were compared with images reconstructed from data acquired using CW EPR to monitor the effect of dioxygen on the linewidth of ^{15}N-PDT.

The phantom for imaging was constructed from two quartz tubes containing 0.2 mM ^{15}N-PDT in H_2O. A 6 mm tube contained degassed 0.2 mM ^{15}N-PDT and a 10 mm tube contained the same sample equilibrated with air. The two tubes were placed in a 16 mm cross-loop resonator [84]. Spectra and projections for images were obtained at an operating frequency of 258 MHz on a spectrometer that includes a modified Bruker E540 console and gradient coils and a resonator similar to the one described in [84]. 2D spectral-spatial images were reconstructed by filtered backprojection from 18 projections at equally spaced angles. The triangular rapid scans were generated with a linear driver [85]. Rapid scan imaging was performed using a Prodel program.

A CW spectrum was obtained with 5 KHz modulation frequency, 4.7 G sweep width, time constant 40.96 ms, conversion time 2.56 ms, 1024 points, 0.1 G modulation amplitude, and 14 dB power attenuation. Three scans were averaged to give a total of 8 s data acquisition time per projection. The low field line of the ^{15}N-PDT spectrum is shown in Figure 5.1. The spectrum is the superposition of the narrow line for the deoxygenated sample and the broader line for the oxygen-equilibrated sample. A rapid scan spectrum was collected with 8.6 KHz scan frequency 4.7 G scan width, averaged 65536 for a period total of 8 Sec, and 8db power attenuation with the same resonator tuning as for CW. The low field line of the ^{15}N-PDT spectrum is shown in Figure 5.2. In the rapid scan experiments data are acquired in quadrature for both up-field and down field scans. All of this information is combined to produce the final spectrum. Even with just the raw data it is evident that in a similar amount of data acquisition time the signal-to-noise is much higher for the rapid scan experiment than the CW experiment.

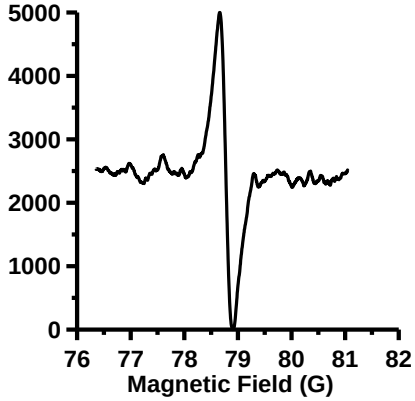

Figure 5.1 CW spectrum for two tubes containing 0.2 mM ^{15}N-PDT in H_2O, recorded at 250 MHz with 5 KHz modulation frequency, 4.7 G sweep width, time constant 40.96 ms, conversion time 2.56 ms, 1024 points, 0.1 G modulation amplitude and 14 dB power attenuation. Three of the 2.6 s sweeps were averaged for a total of 8 s acquisition time per projection

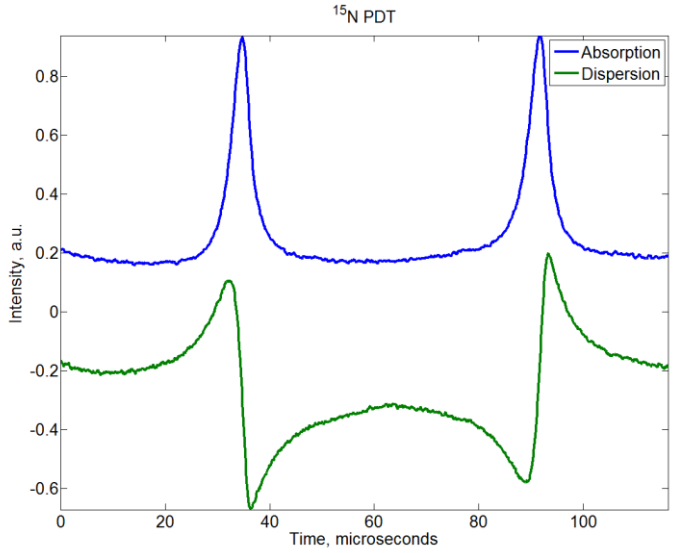

Figure 5.2 Rapid scan spectra of the same two tubes of 0.2 mM ^{15}N-PDT in H_2O as for Figure 5.1, recorded at 250 MHz with 8.6 KHz scan frequency, 4.7 G scan width, 8 db power attenuation, averaged 65536 times for an acquisition time of 8 s per period.

Projections for rapid scan images were acquired with 8.6 kHz scan frequency, 8 dB power attenuation, and video gain of 60 dB. The gradients were the same as shown in Table 5.1 and the sweep widths were the 'calculated' values in Table 5.1. To improve the S/N at higher gradients larger number of scans were averaged. The times for each projection are shown as the sweep time ("calculated" in Table 5.1). For example a 10 s sweep time corresponds to 90k rapid scans. The total data acquisition time was about 7 min. Initially the CW projections were obtained by using sweep times to match the rapid scan data acquisition times (Table 5.1). The modulation amplitude was 0.1 G for all the projections. Due to software and hardware restrictions the actual sweep widths were different from calculated (ideal) values. The averaging times that matched the rapid scan times gave projections for which the S/N was very poor at high gradients and resulted in

low quality images (Figure 5.3 B). The numbers of averages were increased to get better S/N which increased the acquisition time to about 104 min (Table 5.2).

Table 5.1 Parameters for CW projections with time comparable to Rapid Scan[a]

Angle	Gradient G/cm	Sweep (G) (calculated)	Sweep (G) (actual)	Sweep time (s) (rapid scan)	Sweep time(s) (actual)
-85	-10.00	21.0	21.1	125	41.94*3scans
-75	-3.27	10.2	9.4	15	2.62*5scans
-65	-1.88	8.0	7.0	12	1.31*9scans
-55	-1.25	7.0	7.0	10	10.49*1scan
-45	-0.87	6.4	7.0	10	10.49*1scan
-35	-0.61	6.0	7.0	9	1.31*7scans
-25	-0.41	5.7	4.7	8	2.62*3scans
-15	-0.23	5.4	4.7	8	2.62*3scans
-5	-0.08	5.1	4.7	8	2.62*3scans
5	0.08	5.1	4.7	8	2.62*3scans
15	0.23	5.4	4.7	8	2.62*3scans
25	0.41	5.7	4.7	8	2.62*3scans
35	0.61	6.0	7.0	9	1.31*7scans
45	0.87	6.4	7.0	10	10.49*1scan
55	1.25	7.0	7.0	10	10.49*1scan
65	1.88	8.0	7.0	12	1.31*9scans
75	3.27	10.2	9.4	15	2.62*5scans
85	10.00	21.0	21.1	125	41.94*3scans

[a] Rapid projections were obtained at 8.6 kHz scan frequency with gradients and scan widths as shown in this table.

Table 5.2 Parameters for CW projections with longer averaging time

Angle	Gradient G/cm	Sweep(G) (calculated)	Sweep(G) (actual)	Sweep time(s) (actual)
-85	-10	21	21.1	41.94*41scans =1720
-75	-3.27	10.2	9.4	2.62*41scans = 107
-65	-1.88	8	7	1.31*41scans =54
-55	-1.25	7	7	10.49*41scan = 430
-45	-0.87	6.4	7	10.49*41scan = 430
-35	-0.61	6	7	1.31*41scans = 54
-25	-0.41	5.7	4.7	2.62*41scans =107
-15	-0.23	5.4	4.7	2.62*41scans = 107
-5	-0.08	5.1	4.7	2.62*41scans =107
5	0.08	5.1	4.7	2.62*41scans = 107
15	0.23	5.4	4.7	2.62*41scans =107
25	0.41	5.7	4.7	2.62*41scans =107
35	0.61	6	7	1.31*41scans = 54
45	0.87	6.4	7	10.49*41scan = 430
55	1.25	7	7	10.49*41scan = 430
65	1.88	8	7	1.31*41scans = 54
75	3.27	10.2	9.4	2.62*41scans = 107
85	10	21	21.1	41.94*41scans =1720

Figure 5.3A shows a complete set of 18 rapid scan projections with equally spaced projection angles, with good S/N even at high gradients. In the resulting image the signals from the two tubes are well resolved, the linewidth differences are well defined, and the background regions of the image are relatively smooth. By contrast CW projections obtained with acquisition times comparable to those used for rapid scan (Figure 5.3 B) had very poor S/N. At high gradients the S/N is so poor that these

projections contributed little information to the image. The resulting image has poor resolution of the two tubes and the background regions of the image were very noisy. When the acquisition times for the CW projections were increased by a factor of about 15 (Figure 5.3 C) the S/N was still not as good as was obtained by rapid scan, but the resulting image was substantially improved relative to the image in Figure 5.3B.

A

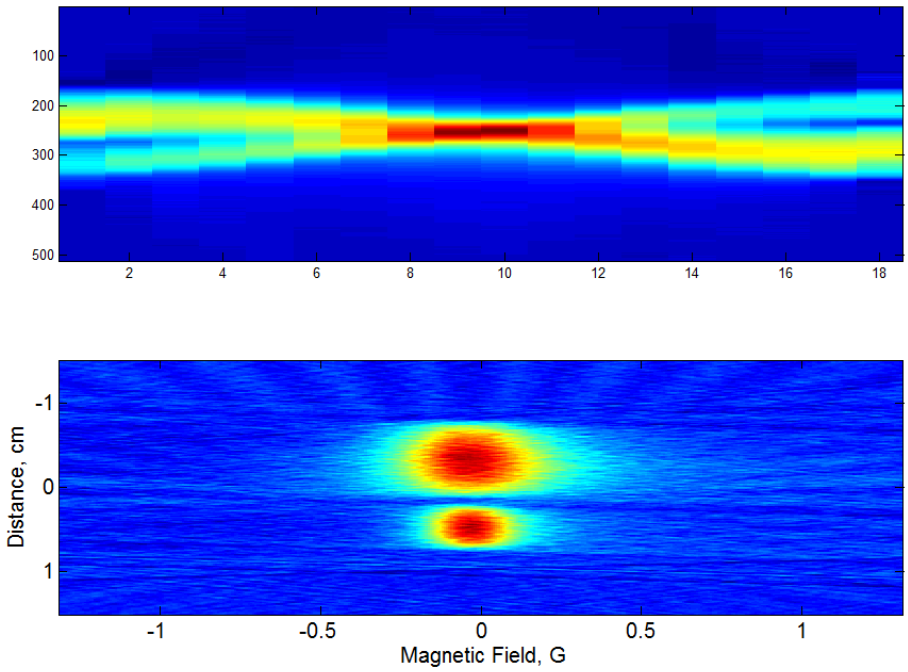
100
200
300
400
500
2
4
6
8
10
12
14
16
18
Distance, cm
-1
0
1
-1
-0.5
0
0.5
1
Magnetic Field, G

B

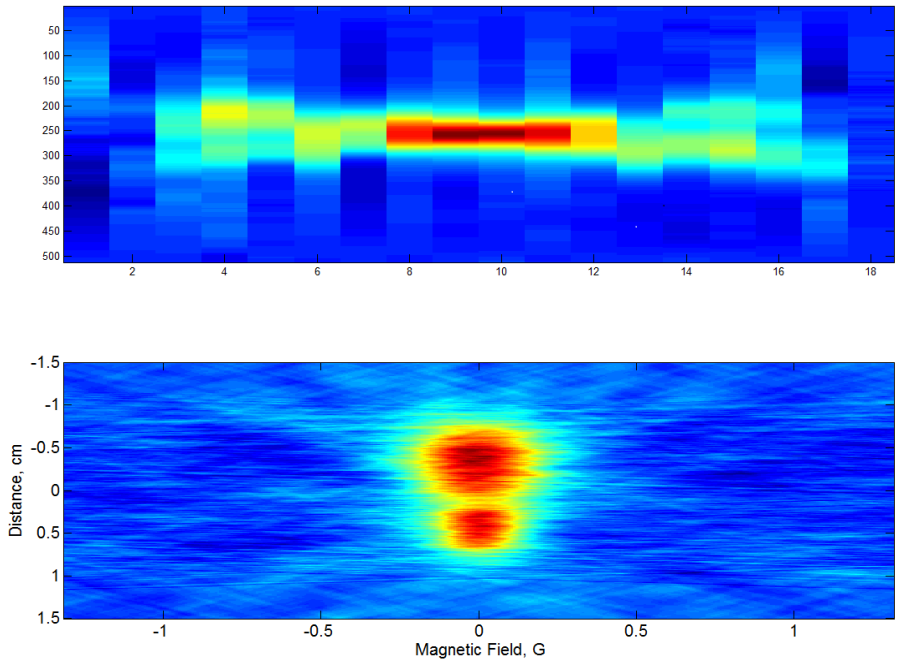
50
100
150
200
250
300
350
400
450
500
2
4
6
8
10
12
14
16
18
Distance, cm
-1.5
-1
-0.5
0
0.5
1
1.5
-1
-0.5
0
0.5
1
Magnetic Field, G

C

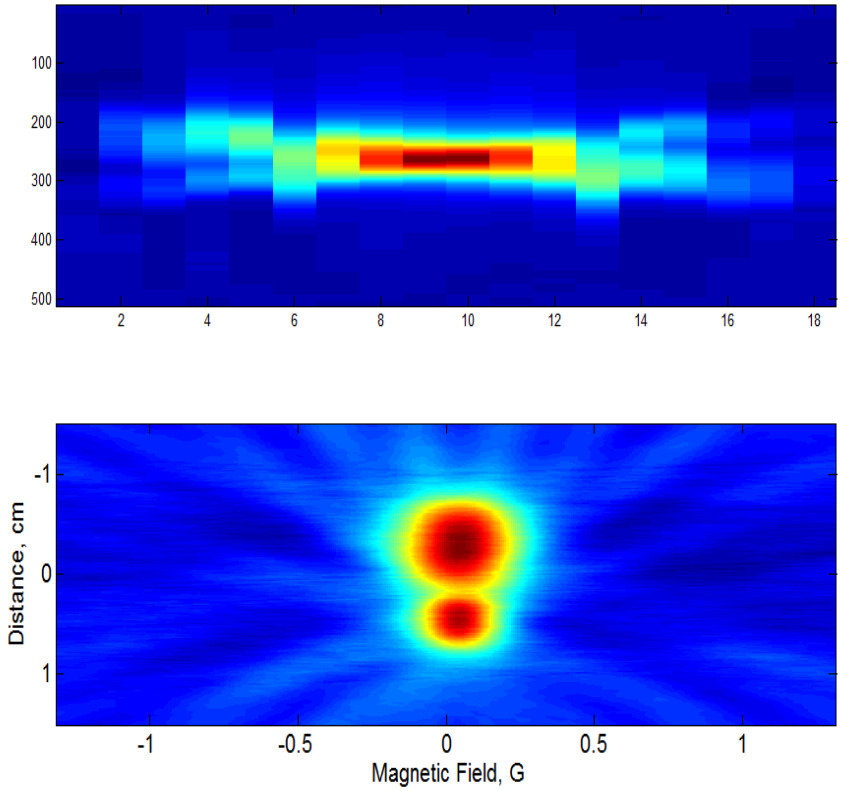

Figure 5.3 In each section of the figure the upper plot shows the projections as a function of the projection number from 1 to 18. The lower plot is the resulting 2D spectral-spatial images reconstructed by filtered backprojection. (A) Rapid scan projections. (B) CW projections with acquisition times comparable to rapid scan (Table 5.1). (C) CW projections obtained by averaging for 15 longer times (Table 5.2) than used for rapid scan.

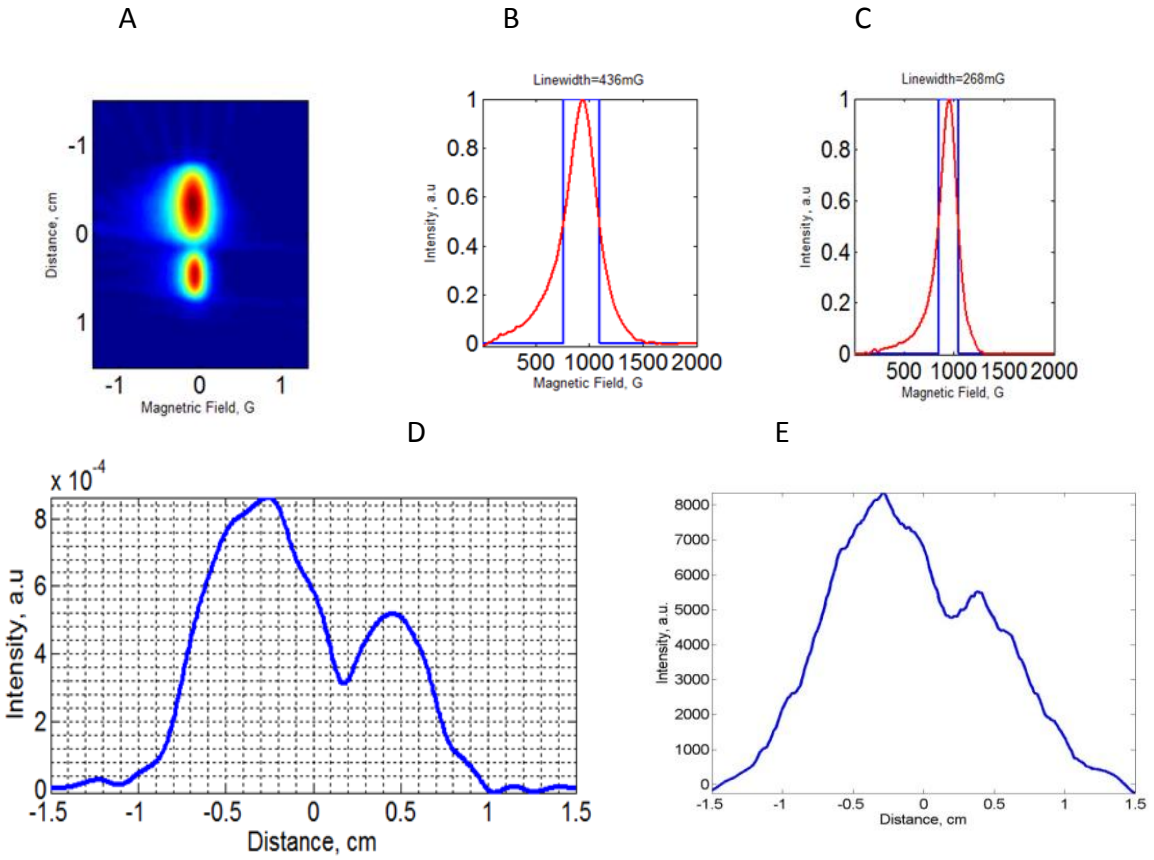

Figure 5.4 2D spectral-spatial images reconstructed by filtered backprojection (A). Linewidth for the sample equilibrated with air in 10 mm tube obtained from rapid scan image (B). Linewidth for the degassed sample in 6 mm tube obtained from rapid scan image (C). Signal intensity as a function of position in the rapid scan image. The separation between the two peaks indicates the distance between centers of tubes (D). Analogous intensity plot for the CW image (E).

These data demonstrate that imaging using rapid scan gives better results than with CW for the same acquisition time. This was indicated by comparing the S/N for individual projections and for reconstructed images and the ability to obtain useful projections at high gradients. The improvement in the S/N gives higher resolution in short acquisition time and will be the method of choice for future EPR imaging.

5.3. pH- sensitive Trityl (aTAM) Imaging Applications

This section shows the use of the pH- sensitive trityl (aTAM) probe discussed in Chapter 4 to map the pH by rapid scan imaging.

The phantom for imaging was constructed from two quartz tubes, separated by a 2 mm foam spacer. A 7 mm O.D. tube contained 0.5 mM $aTAM_4$ at pH 7.1 and a 6.1 mm O.D. tube contained 0.5 mM $aTAM_4$ at pH 6.5. The solvent was 20:80 ethanol: phosphate buffer (1.0 mM). Oxygen was removed by bubbling the solutions with N_2 prior to flame sealing the tubes.

Imaging parameters

The projections for the 2D spectra-spatial image were collected at 295 K on a spectrometer with an operating frequency of 251 MHz that includes a modified Bruker E540 console and gradient coils [57, 86, 87]. The sinusoidal scans were generated with a driver similar to the one described previously [85]. The cross loop resonator and scan coils are similar to the ones described in Ref. [88]. 18 projections were collected with 10.8 kHz sinusoidal scans and B_1 of 36 mG. The maximum gradient was 10 G/cm. The sweep widths ranged from 12 G at zero-gradient to 32 G at the highest gradient, which was sufficient to encompass the full gradient-broadened spectra. Signals were digitized with a Bruker Specjet II using 64k points per gradient and a 10 ns sampling interval which therefore encompassed 7.07 sinusoidal scan cycles within the digitizer time window. Each projection was averaged 49152 times which required 43s. The corresponding absorption signals were obtained by background correction [89], sinusoidal deconvolution [10], and combination of up-field and down-field scans. The

image was reconstructed by filtered backprojection. To permit image reconstruction by filtered backprojection (FBP) the high-gradient spectra were 'padded' with zeros at the low- and high-field ends to generate projections with the widths required for spectral-spatial imaging [90].

Because of the spectral dimension, an EPR spectral-spatial image constitutes a mathematical pseudo-object [91]. The equivalent of rotation in the spectral dimension is achieved by changing the gradient amplitude. The maximum angle for a particular set of experimental constraints can be calculated using Eq.(5.1) [92]:

$$\alpha_{\max} = \arctan(LG_{\max} / \Delta B) \tag{5.1}$$

where L is the spatial length of the image, ΔB is the spectral length of the image, and G_{max} is the maximum gradient. If ΔB is too large, Eq. (5.1) shows that either $G_{\max}$ must be extremely large (which may result in poor signal-to-noise), or the length L of the reconstructed image must be artificially increased relative to the sample size; otherwise α_{max} becomes too small relative to 90^o. Missing angle algorithms can compensate for small decreases in $\alpha_{\max}$ [93]. For aTAM$_4$ the spectral length is about 8 G, which is much smaller than the ~ 40 G for nitroxide radicals. The narrower width is advantageous for spectral-spatial imaging. Even with this narrow width, if the maximum gradient is 10 G/cm and L = 2 cm, α_{max} would be 68^o which would require many missing projections for the reconstruction. Instead, the α_{max} was set at 85^o which corresponds to L = 9 cm. The full image was reconstructed, but only the region of interest is displayed.

For a spectral-spatial EPR image, rapid scan has been shown to provide substantially higher signal-to-noise than CW for the same amount of data acquisition time [88]. A 2D spectral-spatial image of a phantom consisting of two tubes of $aTAM_4$ at pH = 6.5 and 7.1 was reconstructed from projections acquired by rapid scan (Figure 5.5). The spectral differences between the probe at the two different pHs is well resolved. Rapid scan EPR of trityls holds substantial promise for imaging pH with aTAM radicals. If the conventional algorithm for spectral spatial imaging had been used, a substantially wider sweep width would have been used for the highest gradient [90]. Instead, the sweep widths were selected to only be as wide as needed to encompass the gradient-broadened line. The full sweep width required for image reconstruction was generated by zero-filling the experimental data arrays.

Table 5.3 Imaging parameters to collect the image in Figure 5.5

Angle (degree)	Gradient G/cm	Gradient (Amp)	scan width (G)	scan width (Amp)
-85	-10	-18	32	2.5
-75	-3.27	-5.9	18.5	1.5
-65	-1.88	-3.38	15.8	1.25
-55	-1.25	-2.25	14.5	1.15
-45	-0.88	-1.58	13.8	1.09
-35	-0.61	-1.09	13.2	1.05
-25	-0.41	-0.74	12.8	1.02
-15	-0.23	-0.41	12.5	0.99
-5	-0.08	-0.144	12.2	0.97
0	0	0	12	0.95
5	0.08	0.144	12.2	0.97
15	0.23	0.41	12.5	0.99
25	0.41	0.74	12.8	1.02
35	0.61	1.09	13.2	1.05
45	0.88	1.58	13.8	1.09
55	1.25	2.25	14.5	1.15
65	1.88	3.38	15.8	1.25
75	3.27	5.9	18.5	1.5
85	10	18	32	2.5

Scan frequency is held constant at 10.8 KHz for all the projections

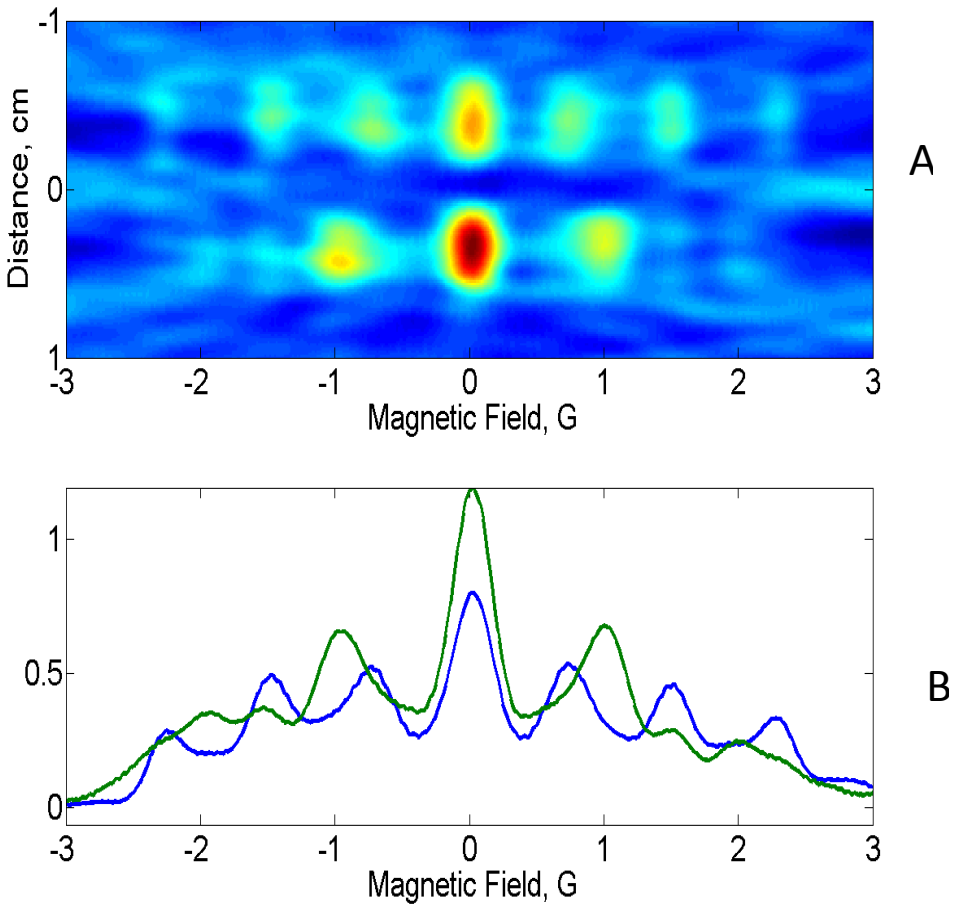

Figure 5.5 2D spectral-spatial image (A) of a phantom consisting of two tubes of 0.5 mM $aTAM_4$. (B) Spectral slices through the image at the locations of the centers of the tubes with pH=6.5 (green) and pH=7.1 (blue).

5.4. Full Spectrum Rapid Scan Imaging

A new algorithm has been developed by Dr. Mark Tseitlin to reconstruct full spectrum image [94]. Unlike conventional spectral-spatial imaging with filtered backprojection, the algorithm permits use of user-selected spacings of gradients. In this section this new method of reconstruction was applied to imaging of pH- sensitive trityl aTAM$_4$.

To construct a phantom, 6 mm tubes were filled to a height of 20 mm with pH sensitive triarylmethyl radicals (aTAM$_4$). The samples were prepared by dissolving radical in 200 μL absolute ethanol and diluting with 800 μL of 1 mM phosphate buffer for a final concentration of 0.5 mM in 80:20 buffer:ethanol. Solutions in the two tubes had pH of 7.2 and 7.0, respectively.

A scan frequency of 3 kHz was used for all projections. Table 5.4 shows the parameters under which the projections were collected. The microwave B_1 was 36 mG, which was in the linear response regime. Other parameters are 50 ns time base, 32768 points, and 19456 averages. The acquisition time per projection was 60 s. Three different gradient patterns were examined for image reconstruction by selecting a subset of the projections described in Table 5.4: (i) Equidistant gradient stepping from -10 G/cm to 10 G/cm with 1 G/cm step; (ii) FBP equidistant angle stepping of total 18 projections, 16 of which are spanned in the region from -3.2 to 3.2 G/cm; (iii) Projections were added to the FBP set that fill the gaps between ±3.2 and the maximum value of ±10 G/cm. These were the projections collected in the intervals from ±4 to ± 9 G/cm with 1 G/cm step and the zero-gradient projection. Comparison of the three gradient collection

schemes revealed that the third pattern produces the best results. Equidistant gradient sampling in scheme (i) produced distorted images. Scheme (iii) resulted in the image with a slightly better spatial resolution compared to the FBP scheme (ii). Scheme (iii) was used to reconstruct the image in Figure 5.6.

Table 5.4 Imaging parameters for full spectrum imaging algorithm

Gradient (G)	(Amp)	Scan width (G)	Scan width (Amp)
-10	-18	32	1.347
-9	-16.2	30	1.263
-8	-14.4	28	1.179
-7	-12.6	26	1.095
-6	-10.8	24	1.011
-5	-9	22	0.926
-4	-7.2	20	0.842
-3.27	-5.886	18.54	0.781
-1.88	-3.384	15.76	0.664
-1.25	-2.25	14.5	0.611
-0.88	-1.584	13.76	0.579
-0.61	-1.098	13.22	0.557
-0.41	-0.738	12.82	0.540
-0.23	-0.414	12.46	0.525
-0.08	-0.144	12.16	0.512
0	0	12	0.505
0.08	0.144	12.16	0.512
0.23	0.414	12.46	0.525
0.41	0.738	12.82	0.540
0.61	1.098	13.22	0.557
0.88	1.584	13.76	0.579
1.25	2.25	14.5	0.611
1.88	3.384	15.76	0.664
3.27	5.886	18.54	0.781
4	7.2	20	0.842
5	9	22	0.926
6	10.8	24	1.011
7	12.6	26	1.095
8	14.4	28	1.179
9	16.2	30	1.263
10	18	32	1.347

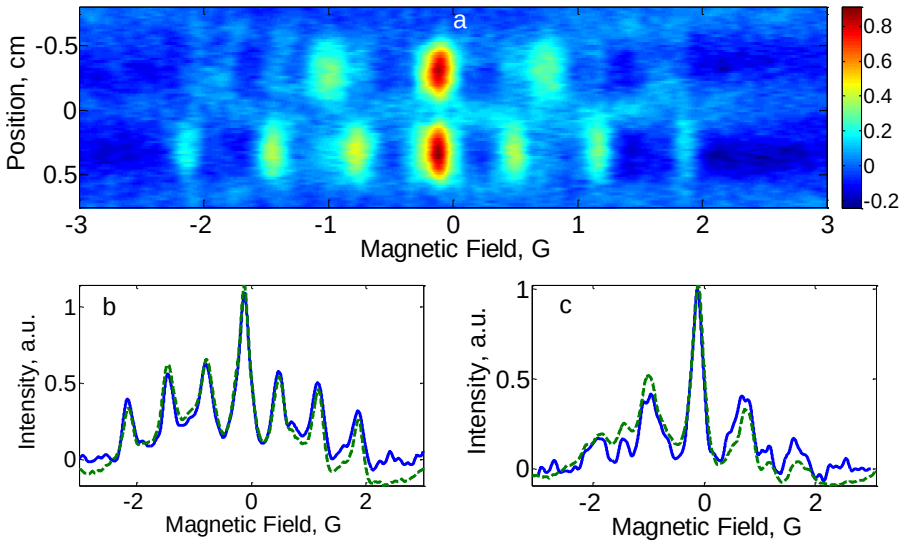

Figure 5.6 (a) 2D spectral-spatial image of phantom consisting of pH=7.0 and pH=7.2 $aTAM_4$ radicals. (b) Comparison of the spectral slice for pH=7.2 (blue) with the zero-gradient spectrum (dashed green). (c) Comparison of pH=7.0 slice (blue) with the zero-gradient spectrum (dashed green).

Chapter Six: X-Band Rapid Scan for Semiquinone Radicals and Spin Coherence Signal

6.1 Introduction

Electron spin resonance under rapid scan conditions has similarities with pulsed EPR. The transient response in a rapid magnetic field scan oscillates analogous to an FID (Free induction decay), but with a field dependent period because of the varying magnetic field. Each hyperfine component responds as predicted by the Bloch equation. When there are multiple equally spaced hyperfine lines, there are coherences in the signal response that produce an echo-like signal at a time that is determined by the hyperfine splitting [55]. Semiquinone radicals have small well-resolved nuclear hyperfine couplings to multiple equivalent protons. A coherence signal has been observed in the X-band rapid scan spectra for semiquinone radicals. The reciprocal of the time between excitation of the spin and the appearance of the coherence signal is equal to the hyperfine splitting obtained by CW EPR [55]. This spin coherence signal has been observed for 2,5-di-t-butyl-1,4-benzosemiquinone (25DTBSQ) and 2,3,5,6-tetramethoxy-1,4-benzosemiquinone (TMBSQ). Analogous spin coherences have been observed in saturation recovery experiments for semiquinones [55] and nitroxides [95]. For rapid scan EPR this is the first time that this spin coherence phenomena is being reported.

6.2 Materials and Method

Sample preparation

2,5-di-t-butyl-1,4-benzosemiquinone (25DTBSQ) radical was prepared by mixing equal volumes of air-saturated solutions of 2,5-di-t-butyl hydroquinone (5 mM) and KOH(5 mM) in ethanol.

2,3,5,6-tetramethoxy-1,4-benzosemiquinone (TMBSQ) radical was prepared by mixing 2:1 volume ratio of 25 mM KOH and 5 mM tetra fluoro-1,4-benzoquinone in methanol.

5 mm sample height of 25DTBSQ in ethanol in 4 mm EPR tube and 3 mm sample height of TMBSQ in methanol since the methanol is more lossy than the ethanol.

Oxygen removal

The vapor space in the tube was initially purged vigorously with N_2, after which N_2 was gently bubbled into the solution through thin Teflon tubing. Then samples were purged continuously with N_2.

EPR spectroscopy

Rapid scan signals were obtained on a Bruker E500T X-band spectrometer with a Bruker Flexline ER4118X-MD5 dielectric resonator as described in [14]. The scan coils were constructed from 200 turns of Litz wire that have inductance of 8.6 mH and a coil constant of 37.7 G/A. The resonator Q was measured using a network analyzer. Q was 320 for 25DTBSQ in ethanol and 99 for TMBSQ in methanol. A locally designed sinusoidal magnetic field scan driver, which is a slightly modified version of that described in [85], was used. Signal was acquired with a Bruker SpecJetII fast digitizer.

The rapid scan spectra were collected at several different scan frequencies and scan widths to observe the effect of the rate on the coherence signal.

6.3 Results and Discussion

25DTBSQ

The primary ^{1}H hyperfine splitting in 25DTBSQ results in a 3-line pattern with a_H = 2.14 G as shown in Figure 6.1. Further splitting due to the 18 equivalent t-butyl protons can be seen in the conventional first-derivative EPR spectrum when low microwave power and low modulation amplitude are used (Figure 3.3A). The experimental spectra were simulated using a t-butyl hyperfine coupling of 59 mG.

In addition to the expected signals, the rapid scan response showed patterns at defined times after passage through the EPR lines. The position of these patterns on a time axis is a direct measure of the hyperfine splitting, and its location in a particular rapid scan response depended on the magnetic field scan frequency (2.6, 2.7, 2.9, 3.5, 7.7 and 19.8 kHz, Figures 6.1-6.6) because the scaling between time and magnetic field changes with scan frequency. When the scan frequency was increased to 41 KHz, rapid scan wiggles were observed, the spacing in gauss between the primary resonances and the coherence signal increased, and the amplitude of the coherence signal decreased (Figure 6.7). In these 10 G wide scans the coherence signal was observed for the first two of the major proton hyperfine lines, but not the third (Figures 6.1 – 6.7). To test whether there was something particular to the third line that prevented observation of the coherence, a 2D experiment was performed with 2 G scans and 7.7 KHz scan frequency. This narrow

sweep encompasses only one of the major proton hyperfine lines in each scan. The center field was stepped from 3427.5 G to 3442.5 G with 0.3 G step. Three slices from the 2D array are shown in Figure 6.8 – 6.10. The spin coherence was observed for each of the major hyperfine lines when observed independently. Also, when the scan direction was reversed, the coherence was observed for the high-field and center-field line, but not the low-field line. This again confirmed that the lack of a coherence signal was not due to differences in spin properties. The small hyperfine splittings from the t-butyl protons are resolved in the deconvolved absorption spectra (Figures 6.8-6.10).

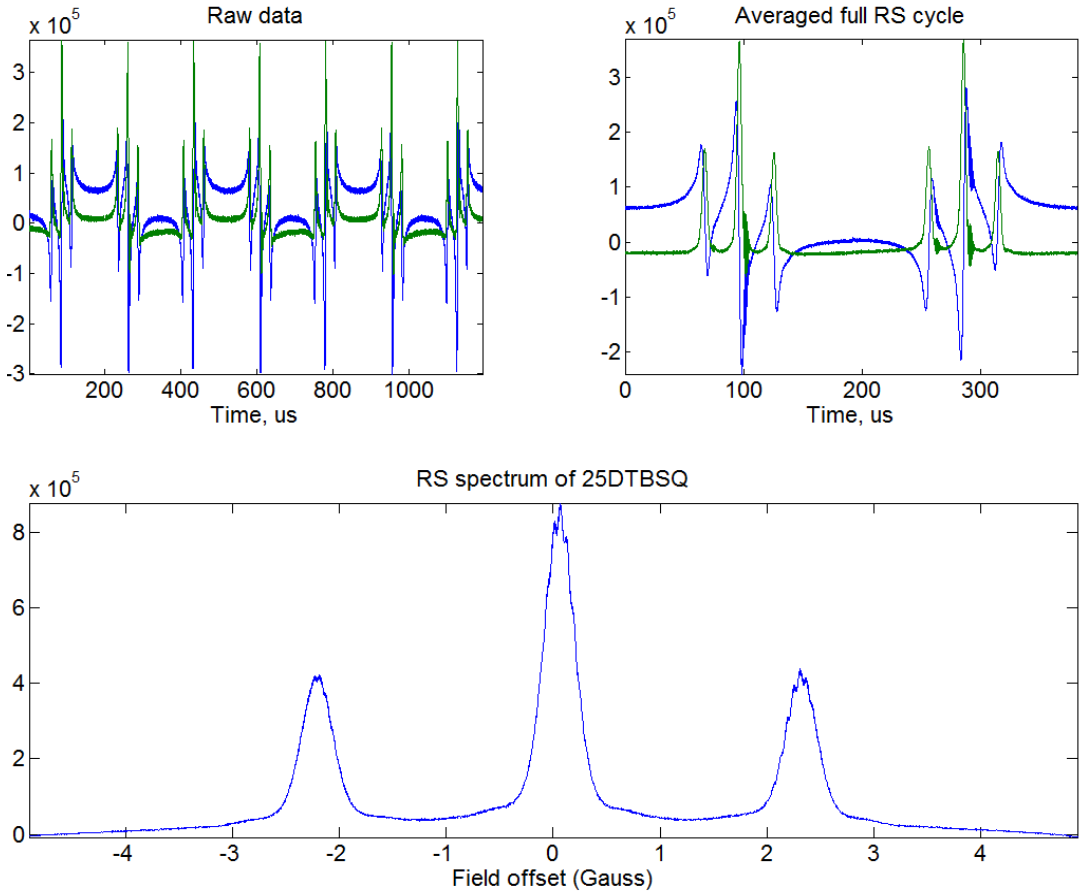

Figure 6.1 Rapid scan spectrum for 25DTBSQ at X-band with scan frequency of 2.6 KHz and 10 G sweep width. In the rapid scans the signal is observed in both the up-field and down-field scans. Data are acquired in quadrature: absorption (green) and dispersion (blue). Multiple cycles of the rapid scans are averaged to obtain the full-cycle spectrum (upper right). The spectrum, after deconvolution of the rapid scan effect, is shown in the lower panel.

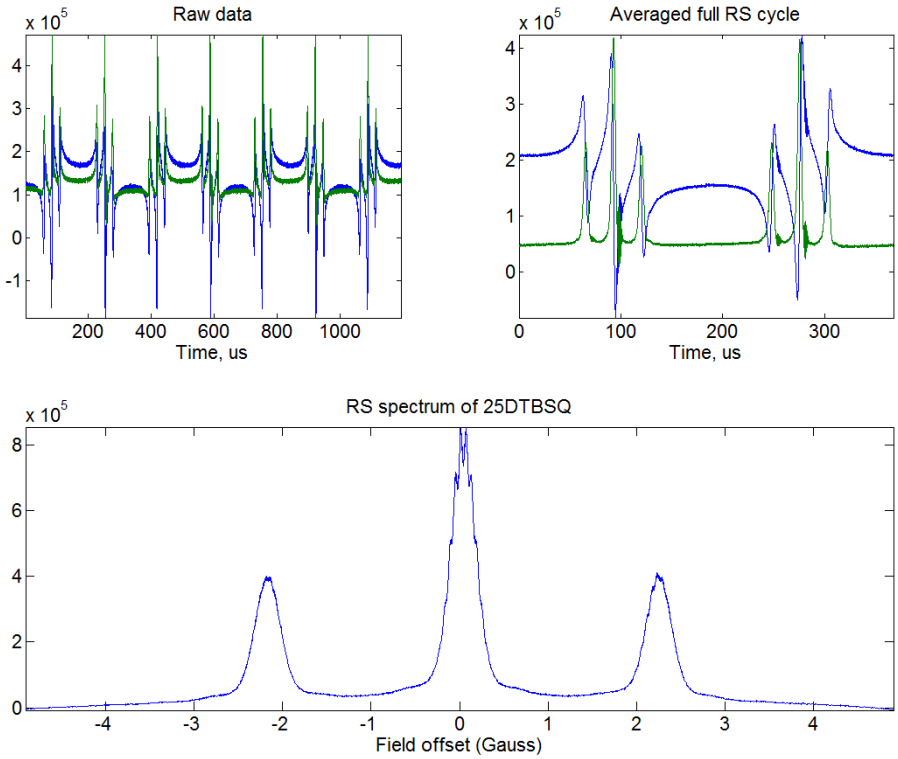

Figure 6.2 Rapid scan spectrum for 25DTBSQ at X-band with scan frequency of 2.7 KHz and 10 G sweep width. Labeling is the same as in Figure 6.1.

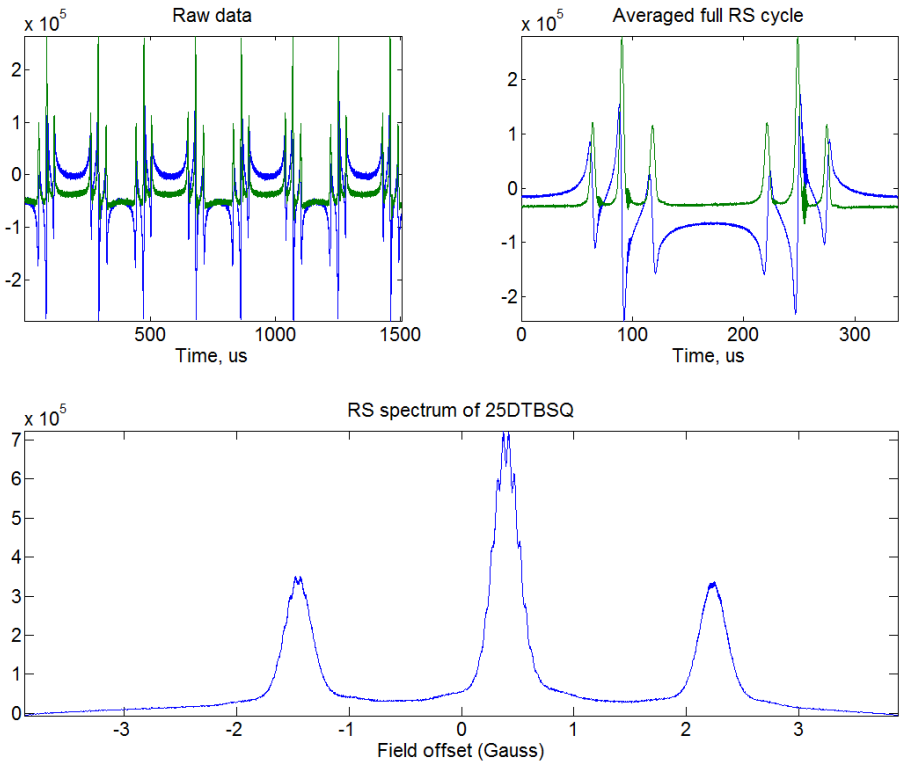

Figure 6.3 Rapid scan spectrum for 25DTBSQ at X-band with scan frequency of 2.9 KHz and 10 G sweep width. Labeling is the same as in Figure 6.1.

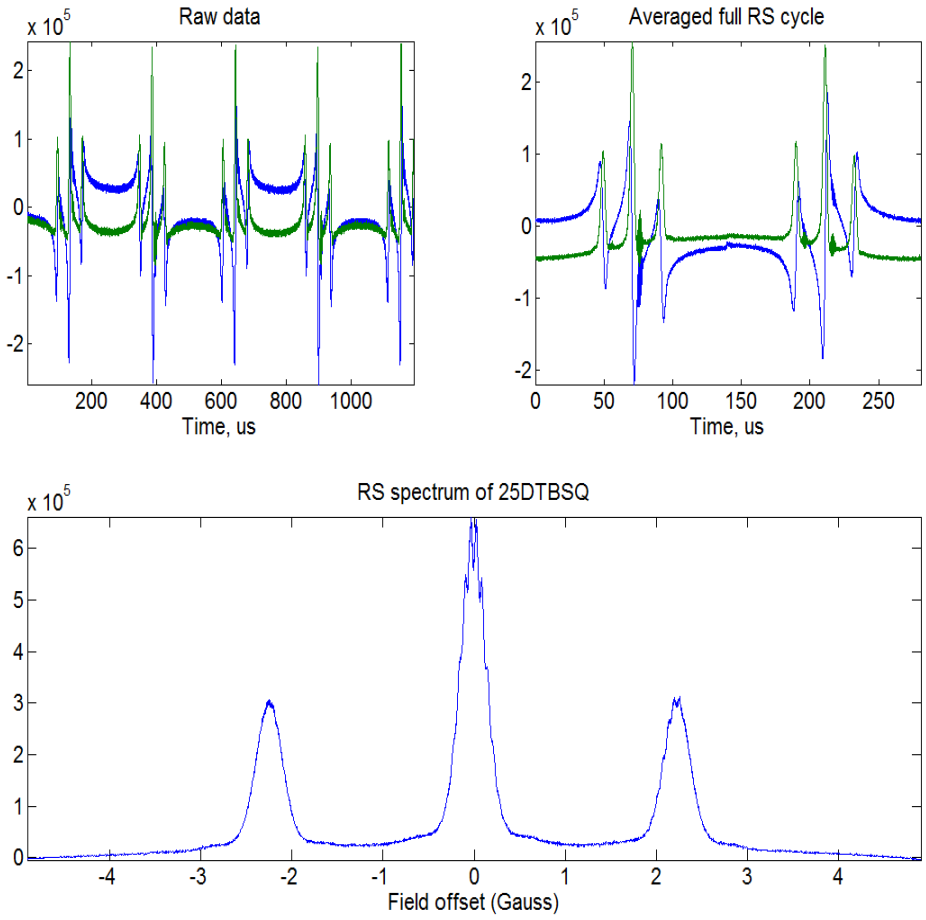

Figure 6.4 Rapid scan spectrum for 25DTBSQ at X-band with scan frequency of 3.5 KHz and 10 G sweep width. Labeling is the same as in Figure 6.1.

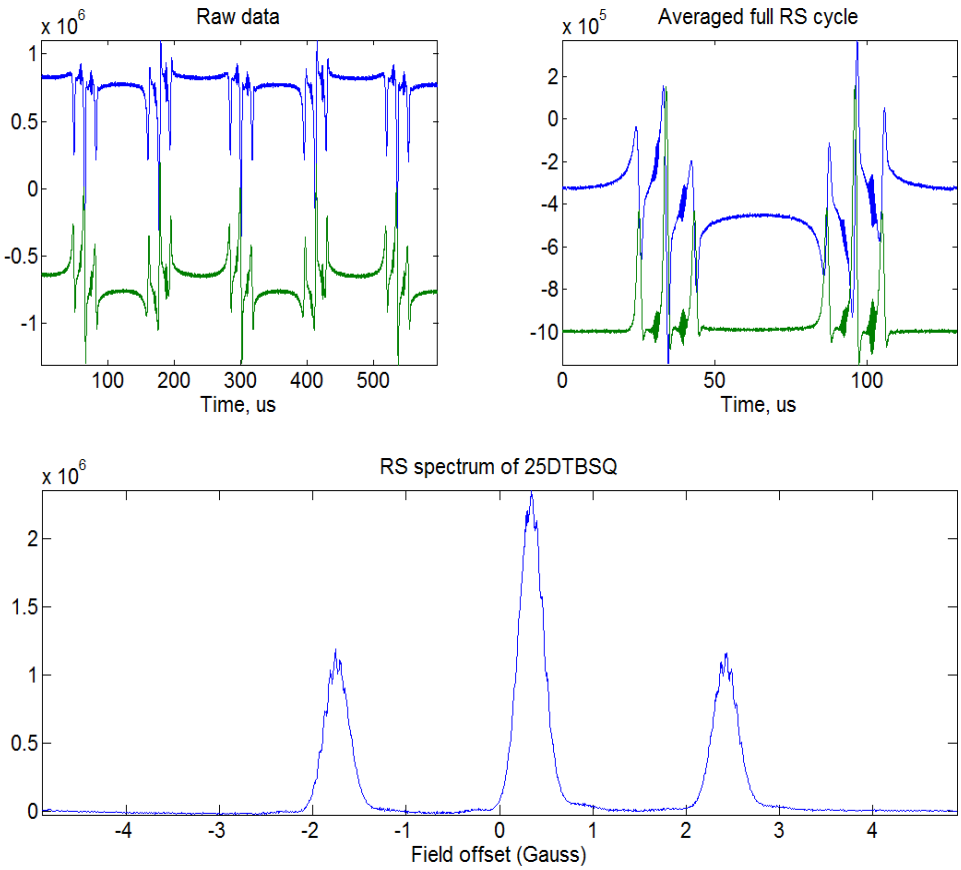

Figure 6.5 Rapid scan spectrum for 25DTBSQ at X-band with scan frequency of 7.7 KHz and 10 G sweep width. Labeling is the same as in Figure 6.1.

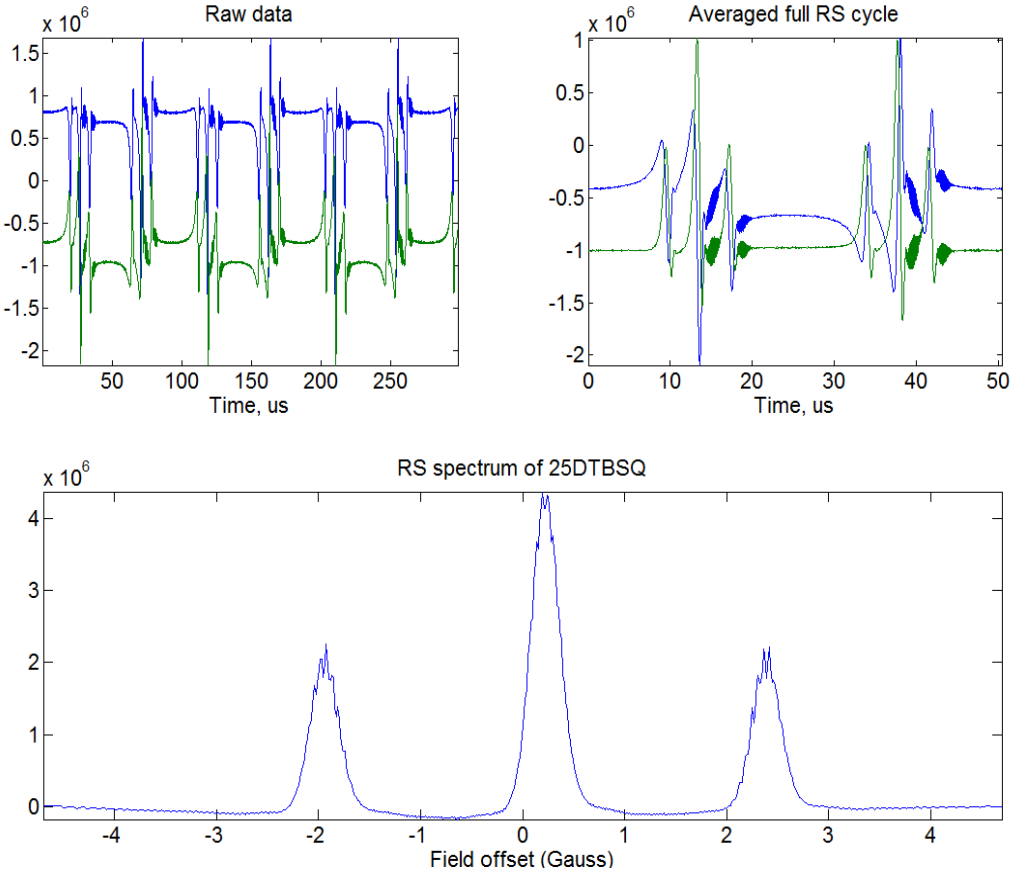

Figure 6.6 Rapid scan spectrum for 25DTBSQ at X-band with scan frequency of 19.8 KHz and 10 G sweep width**.** Labeling is the same as in Figure 6.1.

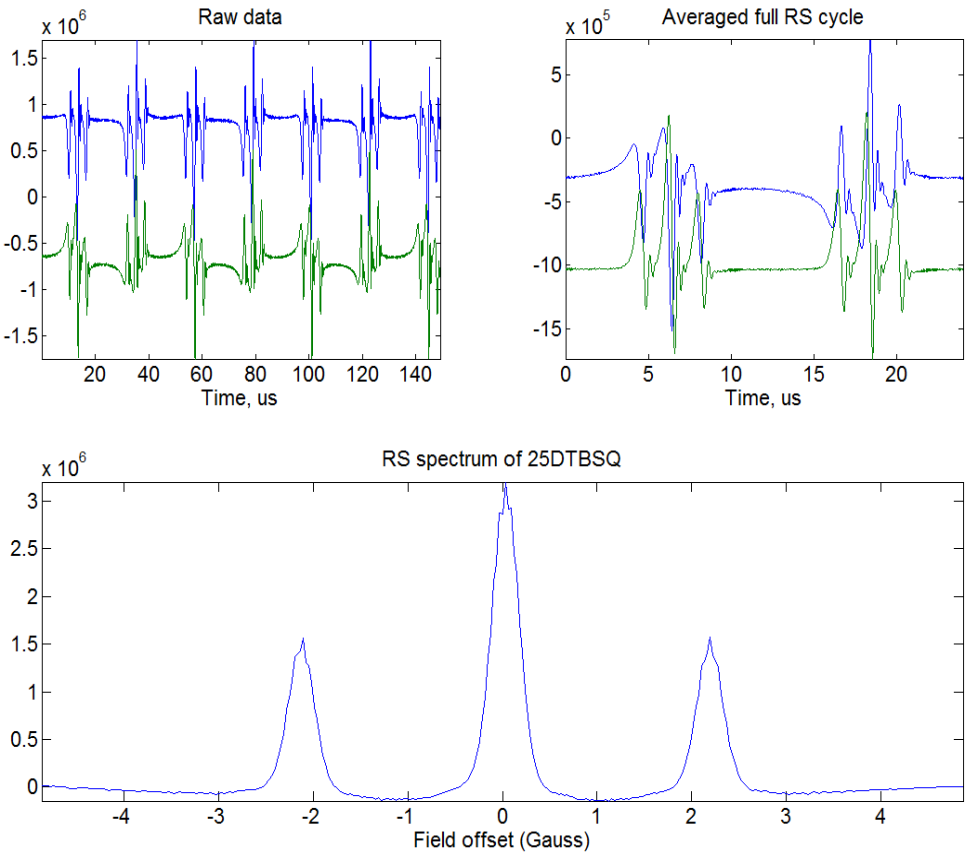

Figure 6.7 Rapid scan spectrum for 25DTBSQ at X-band with scan frequency of 41.6 KHz and 10 G sweep. Labeling is the same as in Figure 6.1.

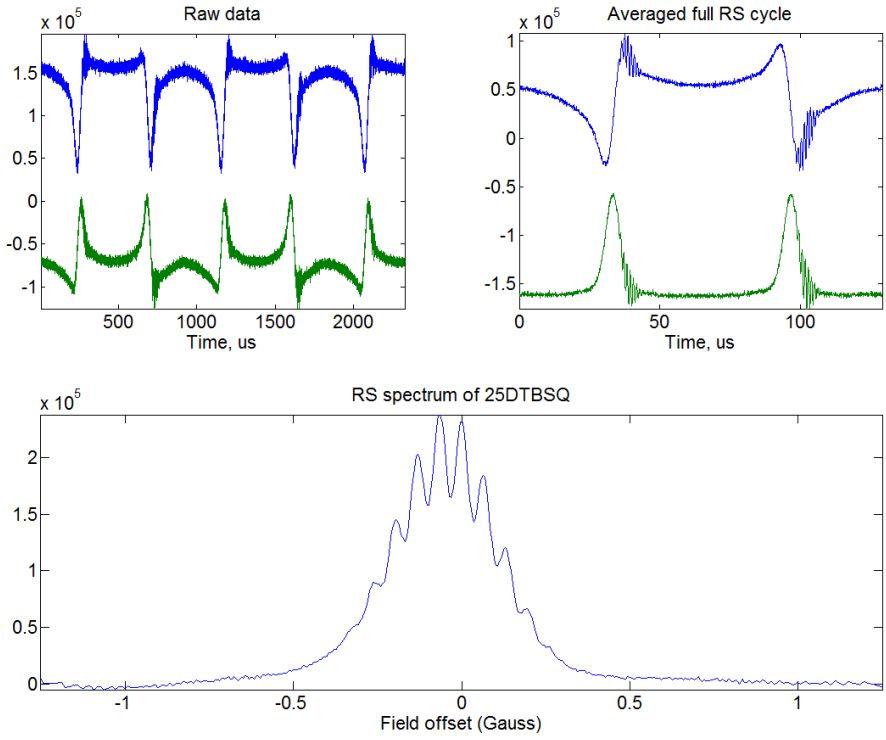

Figure 6.8 Spin coherence from the low field hyperfine line of 25DTBSQ obtained with 7.7 KHz and 2 G sweep width. Labeling is the same as in Figure 6.1.

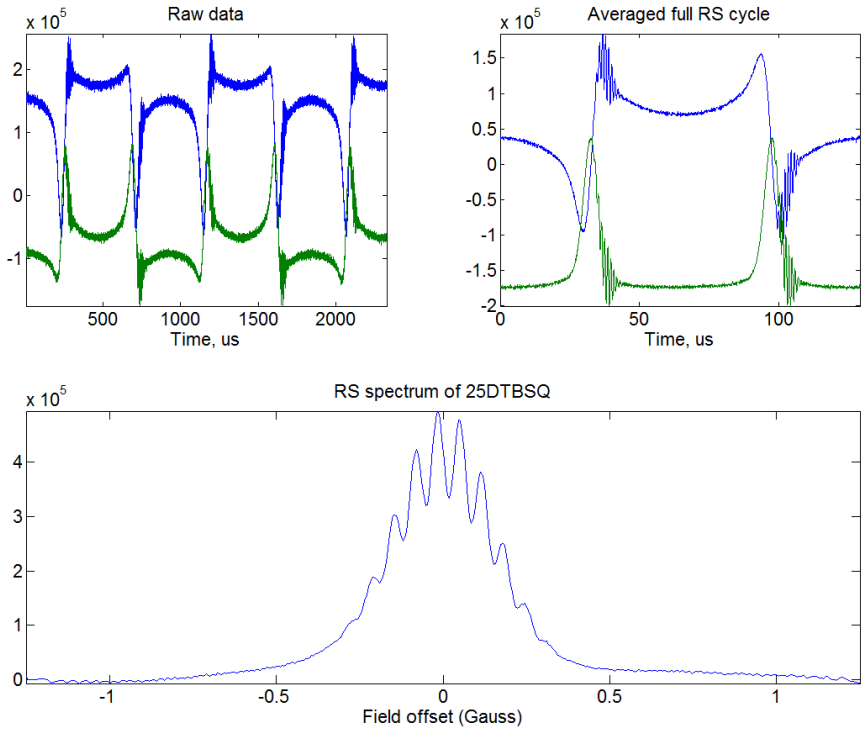

Figure 6.9 Spin coherence from the center field hyperfine line of 25DTBSQ obtained with 7.7 KHz and 2 G sweep width.

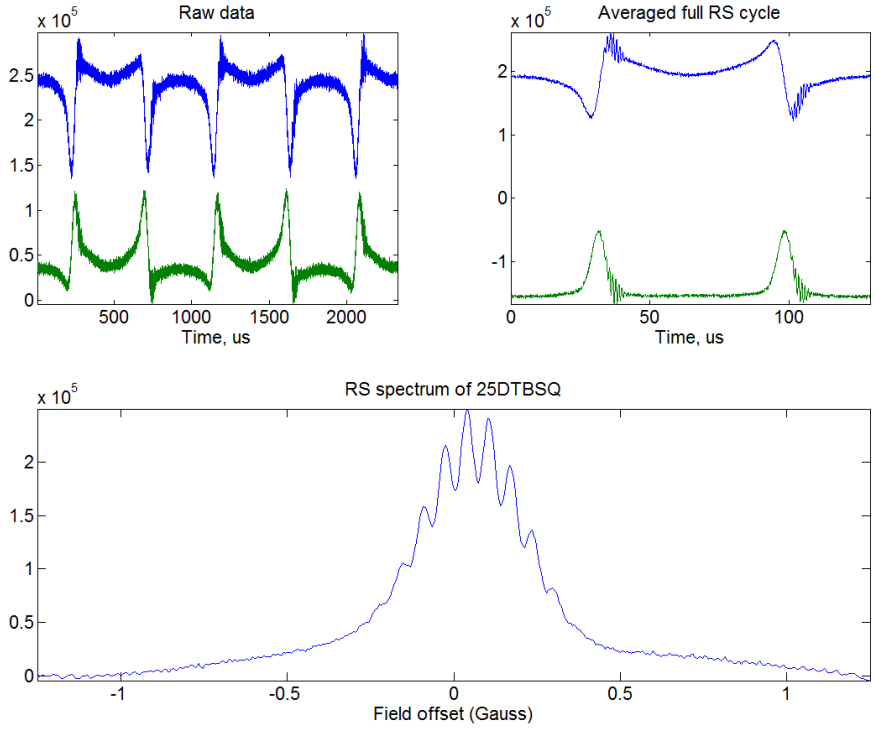

Figure 6.10 Spin coherence signal from high field hyperfine line of 25DTBSQ obtained with 7.7 KHz and 2 G sweep width. Labeling is the same as in Figure 6.1.

Scan Frequency and the Frequency of the Coherence Signal

The frequency of the coherence signal increases linearly with increasing scan rate or scan frequency (Figure 6.11). The slope of a plot of scan rate versus the coherence frequency in gauss equals the hyperfine splitting as shown in Figure 6.12.

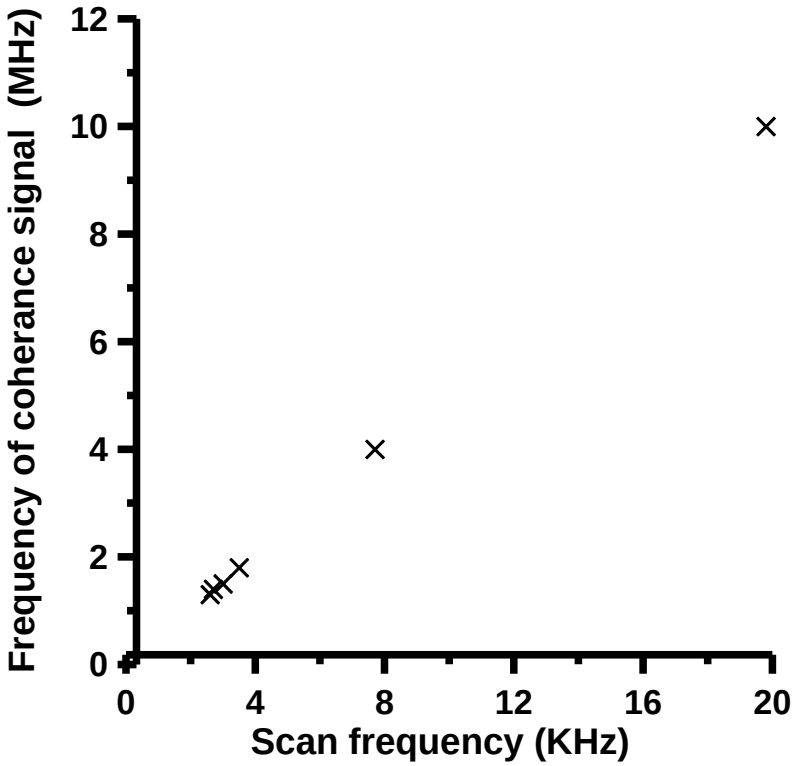

Figure 6.11 The dependence of the frequency of the coherence signal on the scan frequency.

Table 6.1 Scan frequencies used and the frequency of the coherence signal

Scan frequency (KHz)	Frequency of coherence signal (MHz)
2.6	1.3
2.7	1.4
3.0	1.5
3.5	1.8
7.7	4
19.8	10

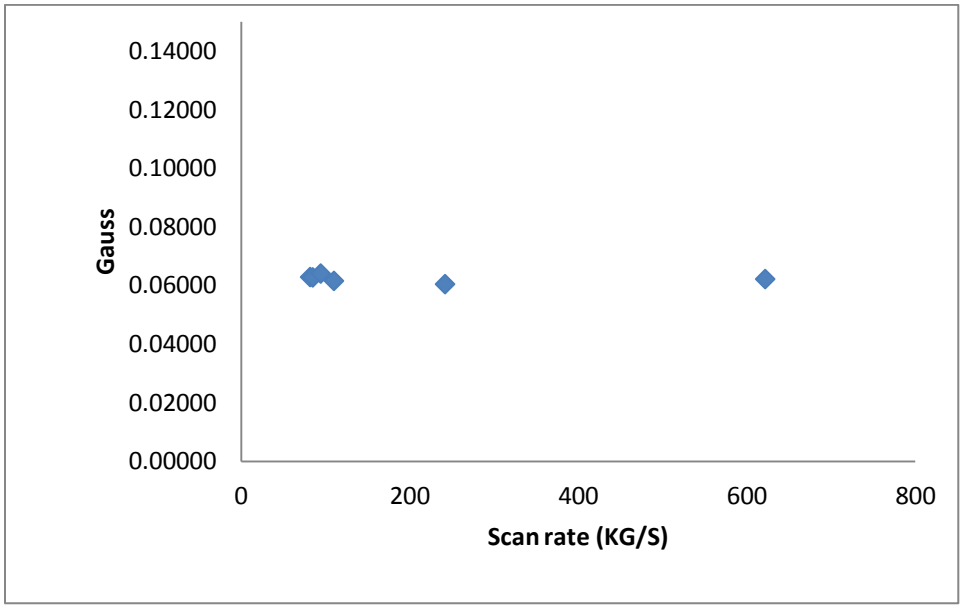

Figure 6.12 Relationship between the scan rate and the coherence frequency in units of gauss

Table 6.2 The rate of the scan and coherence frequency converted into gauss

rate(KG/s)	Rate(G/s) * coherence frequency (s)
81.6	0.063
84.8	0.063
94.2	0.064
109.9	0.062
241.8	0.060
621.7	0.062

TMBSQ

For TMBSQ the coherence signal was observed with 7.7 KHz scan frequency (Figure 6.13) and 20.8 KHz scan frequency (Figure 6.14). At 41.6 KHz the spin coherence was barely detectable and the signal was in the rapid scan regime (Figure 6.15). With 2.6 KHz scan frequency the coherence signal was not observed (Figure 6.16).

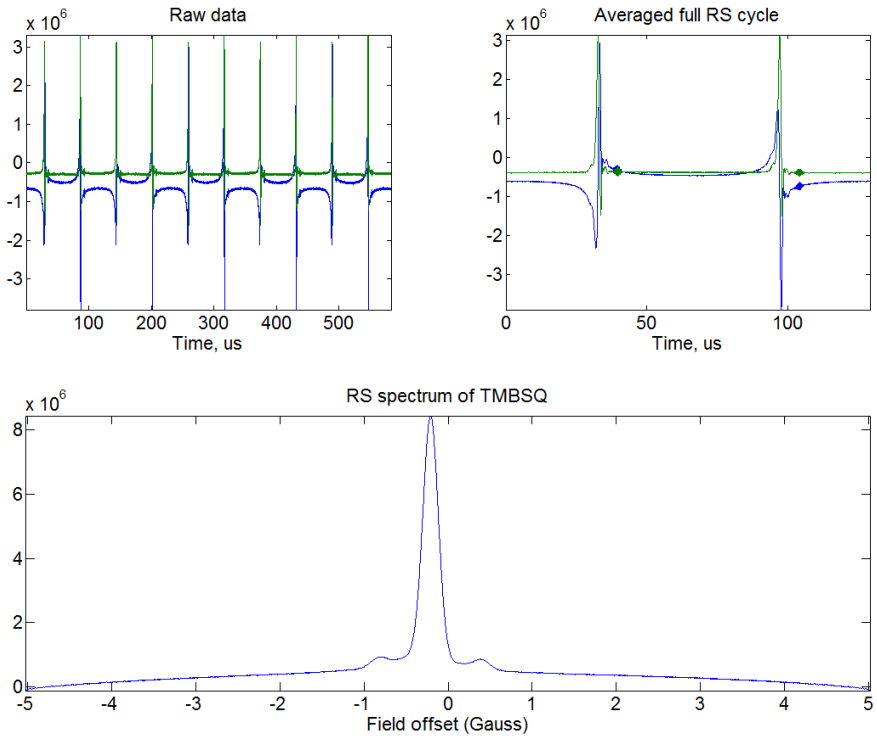

Figure 6.13 Rapid scan spectrum for TMBSQ at X-band with scan frequency of 7.7 KHz and 10 G sweep width. Labeling is the same as in Figure 6.1.

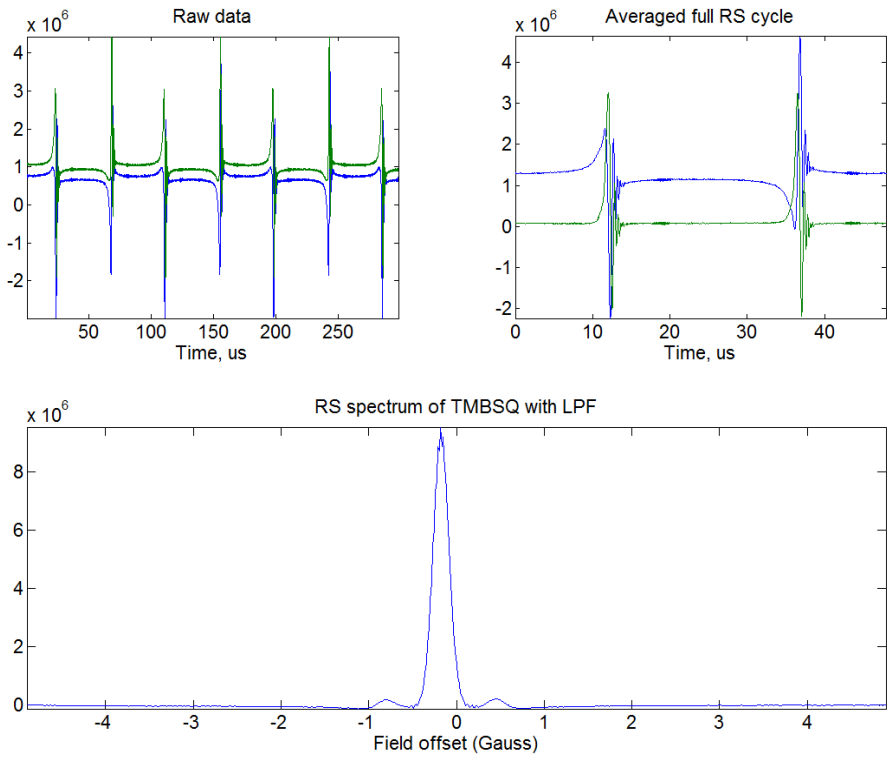

Figure 6.14 rapid scan spectrum for TMBSQ at X-band with scan frequency of 20.8 KHz and 10 G sweep. Labeling is the same as in Figure 6.1.

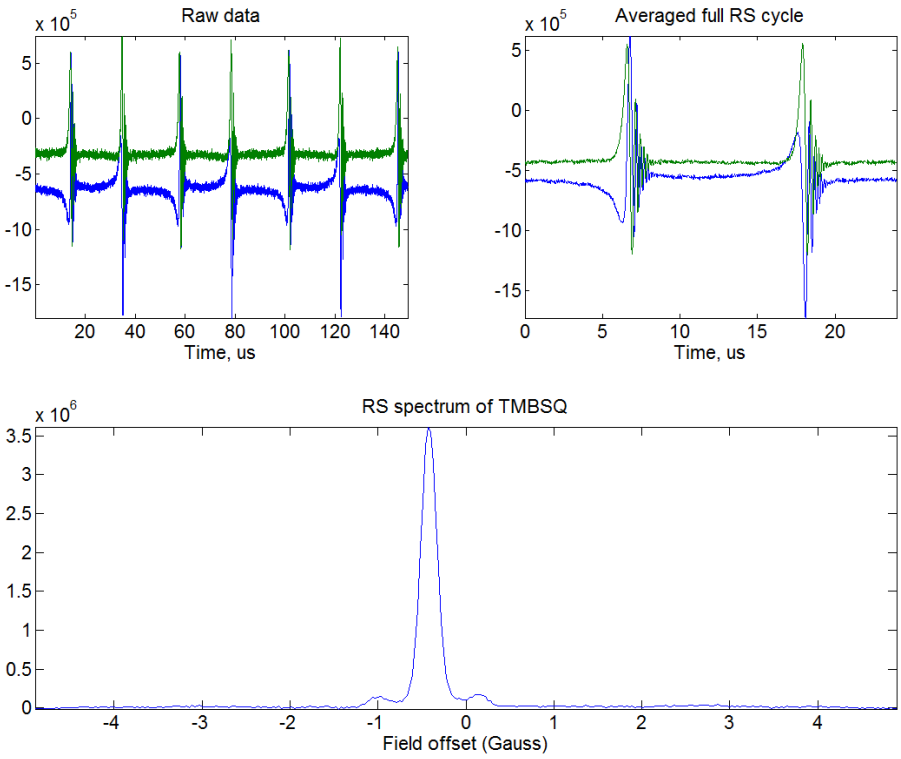

Figure 6.15 Rapid scan spectrum for TMBSQ at X-band with scan frequency of 41.6KHz and 10 G sweep width. Labeling is the same as in Figure 6.1.

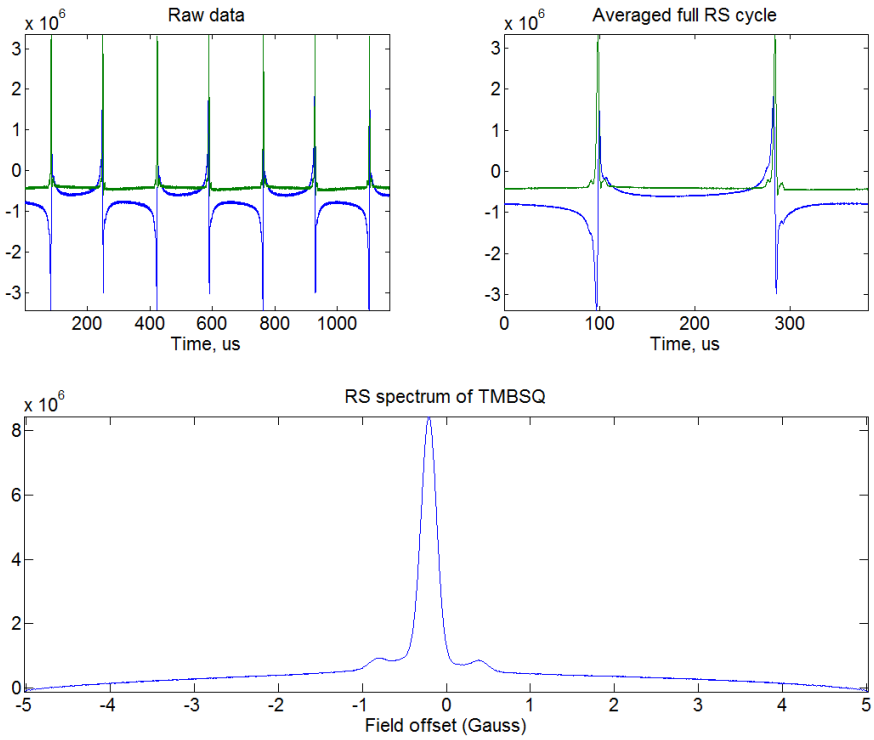

Figure 6.16 Rapid scan spectrum for TMBSQ at X-band with scan frequency of 2.6 KHz and 10 G sweep width. Labeling is the same as in Figure 6.1.

The spin coherence described here is expected to occur in rapid scan spectra of any radical with a dominant multiple line hyperfine pattern with small a_H. Even when rapid scan spectra are obtained under conditions that do not clearly reveal the hyperfine, the coherence signal time location identifies the magnitude of the hyperfine splitting. For larger hyperfine splitting, the reciprocal of the hyperfine splitting is so small that the coherence is difficult to observe.

The reason why the coherence signals were observed for only two of the three major proton hyperfine lines Figure 6.1 to 6.7 is not understood and will require further investigation.

Chapter Seven: Conclusion and Future Work

Throughout this dissertation, various EPR methods have been used to investigate several issues. In pulsed EPR, the saturation recovery experiment has the advantage of giving a true T_1 because the long saturating pulses can decrease the impact of spectral diffusion, but it is not an easy experiment to perform. The low observe power makes sensitivity low compared to inversion recovery, and the detection is very sensitive to experimental conditions. In spite of this difficulty the experiment was performed successfully for several samples.

Enhancing the stability of the semiquinone radicals permitted the understanding of the relaxation mechanisms through extensive frequency dependence studies at up to 8 frequencies between 250 MHz and 34 GHz. The experiments showed that the relaxation rates in solvents with normal isotope abundance are about a factor of 2 faster at lower frequencies than at 9 or 34 GHz. However, in perdeuterated alcohols the relaxation rates exhibit little frequency dependence. The relaxation rates were modeled as the sum of two frequency-independent contributions (spin rotation and a local mode) and two frequency-dependent contributions (modulation of dipolar interaction with solvent nuclei and a much smaller contribution from modulation of g-anisotropy). The correlation time for modulation of the interaction with solvent nuclei is longer than the tumbling correlation time, and is attributed to hydrogen bonding of the alcohol to the oxygen atoms of the

semiquinones. Some of the chemistry behind the stability and the interaction between the semiquinone and dioxygen needs to be investigated more.

Amino-substituted trityl radicals have the potential to monitor pH and local O_2 concentration in vivo. This was the goal for synthesizing these kinds of probes, and it was demonstrated previously with CW EPR. In this dissertation the feasibility of maintaining this dual function potential in pulsed EPR was examined. Electron spin relaxation times T_1 and T_2 were measured at X-band for the protonated and deprotonated forms of two amino-substituted triaryl methyl radicals. T_1 exhibits little dependence on protonation, which makes it useful for measuring O_2 concentration. Values of T_2 vary substantially with pH, reflecting a range of dynamic processes. It was concluded that these probes are suitable to be dual function probes for pulsed EPR. Measuring the relaxation times at low frequency may provide more insight about the relaxation of these radicals. Also, oxygen sensitivity using pulsed EPR needs to be demonstrated, because only the pH sensitivity was examined in this dissertation.

EPR imaging methods have been developed for the last several years in multiple laboratories. Gaining knowledge about the imaging method of choice for the information needed is what motivated the comparison study for several EPR imaging methods. In this dissertation CW and rapid scan methods for imaging the effect of O_2 on the linewdth of the nitroxide probe ^{15}NPDT were compared. This study reveals that rapid scan is the method of choice because of improvements in the S/N for the same acquisition time and the improved resolution for rapid scan images compared to CW in a short acquisition time. It was demonstrated that rapid scan is a promising method for imaging pH sensitive

trityl probes. The rapid scan method is predicted to be better than pulsed EPR imaging, which is restricted by the dead time of the resonator and, in many cases, by the duty cycle of the pulsed amplifier. Further study to compare rapid scan and pulse imaging would be interesting.

A spin coherence phenomenon was observed in the X-band rapid scan spectra for semiqunone radicals with small equally-spaced nuclear hyperfine splittings. This phenomenon was investigated both experimentally and by computation. It is proposed that the origin of this coherence signal is the interference of signals from the multiple equally-spaced hyperfine lines from the 18 equivalent t-butyl protons for 25DTBSQ (a_H = 0.059G) or the 12 methoxy protons for TMBSQ (a_H = 0.046 G). In a narrow scan that encompassed only one of the three resolved lines (a_H = 2.14 G) of the 25DTBSQ spectrum, the coherence was observed from each line and the small hyperfine splittings of a_H = 0.06G were resolved well in the rapid scan absorption spectra. It was predicted by simulation that the full spectrum rapid scan would give three coherence signals for 25DTBSQ. However, the experimental data show only two coherence signals. Work is underway to understand the mismatch between the experiments and the simulations. One hypothesis is that the coherence signal is affected by field inhomegeneties due to eddy currents. A resonator that is expected to have smaller field inhomogeneity will be tested next.

References

[1] G.R. Eaton, S.S. Eaton, D.P. Barr, R.T. Weber, *Quantitative EPR*, Springer Wien: New York, NY, 2010.

[2] J.A. Weil, J.R. Bolton, Electron Paramagnetic Resonance: Elementary Theory and Practical Applications, 2 ed., ;John Wiley & Sons: Hoboken NJ, 2007.

[3] A. Zecevic, G. R. Eaton, S. S. Eaton, and M. Lindgren, Dephasing of Electron Spin Echoes for Nitroxyl Radicals in Glassy Solvents by Non-methyl and Methyl Protons, Molecular Physics, 95 (1998) 1255-1263.

[4] S.S. Eaton, G.R. Eaton, Relaxation Times of Organic Radicals and Transition Metal Ions. In Biological Magnetic Resonance: Distance Measurements in Biological Systems by EPR, Kluwer Academic/Plenum Publishers: New York, NY, 2000

[5] S.S. Eaton, G.R. Eaton, Saturation Recovery EPR, in: J. Cazes (Ed.) Ewing's Analytical Instrumentation Handbook, Marcel Dekker, 2005.

[6] N. Bloembergen, E.M. Purcell, R.V. Pound, Relaxation Effects in Nuclear Magnetic Resonance Absorption, Physical Review, 73 (1948) 679-712.

[7] R. Beeler, D. Roux, G. Bene, R. Extermann, Observation de Battements en Resonance Magnetique Electronique, Comptes Rendus Hebdomadaires Des Seances De L Academie Des Sciences, 241 (1955) 472-474.

[8] R. Beeler, D. Roux, G. Bene, R. Extermann, Rapid-Passage Effects in Electron Spin Resonance, Physical Review, 102 (1956) 295-295.

[9] M. Tseitlin, G.A. Rinard, R.W. Quine, S.S. Eaton, G.R. Eaton, Rapid Frequency Scan EPR, Journal of Magnetic Resonance, 211 (2011) 156-161.

[10] M. Tseitlin, G.A. Rinard, R.W. Quine, S.S. Eaton, G.R. Eaton, Deconvolution of Sinusoidal Rapid EPR Scans, Journal of Magnetic Resonance, 208 (2011) 279-283.

[11] D.G. Mitchell, R.W. Quine, M. Tseitlin, V. Meyer, S.S. Eaton, G.R. Eaton, Comparison of Continuous Wave, Spin Echo, and Rapid Scan EPR of Irradiated Fused Quartz, Radiation Measurements, 46 (2011) 993-996.

[12] D.G. Mitchell, R.W. Quine, M. Tseitlin, R.T. Weber, V. Meyer, A. Avery, S.S. Eaton, G.R. Eaton, Electron Spin Relaxation and Heterogeneity of the 1:1 alpha,gamma-Bisdiphenylene-beta-phenylallyl (BDPA)/Benzene Complex, Journal of Physical Chemistry B, 115 (2011) 7986-7990.

[13] D.G. Mitchell, M. Tseitlin, R.W. Quine, V.M. Meyer, G.R. Eaton, S.S. Eaton, X-band rapid-scan EPR, Abstracts of Papers of the American Chemical Society, 242 (2011).

[14] D.G. Mitchell, M. Tseitlin, R.W. Quine, V. Meyer, M.E. Newton, A. Schnegg, B. George, S.S. Eaton, G.R. Eaton, X-band Rapid-Scan EPR of Samples with Long Electron Spin Relaxation Times: a Comparison of Continuous Wave, Pulse and Rapid-Scan EPR, Molecular Physics, 111 (2013) 2664-2673.

[15] H.J. Halpern, M. Peric, T.D. Nguyen, D.P. Spencer, B.A. Teicher, Y.J. Lin, M.K. Bowman, Selective Isotropic Labeling of a Nitroxide Spin Label to Enhance Sesitivity for T_2 Oxymetry, Journal of Magnetic Resonance, 90 (1990) 40-51.

[16] S.R. Burks, J. Bakhshai, M.A. Makowsky, S. Muralidharan, P. Tsai, G.M. Rosen, J.P.Y. Kao, H-2,N-15-Substituted Nitroxides as Sensitive Probes for Electron Paramagnetic Resonance Imaging, Journal of Organic Chemistry, 75 (2010) 6463-6467.

[17] S. Koda, J. Goodwin, V.V. Khramtsov, H. Fujii, H. Hirata, Electron Paramagnetic Resonance-Based pH Mapping Using Spectral-Spatial Imaging of Sequentially Scanned Spectra, Analytical Chemistry, 84 (2012) 3833-3837.

[18] Y.J. Lin, B.A. Teicher, H.J. Halpern, Synthesis of 4-Protio-3-Carbamoyl-2,2,5,5-Tetraperdeuteromthyl-3-Pyrrolin-1yloxy (mHCTPO)- a Selectively Isotropically Labeled Compound for Use in T_2 Spin Label Oxymetry , Journal of Labelled Compounds & Radiopharmaceuticals, 28 (1990) 621-631.

[19] F. Hyodo, S. Matsumoto, N. Devasahayam, C. Dharmaraj, S. Subramanian, J.B. Mitchell, M.C. Krishna, Pulsed EPR Imaging of Nitroxides in Mice, Journal of Magnetic Resonance, 197 (2009) 181-185.

[20] J.R. Biller, V. Meyer, H. Elajaili, G.M. Rosen, J.P.Y. Kao, S.S. Eaton, G.R. Eaton, Relaxation Times and Line Widths of Isotopically-Substituted Nitroxides in Aqueous Solution at X-band, Journal of Magnetic Resonance, 212 (2011) 370-377.

[21] J.R. Biller, V.M. Meyer, H. Elajaili, G.M. Rosen, S.S. Eaton, G.R. Eaton, Frequency Dependence of Electron Spin Relaxation Times in Aqueous Solution for a Nitronyl Nitroxide Radical and Perdeuterated-Tempone between 250 MHz and 34 GHz, Journal of Magnetic Resonance, 225 (2012) 52-57.

[22] J.R. Biller, H. Elajaili, V. Meyer, G.M. Rosen, S.S. Eaton, G.R. Eaton, Electron Spin Lattice Relaxation Mechanisms of Rapidly-Tumbling Nitroxide Radicals, Journal of Magnetic Resonance, 236 (2013) 47 - 56.

[23] R.W. Quine, S.S. Eaton, G.R. Eaton, Saturation Recovery Electron Paramagnetic Resonance Spectrometer, Review of Scientific Instruments, 63 (1992) 4251-4262.

[24] R.W. Quine, G.R. Eaton, S.S. Eaton, Pulsed EPR spectrometer, Review of Scientific Instruments, 58 (1987) 1709-1723.

[25] B. Epel, C.R. Haney, D. Hleihel, C. Wardrip, E.D. Barth, H.J. Halpern, Electron Paramagnetic Resonance Oxygen Imaging of a Rabbit Tumor using Localized Spin Probe Delivery, Medical Physics, 37 (2010) 2553-2559.

[26] S.K. Rengan, M.P. Khakhar, B.S. Prabhananda, B. Venkataraman, Study of Molecular Motions in Liquids by Electron Spin-lattice Relaxation Measurements, I. Semiquinone ions in hydrogen bonding solvents, Pramana, 3 (1974) 95-121.

[27] P.W. Percival, J.S. Hyde, Saturation-Recovery Measurments of Spin-lattice Relaxation-Times of Some Nitroxides in Solution, Journal of Magnetic Resonance, 23 (1976) 249-257.

[28] H. Sato, S.E. Bottle, J.P. Blinco, A.S. Micallef, G.R. Eaton, S.S. Eaton, Electron Spin-lattice Relaxation of Nitroxyl Radicals in Temperature Ranges that Span Glassy Solutions to Low-viscosity Liquids, Journal of Magnetic Resonance, 191 (2008) 66-77.

[29] B.H. Robinson, D.A. Haas, C. Mailer, Molecular Dynamics in Liquids: Spin-lattice Relaxation of Nitroxide Spin Labels., Science, 263 (1994) 490-493.

[30] D.J. Schneider, J.H. Freed, Calculating Slow Motional Magnetic Resonance Spectra: a User's Guide, in: J.R. L.J. Berliner (Ed.) Biological Magnetic Resonance, 1989, pp. 1-76.

[31] J.H. Freed, ESR and Molecular Dynamics, in: Biological Magnetic Resonance, 2005, pp. 239-268.

[32] J.H. Freed, Theory of Slow Tumbling ESR Spectra of Nitroxides, in: L.J. Berliner (Ed.) Spin Labeling: Theory and Applications, Academic Press, New York, 1976, pp. 53–132.

[33] D.E. Budil, S. Lee, S. Saxena, J.H. Freed, Nonlinear-least-squares Analysis of Slow-Motion EPR Spectra in One and Two Dimensions using a Modified Levenberg-Marquardt Algorithm, Journal of Magnetic Resonance Series A, 120 (1996) 155-189.

[34] Z. Yu, R.W. Quine, G.A. Rinard, M. Tseitlin, H. Elajaili, V. Kathirvelu, A.Rajca, S.S. Eaton, and G.R. Eaton, Rapid-Scan EPR of Immobilized Nitroxides, Journal of Magnetic Resonance, (2014).

[35] H. Sato, V. Kathirvelu, A. Fielding, J.P. Blinco, A.S. Micallef, S.E. Bottle, S.S. Eaton, G.R. Eaton, Impact of Molecular Size on Electron Spin Relaxation Rates of Nitroxyl Radicals in Glassy Solvents between 100 and 300K, Molecular Physics, 105 (2007) 2137-2151.

[36] V. Meyer, L. Clouston, P.J. Boratyński, A. Rajca, R. Stein, H. Mchaourab, S.S. Eaton, and G.R., Eaton, unpublished results.

[37] Y. Song, G.R. Buettner, Thermodynamic and Kinetic Considerations for the Reaction of Semiquinone Radicals to Form Superoxide and Hydrogen Peroxide, Free Radicals in Biology and Medicine, 49 (2010) 919 - 962.

[38] S. Mishra, P. Malhotra, A.K. Gupta, P.K. Singh, S. Javed, R. Kumar, Semiquinone Glucoside Derivative (SQGD) Isolated from Bacillus sp. INM-1 Protects Against gamma Radiation - Induced Oxidative Stress, Environmetal Toxicology and Pharmacology, 37 (2014) 553 - 562.

[39] G. Armendariz-Vidales, L.S. Hermandez-Munoz, F.J. Gonzalez, A.A. de Souza, F.C. de Abreu, G.A.M. Jardim, E.N. da Silva, M.O. Gulart, C. Frontana, Nature of Electrogenerated Intermediates in Nitro-substituted nor B-lapachones: The Structure of Radical Species during Successive Electron Transfer in Multiredox Centers, Journal of Organic. Chemistry, 79 (2014) 5201 - 5208.

[40] P.S. Guin, S. Das, P.C. Mandal, Electrochemical Reduction of Quinones in Different Media: A Review, International Journal of Electrochemistry, 2011, dx.doi.org/10.4061/2011/816202

[41] J.A. Pederson, CRC Handbook of EPR Spectra from Natural and Synthetic Quinones and Quinols, CRC Press, Boca Raton, FL, 1985.

[42] R.W. Fessenden, J.P. Hornak, B. Venkataram, Electron Spin-lattice Relaxation Times of Transient Free Radicals, Journal of Chemical Physics, 74 (1981) 3694-3704.

[43] S.K. Rengan, M.P. Khakhar, B.S. Prabhananda, B. Venkataraman, Electron Spin-Lattice Relaxation in Organic Free Radicals in Solutions, Pure and Applied Chemistry, 32 (1972) 287-305.

[44] S.K. Rengan, M.P. Khakhar, B.S. Prabhananda, B. Venkataraman, Study of Molecular Motions in Liquids by Electron Spin-lattice Relaxation Measurements, II. 2,5-Di-tert-butylsemiquinone Ions in Acetonitrile and Tetrahydrofuran, J. Magn. Reson., 16 (1974) 35-43.

[45] B.S. Prabhananda, J.S. Hyde, Study of Molecular Motions in Liquids by Electron Spin Relaxation: Halogenated p-semiquinone Anions in Alcohols, Journal of Chemical Physics, 85 (1986) 6705-6712.

[46] G. Krishnamoorthy, B.S. Prabhananda, Molecular Motions in Liquidlike Pockets of Frozen Solutions: Electron Spin Relaxation Study of Semiquinones in DMSO and DMSO - Ethanol Mixtures, Journal of Chemical Physics, 76 (1982) 108-113.

[47] P.W. Atkins, D. Kivelson, ESR Linewidths in Solution. II. Analysis of Spin-Rotational Relaxation Data, Journal of Chemical Physics, 44 (1966) 169-174.

[48] L.T. Muus, P.W. Atkins, Electron Spin Relaxation in Liquids, Plenum Press, 1972.

[49] V. Kathirvelu, H. Sato, S.S. Eaton, G.R. Eaton, Electron Spin Relaxation Rates for Semiquinones between 25 and 295 K in Glass-Forming Solvents, Journal of Magnetic Resonance, 198 (2009) 111-120.

[50] J.G. Castle, Jr., D.W. Feldman, Temperature Dependence of Paramagnetic Relaxation at Point Defects in Vitreous Silica, Journal of Applied Physics, 36 (1965) 124-128.

[51] R. Owenius, G.R. Eaton, S.S. Eaton, Frequency (250 MHz to 9.2 GHz) and Viscosity Dependence of Electron Spin Relaxation of Triarylmethyl Radicals at Room Temperature, Journal of Magnetic Resonance, 172 (2005) 168-175.

[52] J.S. Hyde, J.-J. Yin, W.K. Subczynski, T.G. Camenisch, J.J. Ratke, W. Froncisz, Spin-labeled EPR T_1 Values Using Saturation Recovery from 2 to 35 GHz, Journal of Physical Chemistry B, 108 (2004) 9524-9529.

[53] B.H. Robinson, C. Mailer, A.W. Reese, Linewidth Analysis of Spin Labels in Liquids. I. Theory and Data Analysis, Journal of Magnetic Resonance, 138 (1999) 199-209.

[54] C. Mailer, R.D. Nielsen, B.H. Robinson, Explanation of Spin-Lattice Relaxation Rates of Spin Labels Obtained with Multifrequency Saturation Recovery EPR, Journal of Physical Chemistry A, 109 (2005) 4049-4061.

[55] V. Kathirvelu, H. Sato, R.W. Quine, G.A. Rinard, S.S. Eaton, G.R. Eaton, EPR Free Induction Decay Coherence Observed after a Single-Pulse in Saturation Recovery Experiments for Samples with Resolved Multi-line CW Spectra, Applied Magnetic Resonance, 32 (2007) 269-281.

[56] L. Valgimigli, R. Amorati, M.G. Fumo, G.A. DiLabio, G.F. Pedulli, K.U. Ingold, D.A. Pratt, The Unusual Reaction of Semiquinone Radicals with Molecular Oxygen, Journal of Organic Chemistry, 73 (2008) 1830 - 1841.

[57] R.W. Quine, G.A. Rinard, S.S. Eaton, G.R. Eaton, A Pulsed and Continuous Wave 250 MHz Electron Paramagnetic Resonance Spectrometer, Magnetic Resonance Engineering, 15 (2002) 59-91.

[58] R.W. Quine, G.A. Rinard, B.T. Ghim, S.S. Eaton, G.R. Eaton, A 1-2 GHz Pulsed and Continuous Wave Electron Paramagnetic Resonance Spectrometer, Review of Scientic Instruments, 67 (1996) 2514-2527.

[59] S.W. Provencher, An Eigenfunction Expansion Method for the Analysis of Exponential Decay Curves, Journal of Chemical Physics, 64 (1976) 2772-2777.

[60] A.J. Gordon, R.A. Ford, Properties of Solvents and Common Liquids, in: The Chemist's Companion: A Handbook of Practical Data, Techniques, and References, Wiley-Interscience Publication, New York 1972, pp. 4-5.

[61] R.E.D. McClung, D. Kivelson, ESR Linewidths in Solution. V. Studies of Spin–Rotational Effects Not Described by Rotational Diffusion Theory, Journal of Chemical Physics, 49 (1968) 3380 - 3391.

[62] D. Kivelson, P. Madden, Light Scattering Studies of Molecular Liquids, Annual Review of Physical Chemistry, 31 (1980) 523-558.

[63] M. Flores, R.A. Isaacson, R. Calvo, G. Feher, W. Lubitz, Probing Hydrogen Bonding to Quinone Anions Radicals by ^{1}H and ^{2}H ENDOR Spectroscopy at 35 GHz, Chemical Physics , 294 (2003) 401-413.

[64] M.L. Paddock, M. Flores, R. Isaacson, J.N. Shepherd, M.Y. Okamura, EPR and ENDOR Investigation of Rhodosemiquinone in Bacterial Reaction Centers Formed by B-Branch Electron Transfer Applied Magnetic Resonance, 37 (2010) 39 - 48.

[65] P. Ackermann, F. Barbarin, J.P. Germain, C. Fabre, Resonance Paramagnetique Electronique. Influence de la Solvation sur la Relaxation Electronique Anisotrope de Radicaus Stable Neutres ou Charges Proceedings of the Colloquium Spectroscopicum Internationale 2 (1975) 440 - 445.

[66] R. Owenius, G.E. Terry, M.J. Williams, S.S. Eaton, G.R. Eaton, Frequency Dependence of Electron Spin Relaxation of Nitroxyl Radicals in Fluid Solution, Journal of Physical Chemistry B, 108 (2004) 9475-9481.

[67] A.A. Bobko, I. Dhimitruka, J.L. Zweier, V.V. Khramtsov, Trityl Radicals as Persistent Dual Function pH and Oxygen Probes for in Vivo Electron Paramagnetic Resonance Spectroscopy and Imaging: Concept and Experiment, Journal of the American Chemical Society, 129 (2007) 7240-7241.

[68] H.J. Halpern, C. Yu, M. Peric, E. Barth, D.J. Grdina, B.A. Teicher, Oxymetry Deep in Tissues with Low-frequency Electron Paramagnetic Resonance, Proceedings of the National Academy of Sciencs U. S. A., 91 (1994) 13047-13051.

[69] T.J. Reddy, T. Iwama, H.J. Halpern, R.H. Viresh, General Synthesis of Persistent Trityl Radicals for EPR Imaging of Biological Systems, Journal of Organic Chemistry, 67 (2002) 4635-4639.

[70] I. Dhimitruka, M. Velayutham, A.A. Bobko, V.V. Khramtsov, F.A. Villamena, C.M. Hadad, J.L. Zweier, Large-scale Synthesis of a Persistent Trityl Radical for Use in Biomedical EPR Applications and Imaging, Bioorganic Medicinal Chemistry Letters, 17 (2007) 6801- 6805.

[71] H.J. Halpern, C. Yu, M. Peric, E.D. Barth, G.S. Karczmar, J.N. River, D.J. Grdina, B.A. Teicher, Measurement of Differences in pO_2 in Response to Perfluorocarbon/carbogen in FSa and NFSa Murine Fibrosarcomas with Low-frequency Electron Paramagnetic Resonance Oximetry, Radiation Research, 145 (1996) 610-618.

[72] M. Elas, B. Williams, A. Parasca, C. Mailer, C.A. Pelizzari, M.A. Lewis, J.N. River, G.S. Karczmar, E.D. Barth, H.J. Halpern, Quantitative Tumor Oxymetric Images from 4D Electron Paramagnetic Resonance Imaging (EPRI): Methodology and Comparison with Blood Oxygen Level-Dependent (BOLD) MRI, Magnetic Resonance in Medicine, 49 (2003) 682-691.

[73] M. Elas, K.H. Ahn, A. Parasca, E.D. Barth, D. Lee, C. Haney, H.J. Halpern, Electron Paramagnetic Resonance Oxygen Images Correlate Spatially and Quantitatively with OxyLite Oxygen Measurements, Clinical Cancer Research, 12 (2006) 4209-4217.

[74] I. Dhimitruka, A.A. Bobko, C.M. Hadad, J.L. Zweier, V.V. Khramtsov, Synthesis and Characterization of Amino Derivatives of Persistent Trityl Radicals as Dual Function pH and Oxygen Paramagnetic Probes, Journal of the American Chemical Society, 130 (2008) 10780-10787.

[75] L. Yong, J. Harbridge, R.W. Quine, G.A. Rinard, S.S. Eaton, G.R. Eaton, C. Mailer, E. Barth, H.J. Halpern, Electron Spin Relaxation of Triarylmethyl Radicals in Fluid Solution, Journal of Magnetic Resonance, 152 (2001) 156-161.

[76] C. Mailer, S.V. Sundramoorthy, C.A. Pelizzari, H.J. Halpern, Spin Echo Spectroscopic Electron Paramagnetic Resonance Imaging, Magnetic Resonance in Medicine, 55 (2006) 904-912.

[77] B. Epel, S.V. Sundramoorthy, P. Seifi, J. Bryant, G. Redler, H.J. Halpern, Exploring the Limits of Electron Spin Echo in Vivo Oxygen imaging, in: Rocky Mountain Conference on Analytical Chemistry, Snowmass, Colorado, 2010, pp. abstract 141.

[78] B. Epel, S.V. Sundramoorthy, E.D. Barth, C. Mailer, H.J. Halpern, Comparison of 250 MHz Electron Spin Echo and Continuous Wave Oxygen EPR Imaging Methods for in Vivo Applications, Medical Physics, 38 (2011) 2045-2052.

[79] B. Epel, M.K. Bowman, C. Mailer, H.J. Halpern, Absolute oxygen R1e Imaging in Vivo with Pulse Electron Paramagnetic Resonance, Magnetic Resonance in Medicine, 70 (2013) 70:10.1002/mrm.24926.

[80] M.C. Krishna, N. Devasahayam, J.A. Cook, S. Subramanian, P. Kuppusamy, J.B. Mitchell, Electron Paramagnetic Resonance for Small Animal Imaging Applications, ILAR journal / National Research Council, Institute of Laboratory Animal Resources, 42 (2001) 209-218.

[81] K. Nakagawa, B. Epel, Locations of Radical Species in Black Pepper Seeds Investigated by CW EPR and 9 GHz EPR Imaging, Spectrochimica acta. Part A, Molecular and biomolecular spectroscopy, 131 (2014) 342-346.

[82] E. Lund, E. Adolfsson, N. Kolbun, H. Gustafsson, EPR Imaging of Dose Distributions Aiming at Applications in Radiation Therapy, Radiation Protection Dosimetry, 159 (2014) 130-136.

[83] J.P. Joshi, J.R. Ballard, G.A. Rinard, R.W. Quine, S.S. Eaton, G.R. Eaton, Rapid-Scan EPR with Triangular Scans and Fourier Deconvolution to Recover the Slow-scan Spectrum, Journal of Magnetic Resonance, 175 (2005) 44-51.

[84] G.A. Rinard, R.W. Quine, J.R. Biller, G.R. Eaton, A Wire-Crossed-Loop Resonator for Rapid Scan EPR, Concepts in Magnetic Resonance Part B-Magnetic Resonance Engineering, 37B (2010) 86-91.

[85] R.W. Quine, D.G. Mitchell, M. Tseitlin, S.S. Eaton, G.R. Eaton, A Resonated Coil Driver for Rapid Scan EPR, Concepts in Magnetic Resonance Part B-Magnetic Resonance Engineering, 41B (2012) 95-110.

[86] G.A. Rinard, R.W. Quine, S.S. Eaton, G.R. Eaton, E.D. Barth, C.A. Pelizzari, H.J. Halpern, Magnet and Gradient Coil System for Low-Field EPR Imaging, Magnetic Resonance Engineering, 15 (2002) 51-58.

[87] R.W. Quine, G.A. Rinard, S.S. Eaton, G.R. Eaton, Quantitative Rapid Scan EPR Spectroscopy at 258 MHz, Journal of Magnetic Resonance, 205 (2010) 23-27.

[88] J.R. Biller, M. Tseitlin, R.W. Quine, G.A. Rinard, H.A. Weismiller, H. Elajaili, G.M. Rosen, J.P. Kao, S.S. Eaton, G.R. Eaton, Imaging of Nitroxides at 250 MHz using Rapid-Scan Electron Paramagnetic Resonance, Journal of Magnetic Resonance, 242 (2014) 162 – 168.

[89] M. Tseitlin, D.G. Mitchell, S.S. Eaton, G.R. Eaton, Corrections for Sinusoidal Background and Non-orthogonality of Signal Channels in Sinusoidal Rapid Magnetic Field Scans, Journal of Magnetic Resonance, 223 (2012) 80 - 84.

[90] G.R. Eaton, S.S. Eaton, EPR Imaging: Progress and Prospects, Bulletin of Magnetic Resonance, 10 (1988) 22-31.

[91] G.R. Eaton, S.S. Eaton, Introduction to EPR Imaging Using Magnetic-field Gradients, Concepts in Magnetic Resonance, 7 (1995) 49-67.

[92] M.M. Maltempo, Differentiation of Spectral and Spatial Components in EPR Imaging using 2-D Image Reconstruction Algorithms., Journal of Magnetic Resonance, 69 (1986) 156-161.

[93] M.M. Maltempo, S.S. Eaton, G.R. Eaton, Algorithms for Spectral-Spatial Imaging with a "Missing Angle", in: G.R. Eaton, K. Ohno, S.S. Eaton (Eds.) EPR Imaging and in vivo Spectroscopy, CRC Press, Boca Raton, FL, 1991, pp. 145-152.

[94] M. Tseitlin, J. R. Biller, H. Elajaili, V. Khramtsov, I. Dhimitruka, G. R. Eaton, and S. S. Eaton,, New Spectral-Spatial Imaging Algorithm for Full EPR Spectra of Multiline Nitroxides and pH Sensitive Trityl Radicals, Journal of Magnetic Resonance, 245 (2014) 150-155.

[95] R.D. Nielsen, S. Canaan, J.A. Gladden, M.H. Gelb, C. Mailer, B.H. Robinson, Comparing Continuous Wave Progressive Saturation EPR and Time Domain Saturation Recovery EPR over the Entire Motional Range of Nitroxide Spin Labels, Journal of Magnetic Resonance, 169 (2004) 129-163.

Appendix – List of Publications

Relaxation Times and Line Widths of Isotopically-Substituted Nitroxides in Aqueous Solution at X-band, J. R. Biller, V. Meyer, H. Elajaili, G. M. Rosen, J. P.Y. Kao, S. S. Eaton, and G. R. Eaton, *J. Magn. Reson*. **212**, 370-377 (2011).

Frequency dependence of electron spin relaxation times in aqueous solution for a nitronyl nitroxide radical and perdeuterated-tempone between 250 MHz and 34 GHz, J. R. Biller, V. Meyer, H. Elajaili, G. M. Rosen, S. S. Eaton, G. R. Eaton, *J. Magn. Reson*. **225**, 52-57 (2012).

Electron Spin Lattice Relaxation Mechanisms of Rapidly-Tumbling Nitroxide Radicals, J. R. Biller, H. Elajaili, V. Meyer, G. M. Rosen, S. S. Eaton, and G. R. Eaton, J. Magn. Reson., 236, 47 – 56 (2013).

Imaging of Nitroxides at 250 MHz using Rapid-Scan Electron Paramagnetic Resonance, J. R. Biller, M. Tseitlin, R. W. Quine, G. A. Rinard, H. A. Weismiller, H. Elajaili, G. M. Rosen, J. P. Y. Kao, S. S. Eaton, and G. R. Eaton, J. Magn. Reson. 242, 162 – 164 (2014).

New spectral-spatial imaging algorithm for full EPR spectra of multiline nitroxides and pH sensitive trityl radicals, M. Tseitlin, J. R. Biller, H. Elajaili, V. Khramtsov, I. Dhimitruka, G. R. Eaton, and S. S. Eaton, J. Magn. Reson. 245, 150-155 (2014).

Rapid-Scan EPR of Immobilized Nitroxides, Zhelin Yu, Richard W. Quine, George A. Rinard, Mark Tseitlin, Hanan Elajaili, Velavan Kathirvelu, Andrzej Rajca, S. S. Eaton, and G. R. Eaton, J. Magn. Reson. submitted (2014).

Electron Spin Relaxation Times and Rapid Scan EPR Imaging of pH-sensitive Amino Substituted Trityl Radicals, Hanan B. Elajaili, Joshua R. Biller, Mark Tseitlin, Ilirian Dhimitruka, Valery V. Khramtsov, S. S. Eaton, and G. R. Eaton, J. Magn. Reson and Chem. submitted (2014).

Frequency Dependence of Electron Spin-lattice Relaxation for Semiquinones in Alcohol Solutions, Hanan B. Elajaili, Joshua R. Biller, S. S. Eaton, and G. R. Eaton, J. Magn. Reson. submitted (2014).